CARNEGIE MELLON UNIVERSITY

DOCTORAL THESIS

Inferring the complex internal structure of dwarf galaxies

Author:
Zhaozhou AN

Advisor:
Prof. Matthew G. WALKER

A thesis submitted in fulfillment of the requirements
for the degree of Doctor of Philosophy

in the

Department of Physics

April 25, 2024

Abstract

This thesis focuses on modeling the complex internal structure of dwarf galaxies. Dwarf galaxy is the most frequent type of galaxy in the universe. It is dominated by the dark matter and thus naturally becomes the best targets for testing the dark matter theories. The work I did focuses on the observations of the dwarf galaxies and infers the underlying structures using the observational data from several sky surveys.

In the first project, I infer the 3D shape of the dwarf galaxies around the MW. I combine the Dark Energy Camera Legacy Survey (DECaLS) DR8 photometry with *Gaia* photometry to study the 3D structure of Bootes I, Draco, Ursa Minor, Sextans and Sculptor dwarf galaxies using blue horizontal branch (BHB) stars as distance indicators. I construct a new colour-absolute magnitude of BHB stars that I use to measure the distance gradients within the bodies of the dwarf galaxies. I detect a statistically significant non-zero gradient only in Sextans and Sculptor. Through modelling of the gradient and 2-D density of the systems using triaxial Plummer models, I find that the distance gradients in both dwarf galaxies are inconsistent with prolate shape but compatible with oblate or triaxial shapes. In order to explain the observed gradients, the oblate models of Sextans and Sculptor need to have a significant intrinsic ellipticity larger than 0.47 for Sextans and 0.46 for Sculptor. The flattened oblate shape may imply a significant anisotropy in the velocity distribution in order to be consistent with the lack of significant velocity gradients in these systems.

In the next project, I look at a specific system: the Sagittarius dwarf galaxy and M54. I present results from simultaneous modeling of 2D (projected along the line of sight) position, proper motion and line-of-sight velocity for *Gaia*- and APOGEE-observed stars near the centre of the Sagittarius (Sgr) dwarf spheroidal galaxy. I use a mixture model that allows for independent sub-populations contributed by the Sgr galaxy, its nuclear star cluster M54, and the Milky Way foreground. I find an offset of 0.295 ± 0.029 degrees between the inferred centroids of Sgr and M54, corresponding to a (projected) physical separation of 0.135 ± 0.013 kpc. The detected offset might plausibly be driven by unmodelled asymmetry in Sgr's stellar configuration; however, standard criteria for model selection favour our symmetric model over an alternative that allows for bilateral asymmetry. I infer an offset between the proper motion centres of Sgr and M54 of $[\Delta\mu_\alpha \cos\delta, \Delta\mu_\delta] = [4.9, -19.7] \pm [6.8, 6.2]$ μas yr^{-1}, with magnitude similar to the covariance expected due to spatially-correlated systematic error. I infer an offset of 4.1 ± 1.2 km s^{-1} in line-of-sight velocity. Using inferred values for the systemic positions and motions of Sgr and M54 as initial conditions, I calculate the recent orbital history of a simplified Sgr/M54 system, which I demonstrate to be sensitive to any line-of-sight distance offset between M54 and Sgr, and to the distribution of dark matter within Sgr. Considering the case that the centroids of M54 and Sgr currently are offset by $\lesssim 0.7$ kpc, I find that if Sgr's dark matter halo has the central 'cusp' that characterises cold dark matter halos, then M54 is currently approaching apocentre of an orbit (within Sgr) that is gradually decaying due to dynamical friction. If Sgr's dark matter halo has a 'core' of uniform central density, then M54 is currently near pericentre of an orbit that is, as expected from previous work, relatively unaffected by dynamical friction. Finally, if the centroids currently are offset by $\gtrsim 0.7$ kpc, (thus dominated by an offset in line-of-sight distance), then the calculated orbits would imply that M54 fell into Sgr within the past 200 Myr.

Acknowledgements

Embarking on this journey has been an incredible experience for me. Before the end of the journey, I want to express my gratitude to the people whose support has helped me go through this path.

First, I want to thank my advisor Matthew Walker for all the guidance, patience, and encouragement he gives me. Matt gives me many constructive advice in my research project and is very supportive of my choices and plans. I have learnt a lot from working with Matt. It is my honour to have him as my advisor.

I also want to thank Sergey Koposov and Rupert Croft for their advice and help in the early stage of my PhD. Without their help, I wouldn't be able to continue my PhD.

In addition to Matt and Rupert, I want to thank the other two committee members, Antonella Palmese and Carlos Badenes, for their invaluable help and support. I greatly appreciate all the advice and suggestions from them for my thesis.

I would also like to thank Andrew Pace and Siddharth Satpathy for all the discussions. In addition to them, I feel lucky to have the opportunity to be in the same group with Kuan-Wei Huang, Kuldeep Sharma, Evan Tucker, Alexander Moskowitz, Christopher Kervick, Jeffrey Patrick, Rachel Buttry, Mei-Yu Wang, Raphael Errani, Nora Shipp, and Sofia Splawska.

I would like to thank my friends and colleagues in the Physics department of Carnegie Mellon University, and also the friends I met outside of the department.

Finally, I would like to thank my parents for the love and support over so many years. I would not have what I have without them and I am forever grateful for their unconditional love.

Contents

List of Figures

List of Tables

Chapter 1

Introduction

As a still unsolved problem, the dark matter (DM) problem has a surprisingly long history to at least the 1930s.

Jan Oort studied the Doppler shifts for stars in the Milky Way and found that the measured velocity is much higher than the expected from the visible mass. One explanation was that there is invisible dark matter which contributes to the total mass to make stars bound to the galaxy (Oort, 1932). At almost the same time, Fritz Zwicky studied the Coma cluster and found that the velocity dispersion requires a much higher mass density than the mass density from the observed visible matter (Zwicky, 1933). Shortly after that, Sinclair Smith studied the radial velocity of the stars from the Virgo Cluster and found that the mass of the cluster required from the radial velocity is much larger than the observed visible mass (Smith, 1936). However, the assumption of the existence of the dark matter was not widely accepted at that time.

Besides the discrepancy between the measurement of the mass in the cluster of galaxies, the flat galactic rotation curves add more evidence to the existence of the dark matter. A bunch of studies (Freeman, 1970; Rubin and Ford, 1970; Rogstad and Shostak, 1972; Roberts and Whitehurst, 1975; Rubin, Ford, and Thonnard, 1980) of the rotation curves found that the curves are flatter than expected, which requires the explanation and dark matter can be one of the possibilities.

According to the story told by Jaco de Swart, Gianfranco Bertone and Jeroen van Dongen (Swart, Bertone, and Dongen, 2017), the community did not widely adopt the dark matter theory until they needed extra mass to make the universe's mass density close to the critical value so that the universe is closed, which is 1970s. Two papers bring the problems together (Einasto, Kaasik, and Saar, 1974; Ostriker, Peebles, and Yahil, 1974) and the dark matter theory did not come as a unified solution to the cluster mass problem and the flat rotation curves problem, instead, the two problems became the evidence of the extra mass called dark matter.

1.1 Dark Matter Candidates

Before trying to come up with new particles as the dark matter particle(s), it is natural to think that maybe dark matter is just compact objects with much less brightness, which are called massive astrophysical compact halo objects (MACHOs). However, the search for MACHOs using gravitational microlensing has shown that there are not enough MACHOs to explain dark matter (Lasserre et al., 2000; Tisserand et al., 2007). On the other hand, we can infer the cosmic baryon density from the abundances of primordial light element or the Cosmic Microwave Background (CMB), both methods eventually show that the baryonic matter in the universe is too small to be dark matter (Fukugita, Hogan, and Peebles, 1998; Burles, Nollett, and Turner, 2001; Hinshaw et al., 2013; Planck Collaboration et al., 2016). Both efforts indicate that the dark matter consists of the new particle, but the question of which particle(s) the dark matter is is still in debate today.

Lots of effort was put into narrowing down the candidates for the dark matter particle. Within the standard model, neutrinos become a tempting choice because they do not experience electromagnetic or strong interactions. However, the mass limit of the neutrinos in the standard model puts an upper bound on the total relic density of them, which is too low to account for the mass of the dark matter. Even if the mass limit is evaded from some assumptions, the neutrinos will be relativistic particle which results in a top-down formation history of the structure in the Universe, which is inconsistent with the observations (Bond and Szalay, 1983; Peebles, 1984). As the particle physicist searches for an extension or more fundamental theory for the standard model, more possible candidates became the natural results of these efforts. The supersymmetry theory is one of the most important theories in theoretical physics (Nilles, 1984; Jungman, Kamionkowski, and Griest, 1996), which also provides a bunch of the dark matter candidates including neutralinos, sneutrinos, gravitinos, and axinos. Axions, which are introduced in an attempt to solve the problem of CP violation, are also considered as the dark matter candidate. The Sterile neutrinos are the hypothetical particles without standard model weak interactions, which is also a viable dark matter candidate (Boyarsky et al., 2019).

With the help of the numerical simulations, it has shown that hot dark matter (relativistic) cannot reproduce the observed large scale structure of our universe (White, Frenk, and Davis, 1983), which indicate we should look for cold dark matter particle (non-relativistic). The regime of a particle freeze-out in the early Universe to be cold relic and still remain sufficient relic abundance to match the observed dark matter density puts strong constraints on the mass and self-annihilate cross section of the particle. All those constraints from the analytic analysis and simulations, combined with the theoretical preference of the new physics at or around the electroweak scale, lead to the weakly interacting massive particles (WIMPs) (Steigman and Turner, 1985), which have become the most popular candidate for the cold dark matter particle at present.

Besides the cold dark matter theory, there are several alternative theories which can potentially also be the solution to the dark matter problem.

The self-interacting dark matter (SIDM) (Carlson, Machacek, and Hall, 1992) is an alternative class of dark matter particles that can solve the cusp-core problem and missing satellites problems which we are going to consider in Section 1.2. SIDM particle is cold, non-dissipative, and self-interacting with a large scattering cross section (Spergel and Steinhardt, 2000). Compared with cold dark matter theory, SIDM predicts that the dark matter halo will have isothermal velocity dispersion, more spherical shape than cold dark matter halo, and have a cored central density distribution even in the galaxy with a smooth star formation history. The predictions may potentially distinguish SIDM theory from the cold dark matter theory in the observation (Tulin and Yu, 2018).

The warm dark matter (WDM) is another dark matter particle which is inspired by the small-scale problems in the cold dark matter theory. The higher velocity makes it have a large free-streaming length which can suppress the small-scale structure and thus alleviate the small-scale problems (Bode, Ostriker, and Turok, 2001). However, some studies using Lyman-α forest data and gravitational lenses put the constraints on the free-streaming length of WDM and this calls into question whether WDM still remains a viable solution to the small-scale problems (Gilman et al., 2020; Iršič et al., 2017).

Fuzzy dark matter (FDM) is another dark matter particle which, again, is inspired by the small-scale problems in the cold dark matter theory (Hu, Barkana, and Gruzinov, 2000). FDM particle is assumed to be extraordinarily light and thus the de Broglie wavelength of the particle will be $\sim 1\,\mathrm{kpc}$, so the kpc scale cusps in the dark matter halos are suppressed and fewer low mass halos are predicted in this theory. It can also explain the 'timing problem' in the Fornax dwarf galaxy where the globular clusters have not fallen into the centre of the Fornax dSph at present time, while the time for the falling due

to the dynamical friction from the analytical estimates is much shorter than their ages (Tremaine, 1976; Hernandez and Gilmore, 1998; Hui et al., 2017).

The modified Newtonian dynamics (MOND) is a quite different solution to the missing mass problem. It is first proposed by Mordehai Milgrom's trio papers (Milgrom, 1983c; Milgrom, 1983a; Milgrom, 1983b). The key idea of the MOND is that assuming the Newton's second law is correct at large acceleration but inaccurate at small acceleration. The modified formula at low acceleration should instead be $F = ma^2/a_0$, where a_0 is a constant. The new formula makes it possible to explain the observations without the need for the extra mass in the universe. The idea indicates an alternative solution of dark matter theory. The MOND theory has changed, and several versions have been proposed to accommodate the observations (Clowe et al., 2006; Angus, Famaey, and Zhao, 2006; Nojiri, Odintsov, and Oikonomou, 2017). One famous example is the bullet cluster 1E 0657-558, where the gravitational approximately potential traces the distribution of galaxies instead of tracing the plasma distribution which is the dominant baryonic mass component (Clowe et al., 2006), and MOND theories have difficulty explaining this observation. Later Angus, Famaey, and Zhao (2006) analyse the three versions of MOND and conclude that it is possible to reproduce the observation of the bullet cluster in the MOND scenario. MOND still remains as a viable solution to the dark matter problem.

The cold dark matter (CDM) theory is extremely successful at reproducing the large-scale structures of our universe, making it the most popular solution to the dark matter problem, and thus we will only focus on the discrepancy between CDM and the observations and ignore the other alternative theories in this work.

1.2 ΛCDM

Putting cold dark matter and dark energy together, we now have the prominent cosmological model ΛCDM, where the universe consists of around 70% dark energy, 25% cold dark matter and 5% baryons. ΛCDM makes predictions which match the observations very well on the large scale, but encountered several issues when it is used to predict small-scale structure.

1.2.1 Cusp or Core

With the results of the numerical simulation of the cold dark matter in small scale, several papers pointed out the cusp-core challenge to the theory in 1990s (Flores and Primack, 1994; Moore, 1994). The cold dark matter only simulation found that the density distribution of the dark matter halo can be well described by the NFW profile (Navarro, Frenk, and White, 1997) at a wide range of scales, where the central density ρ is proportional to r^{-1}. Some ΛCDM simulations suggest that the Einasto profile is a better empirical model that has the central region slope slightly shallower than -1 (Einasto, 1965; Merritt et al., 2006). However, these predictions from the cold dark matter simulations are way above many observed density curves in low-mass dark-matter-dominated galaxies (McGaugh, Rubin, and Blok, 2001; Simon et al., 2005; Blok et al., 2008; Naray, McGaugh, and Blok, 2008). This mismatch between the observed core density profile and predicted cusp density profile is called the cusp-core problem.

1.2.2 Missing Satellites

In 1999, when people compared the results from the numerical CDM simulations in small scale to the observations, they found that the number of the satellites does not match the simulations at all. Ben Moore found that the simulations predict that there should be

about 500 satellites with circular velocities larger than the Draco and Ursa Minor systems (Moore et al., 1999), and Anatoly Klypin stated that the simulations predict $\sim$ 300 satellites in the Local Group (Klypin et al., 1999). However, the number of the satellites from the observation is much less than the predictions. For example, the number of satellites within the Milky Way is $\sim$ 50, while the simulations predict thousands of subhaloes, and it seems unlike to have the predicted number of the satellites even after considering the faint galaxies (Hargis, Willman, and Peter, 2014). The mismatch between the number of the predicted subhaloes and the number of the observed satellites is called the missing satellites problem.

1.2.3 Too-big-to-fail

Michael Boylan-Kolchin showed that the ΛCDM predicts the Milky Way should host massive subhaloes which is incompatible with any known MW satellite having $L_V > 10^5 L_\odot$ if we assume the monotonic relation between galaxy luminosity and halo mass still holds at this mass level (Boylan-Kolchin, Bullock, and Kaplinghat, 2011). This indicates we need either an explanation of why the monotonic relation between galaxy luminosity and halo mass breaks at this mass range or why those massive subhaloes are not produced in the Milky Way. Besides these two possible explanations, there is a nonzero chance that MW is a statistical anomaly. However, similar studies have been performed with the M31 satellite and a similar discrepancy is found (Tollerud, Boylan-Kolchin, and Bullock, 2014), and it is almost impossible to have two statistical anomalies together.

1.2.4 Diversity of Dwarf Galaxy Rotation Curves

Oman et al. (2015) compare the circular velocity profiles of galaxies in ΛCDM cosmological hydrodynamical simulations with the observed rotation curves of galaxies. They find that the shapes of the circular velocity profiles from the simulations have little variation at fixed maximum circular velocity, whereas the observed dwarf galaxies show a large diversity of rotation curve shapes, even at fixed maximum rotation speed. Later Oman et al. (2016) show that this problem may be better interpreted as dark mass deficits, and the formation of the core cannot explain this because the mass deficit extends over the whole luminous radius of the affected galaxies, and several examples have rotation curves which do not suggest a core. However, Brook (2015) suggest that the scatter from the stellar mass and dark matter halo mass relation and the scatter from the size and stellar mass relation can lead to the observed diversity of dwarf rotation curves. There is a correlation between the rotation curve shape and baryonic surface density, but some argue that this relation is too weak in the dwarf galaxy regime and cannot be used to explain the diversity of dwarf rotation curves. Some possible paths which may provide the solutions include baryonic inflows and outflows during galaxy formation, dark matter self-interactions, variations in the baryonic mass structure coupled to rotation velocities through the mass discrepancy-acceleration relation (MDAR) which describes a tight correlation between the observed rotational velocity and the rotation velocity inferred from the distribution of baryons (McGaugh, Lelli, and Schombert, 2016), and noncircular motions in gaseous discs (Santos-Santos et al., 2020).

1.2.5 Planes of Satellites

It has been known for a long time that satellite galaxies of MW seem to lie in a polar great circle around MW (Kunkel and Demers, 1976; Lynden-Bell, 1976). Kroupa, Theis, and Boily (2005) pointed out that the distribution is inconsistent with the substructure

population predicted by the dark matter theory and thus the MW satellites cannot be related to dark-matter dominated satellites. More studies on the MW satellites and Andromeda satellites show that it is unlikely that the thin planar distribution of satellites is a random sample from the predictions of ΛCDM (Pawlowski, Pflamm-Altenburg, and Kroupa, 2012; Pawlowski and Kroupa, 2013; Ibata et al., 2013). The unusual thin planar distribution of the satellites is the planes of satellites problem.

1.2.6 Possible Solutions

To solve all these small-scale problems, it is possible that CDM needs major modification to accommodate the observations in small scale. However, the CDM provides excellent predictions on the large scale, making it less likely to be completely incorrect. Overall, the tensions in the small scale is the discrepancy between the simulations and the observations, so there are naturally two directions to try to solve it:

1. The simulations and the physics theory used in the simulations need to be improved to make correct predictions on the small scale.

2. The observations have bias or extra uncertainty that is not properly considered, and these may explain the discrepancy with the predictions from the simulations.

On the simulation side, the oldest dark matter simulations are the dark matter only simulation, where the dark matter halos share a similar density profile (NFW or Einasto profile) at a wide range of scales, and the density profile is cuspy (Einasto, 1965; Navarro, Frenk, and White, 1997; Merritt et al., 2006). When people find that the predicted shape of dark matter density distribution does not match the observed shape, the first thing to consider is bringing the baryonic feedback into the simulations. The dark matter particle has limited physical processes to consider in the simulation, which makes it simple and quite efficient to calculate, however, the baryons have too many possible physics processes to be considered. The possible baryonic processes which may alter the simulation results include but are not limited to gas cooling, interstellar medium, star formation, stellar feedback, supermassive black holes, feedback from active galactic nuclei, magnetic field, cosmic rays, radiation hydrodynamics, etc (Vogelsberger et al., 2020). The limited computation power requires the simplification of those processes to make it possible to calculate, which will usually decrease the accuracy of the simulation. There are many studies about which baryonic feedback should be considered to reproduce the observations in the small scale.

The supernova-driven winds, which can expel a large fraction of the baryonic component from a dwarf galaxy disc after a vigorous episode of star formation, were introduced into the CDM simulation as the first try of including the baryonic feedback, and it has been shown that supernova-driven winds can convert the cusp shape dark matter density profile to a core. However, the radius of the core is sensitive to the properties of the baryonic disc, and the possible values can only produce a quite small core (Navarro, Eke, and Frenk, 1996). Even though this does not produce predictions that match very well with the observations, this effect of baryonic feedback has been shown to be important in the transformation from cusp to core. The physical process is complicated and difficult to simplify, so some papers try to explore the effect of the mass loss without considering the physics process underlying it. Read and Gilmore (2005) introduce the baryonic mass loss event numerically and explore how it affects the baryons and dark matter. They show that with one impulsive mass-loss event, the remaining stellar component of a dwarf spheroidal galaxy in the ΛCDM simulation is well fitted over many

scalelengths by an exponential profile, and two impulsive mass-loss phases with significant gas re-accretion can transform a cuspy dark matter profile into a core one with near-constant density at the centre. Later Pontzen and Governato (2012) proposed an analytic model that explains how dark matter cusps are transformed into cores under repeated, rapid oscillations of the central gravitational potential, which can be the result of recurrent, concentrated bursts of star formation that induce rapid expansion of gas through supernova feedback heating, indicating that extreme, violent mass loss events are not necessary in the formation of cores.

As more physical processes are added to the simulations and the resolution is improved owing to the improvement of the computation power, several mechanisms are found to be possible to lead the cusp-core transformation.

The gravitational potential change may be the most widely studied mechanism. The change in the central potential will transfer the energy into dark matter particles and thus generate a dark matter core. There are several possible physical processes that can cause the gravitational potential change. The supernova-driven wind introduced in Navarro, Eke, and Frenk (1996) is one of the possibilities. Later research report that resolving inhomogeneous interstellar medium can result in the strong outflows from supernova explosions which remove low angular momentum gas, and lead to a more realistic dwarf galaxies results in the simulation (Governato et al., 2010).

The stellar feedback can also change the central gravitation potential. Multiple bursty stellar formation can transform the cusp to the core. Mashchenko, Couchman, and Wadsley (2006) and Mashchenko, Wadsley, and Couchman (2008) use hydrodynamic simulation to show that the feedback from supernova explosions and stellar winds can drive the bulk motion of gas, which results in significant gravitational potential fluctuations and thus flattens the central dark matter cusp.

In addition to the gas flow due to stellar feedback, the impulsive heating from minor mergers can also change the gravitational potential, which will lead to the formation of a core. The special part of this mechanism is that it does not rely on stellar feedback, which means that it can possibly form a core in the ultra-faint dwarf where star formation was quenched at high redshift. However, late major mergers can regenerate a cusp, which means the shape of the central density distribution correlates with the mass assembly histories and thus leads to significant stochasticity in the central dark matter density slopes of ultra-faint dwarfs (Orkney et al., 2021).

The dynamical friction from the dense infalling substructures is another possible mechanism. Dynamical friction on the clumps of the baryonic mass will transfer the orbital energy to the dark matter particles, and thus transform the cusp to the core (El-Zant, Shlosman, and Hoffman, 2001).

The baryonic feedback which enables the formation of the core can also alleviate the too-big-to-fail problem by reducing the dark matter mass in the inner region without requiring dwarf galaxies to reside in lower-mass halos, and the simulations about MW-like environment has shown that the enhanced tidal stripping on satellites due to the central galaxy can also explain the observations of the satellites. Both mechanisms contribute to the solution to the too-big-to-fail problem for satellites. For the isolated field galaxies, the solution is less clear because they do not have a host, and thus there is no interaction with the host galaxy (Sales, Wetzel, and Fattahi, 2022).

Although baryonic feedback offers the possibility of reconciling the predictions of ΛCDM simulations to the observations at small scale, several predictions remain to be controversial as summarised in Sales, Wetzel, and Fattahi (2022). The first is that some simulations show that the inner density slopes should be correlated with the star formation activity as a natural result of core formation through stellar feedback (Chan et al.,

2015), while some simulations do not predict a strong correlation between them (Benítez-Llambay et al., 2019). The observation does suggest this correlation (Read, Walker, and Steger, 2019). The second is that some simulations show that the size of dark matter core is linked to the half-mass radius of the stars, while others suggest that the size of the dark matter core depends on how concentrated the energy deposition of the feedback is. The third is the discrepancy of the minimum galaxy mass needed for core formation, which decides whether we should expect the core or cusp in the ultra-faint dwarf or the mass threshold for forming a core in ultra-faint dwarf.

However, not all simulations agree that baryonic feedback can lead to the formation of cores. Some recent cosmological, hydrodynamical simulations show that the bursty star formation history is not correlated with the inner slope of the dark matter density profile, and there is no core formation evidence. Bose et al. (2019) argue that bursty star formation and supernova feedback are not sufficient for core formation. One possible explanation is that the gas density threshold for converting gas into stars is too low and it prevents the gas from becoming gravitationally dominant, and thus no significant enough gravitational potential fluctuation is produced by the stellar feedback, which explains why no formation of the core is observed in these simulations. However, the threshold used in the simulation is necessary to achieve a good match to the broad population of galaxies. They conclude that this may indicate the importance of large concentrations of gas over some scale for core formation to be efficient.

In addition to baryonic feedback, the improvement in the resolutions has also helped to get more accurate results. The simulations with improved resolution, combined with including the baryonic effects, using initial conditions which match the Local Group environment, show that ΛCDM can reproduce the observed dwarf galaxy population and the central masses of the satellite galaxies in the Local Group without showing the missing satellites or too-big-to-fail problem. (Sawala et al., 2016; Wetzel et al., 2016; Garrison-Kimmel et al., 2019).

On the observation side, there are a few questions and uncertainty from the observations that may lead to the solution to some of the previously mentioned problems. Some argue that the observation of the core shape may be the consequence of the imperfect assumption and biased estimator, and thus there are fewer core-shaped dark matter density profiles in the dwarf galaxies than we originally thought it would be.

Several mass estimators may be biased or should include extra uncertainties because of some of the assumptions they made. The uncertainty of the mass estimators which rely on the spherical Jeans equation depends on many properties of the dwarf galaxies including the 3-D shape of the galaxy, radial bias in the stellar velocity dispersion anisotropy, level of rotational support, and the alignment between galaxies and their host dark matter haloes (Campbell et al., 2017). It has been shown that Jeans modelling may overestimate the dynamical mass in a galaxy during periods of post-starburst gas outflow and underestimate the mass during periods of net inflow because of the assumption of dynamical equilibrium (El-Badry et al., 2017), and the assumption of the spherical symmetry in Jeans modeling can lead to biased density profile shape results for some mass estimators, which will falsely statistically significantly detect a core in the profile, while the actual shape of the profile is cusp (Genina et al., 2018).

Oman et al. (2016) suggest that the systematic errors in the inclination measurement, which is substantially underestimated in the nearly face-on galaxies, may potentially explain the large diversity of dwarf galaxy rotation curves because it affects the extraction of the circular velocity profile from the gas velocity fields. They also suggest that this systematic error may also decrease the reliability of the mass estimator using Jeans modelling.

With efforts on both the simulation and observation sides, the discrepancy between the observations and the predictions from the ΛCDM is becoming less severe. However, some tensions still exist and wait for better solutions to reconcile the predictions with the observations. The dwarf galaxies, which is small, dark matter dominated and the centre of most small-scale problems, have become the perfect testbed for the dark matter theory and the predictions from the simulations.

1.3 This Work

It is obvious that whether the dark matter theory can reproduce the observations of the dwarf galaxies has become one of the most important tests in the dark matter studies. However, the observation of the dwarf galaxies is not easy because of their low luminosity and lack of the distance information for stars along the line of sight. Even for the dwarf galaxies near the MW, it is quite difficult to measure the distance to the individual star with good precision, which makes it quite challenging to model the 3-D shape of the dwarf galaxy. Some dwarf galaxies like Sagittarius dwarf galaxy also have a complex internal structure and it overlaps with the MW background stars in projected sky, which makes it particularly difficult to model different components inside it properly. This work aims to improve the constraints from the observations, which can be used as information in the analysis or the targets for comparison in the simulation by inferring the internal structure of dwarf galaxies using the observational data from several sky surveys.

First we will infer the triaxial shape of the dwarf galaxies around the MW. This will provide information on the shape and orientation for the analytic calculation and simulation of these targets to improve the accuracy. We then study the centre of the Sagittarius dwarf galaxy, which is a complicated environment with multiple components and is heavily contaminated by the MW stars in the observational data. We analyse the 5-D data and provide information on the offset between the centre of the Sagittarius dwarf galaxy and the centre of the M54 in spatial, proper motion, and radial velocity space, along with the orbit calculations from our results for the possible implications of the origin of the M54 and the formation history of the Sagittarius dwarf galaxy. Our results will provide more information in the studies of the formation of globular cluster inside the dwarf galaxies and may help to constrain the shape of the dark matter density distribution in the Sagittarius dwarf galaxy.

1.4 Dwarf Galaxy

Dwarf galaxy is the most common type of galaxy in the universe. They are small and dark matter dominated. Dwarf galaxy is also the crucial building block of much larger galaxies in hierarchical formation models (White and Frenk, 1991). Several early works in 1980s already pointed out that the high mass-to-light ratio of the dwarf galaxy makes it a perfect object to study the dark matter (Aaronson, 1983; Lin and Faber, 1983; Faber and Lin, 1983).

At the time when only a handful of dwarf galaxies have been observed, it seems the dwarf galaxies can be easily identified and well separated from the giant galaxies in the central surface brightness and absolute magnitude space (Kormendy, 1985). With the improvement of the telescope, more systems have been observed, and the new discoveries bring about so many questions, including that the gap between the elliptical galaxy and dwarf elliptical galaxy in the central surface brightness vs luminosity space does not exist anymore (Graham and Guzmán, 2003). With more faint systems being discovered, even the definition of the galaxy becomes obscured (Kormendy, 1985; Jerjen, Binggeli, and

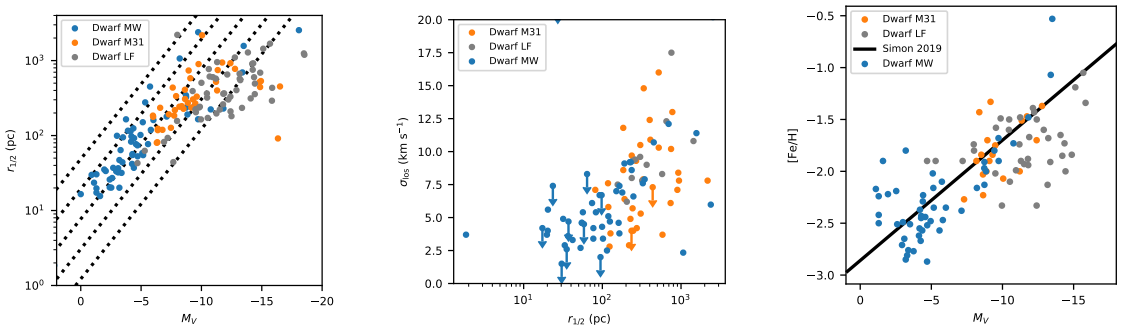

FIGURE 1.1: The figures of the size-luminosity relation (left), size-velocity dispersion relation (middle), and luminosity-metallicity relation (right) for the dwarf galaxies in the Local Field. Figures are modified versions of the Local Volume Database. The dwarfs in the MW (blue), dwarfs in the Andromeda (orange), and dwarfs in the Local Field outside of the MW and Andromeda (grey) are marked with different colours. The dotted lines in the left figure represent the constant surface brightness ($24, 26, 28, 30, 32$ mag/arcsec^2 from the top left to the bottom right). The down arrow symbols in the middle figure represent the upper limit of the velocity dispersion at 95% confidence interval, where the starting point of the arrow is the upper limit. The solid line in the right figure is the luminosity-metallicity relation from Simon (2019).

Freeman, 2000; Willman and Strader, 2012). We follow the definition from James S. Bullock (Bullock and Boylan-Kolchin, 2017) to divide the dwarf galaxies into three classes: bright dwarfs ($M \approx 10^{7-9}\, M_\odot$), classical dwarfs ($M \approx 10^{5-7}\, M_\odot$), and ultra-faint dwarfs ($M \approx 10^{2-5}\, M_\odot$).

Even though we call them dwarf galaxies, their properties can vary a lot among different dwarf galaxies. The mass-to-light ratio of the dwarf galaxies was originally thought to vary from $1 \sim 100$ (Mateo, 1998). With the improvement of the telescope and the found of the ultra-faint dwarf, the mass-to-light ratio can go above 1000 (Simon, 2019). The rotation curves of the dwarf galaxies show a large diversity as we talked in Section 1.2.4. Some are consistent with a cored dark matter density profile; some are consistent with the NFW profile, and some are even more concentrated than the NFW profile (Oman et al., 2015; Sales, Wetzel, and Fattahi, 2022). The shape of the host dark matter haloes of the dwarf galaxies is still in debate due to the difficulty of inferring the shape of the dark matter density distribution at the centre of the dwarf galaxies. Most may have a cored shape dark matter density profiles and some may have cuspy profiles (Read, Walker, and Steger, 2018). Most dwarf galaxies have elliptical shapes with the ellipticity less than 0.7 (based on the Local Volume Database maintained by Andrew Pace).

Several properties of the dwarf galaxy have strong correlations with each other, we show the plots of the size-luminosity relation, size-velocity dispersion relation, and luminosity-metallicity relation for the dwarf galaxies in the Local Field in Figure 1.1 using the compiled dwarf galaxy dataset from the Local Volume Database[1] and a slightly modified version of their sample code.

It is relatively difficult to observe dwarf galaxies due to their low luminosity; however, the relatively sufficient amount of the dwarf galaxies in the universe makes it possible to have several dwarf galaxies locate in very close distance to us. We can observe the stars for the dwarf galaxies in the Local Group, which enable the detailed studies of these

[1] https://github.com/apace7/local_volume_database

low-luminosity galaxies, like the studies about the internal kinematics of low-luminosity galaxies.

Dwarf galaxies are metal poor or at least have a metal poor stellar component, which means that they hold nearly primordial material, and the dwarf galaxy in the Local Group are the only galaxies for which we can obtain the reliable abundances from resolved stellar population (Mateo, 1998).

In addition to the properties of themselves, they can be used as probes for the nearby environment. The interaction between the Local Group dwarf galaxies and other larger galaxies may shed light on the assembly histories of those larger galaxies (Mateo, 1996; Wyse, 2001).

We have talked about the small-scale challenges in the ΛCDM theory in Section 1.2, and most of the unsolved problems are related with the dwarf galaxies, which make it the primary target for us to test the different dark matter theories.

The dwarf galaxies around the Milky Way can be used to constrain the density profile of the dark matter subhaloes (Stoehr et al., 2002), and the inner density profiles of haloes and subhaloes can be used to estimate the luminosity in dark matter annihilation radiation (Stoehr et al., 2003).

The ΛCDM simulations make predictions about the mass function of dark matter haloes and subhaloes. However, it is unknown whether the relation between the stellar mass and halo mass can be extrapolated to the low mass region. It has been shown that the observed stellar mass function cannot be reproduced by simply shifting the mass function of the dark matter haloes (Baldry et al., 2012; Bernardi et al., 2013; Wright et al., 2017; Bullock and Boylan-Kolchin, 2017), which raise the question about what the relation between these two masses at the small mass region, which is beyond our observation limits, is. More importantly, the predictions from different simulations show potential different predictions about the expected ultra faint populations, which may indicate that the large uncertainty exists in this regime in the simulation (Sales, Wetzel, and Fattahi, 2022).

Carlsten et al. (2020) shows that the radial spatial distribution of low-mass satellites around a MW-like host is generally more concentrated than the MW-sized haloes from the simulations, which indicate there possibly is some artificial disruption leading to this discrepancy.

With all the possibilities, dwarf galaxies are one of the most important probes and the testbed for the dark matter theories.

1.4.1 Sky Surveys

The studies in astronomy are always deeply bounded with the observations. Sky surveys are the main source of data from astronomy research. Every time a new sky survey is released, it will bring another wave of studies and new findings. Due to the generally low luminosity of the dwarf galaxies, they are always challenging the limits of sky surveys.

Gaia satellite was launched in December 2013 as the successor of the HIPPARCOS (European Space Agency, 1997; Gaia Collaboration et al., 2016a). It produced the first data release in Sep 2016, the second data release in Apr 2018, and the third data release (DR3) in Jun 2022. *Gaia* has a ambitious goal of measuring the 3-D spatial and 3-D velocity distribution of stars. *Gaia* DR3 includes more than 1.4 billion sources with full astrometry (Gaia Collaboration et al., 2023a). The photometry of *Gaia* DR3 includes three bands: G, G_{BP} and G_{RP}. BP band roughly covers the wavelength from 330 to 670 nm; RP band roughly covers the wavelength from 640 to 1050 nm; and G band roughly covers the wavelength from 330 to 1050 nm (Riello et al., 2021). *Gaia* DR3 provides the high-precision data where the photometric uncertainties are 1 mmag for G band, 12 mmag

for BP band, and 6 mmag for RP band for the sources with G = 17 mag, and the astrometric uncertainties are 0.05 mas for the position, 0.07 mas for the parallax, and 0.07 mas/yr for the proper motion for the sources with G = 17 mag. Even for faint sources with G = 20 mag, *Gaia* DR3 can achieve 6 mmag photometric uncertainty for the G band and 0.5 mas/yr median uncertainty for proper motion. Additionally, *Gaia* DR3 provides the radial velocity and some other data related with the spectra for part of the sources. The all-sky high-precision full astrometric data provided by *Gaia* enable tons of studies including many studies about dwarf galaxies.

Dark Energy Survey (DES) is a survey conducted by the Dark Energy Camera (DECam) which is mounted on the Blanco 4-m telescope at Cerro Telolo Inter-American Observatory (The Dark Energy Survey Collaboration, 2005). DES is designed to run for five years to collect data for measuring the dark energy and dark matter densities and the dark energy equation of state. DES covers $\sim 5000\,\mathrm{deg}^2$ of the southern sky and has five broadband filters g, r, i, z, and Y, roughly from 400 to 1060 nm (Drlica-Wagner et al., 2018). DES has already published two public data releases. DES is a deep survey with the 95% completeness limit at 24.6 mag (g), 24.3 mag (r), 24.0 mag (i), 23.7 mag (z), 23.4 (Y).

DECam is also used by the Dark Energy Camera Legacy Survey (DECaLS) (Dey et al., 2019). DECaLS is part of the DESI Legacy Imaging Surveys. DECaLS targets the entire South Galactic Cap and the $\delta \leq +34$ regions in the North Galactic Cap that are outside the coverage of DES. DECaLS provides photometry data for g, r, and z bands with exceptional depth. The data have the 5σ depth of $g = 24.0$ mag, $r = 23.4$ mag and $z = 22.5$ mag for an ELG galaxy with half-light radius of 0.45 arcsec. DECaLS also includes the data obtained as part of the Dark Energy Survey (DES), while it uses *The Tractor* software (Lang, Hogg, and Mykytyn, 2016) to extract the sources instead of using *PSFEx* (Bertin, 2011) and *SourceExtractor* (Bertin and Arnouts, 1996) as DES.

Apache Point Observatory Galactic Evolution Experiment (APOGEE) is part of the Sloan Digital Sky Survey, and it is composed of two generations: APOGEE-1 and APOGEE-2. APOGEE-1 is part of the SDSS-III and uses the Sloan 2.5 m Telescope. It is designed to build a spectra database for over 100*k* stars to benefit the large-scale, systematic, precision chemical and kinematical study (Majewski et al., 2017). APOGEE-2 is part of the SDSS-IV. As the continuation of APOGEE-1, it is ran by the 2.5-meter Sloan Foundation Telescope and the 2.5-meter Irénée du Pont telescope in parallel. Combined with APOGEE-1, they provide spectroscopic data which include stellar-atmospheric parameters and line-of-sight velocities measured from twin, multi-plexed, near-infrared, high-resolution spectra covering both the northern and southern sky (Abdurro'uf et al., 2022; Wilson et al., 2019).

1.4.2 Triaxial Shape of the Dwarf Galaxies

When we model the distribution of the stellar distribution and dark matter distribution, similar to many analysis processes in physics, we start with simple assumptions and gradually add the important complexities into the model and analysis to improve the quality of the results, and thus we usually start with a spherically symmetric shape. However, the improvement from the spherical shape to the triaxial shape is not an easy one. It will introduce four free parameters (ellipticity, triaxiality, and two parameters for the orientation of the major axis), and this will lead to many problems including the slower speed of computation, greatly increased complexity of the analytical calculation, increased size of the parameter space, etc. As a result, many studies in the field of ΛCDM and dwarf galaxies use the spherical symmetry assumption.

Gilmore et al. (2007) and Strigari, Frenk, and White (2010) use Jeans modelling mass estimator which assumes spherical symmetry. Walker et al. (2009a) and Wolf et al. (2010)

propose the mass estimators for the mass enclosed within half light radius of the dwarf galaxies from the analysis of the Jeans equation, where the mass profile is assumed to be spherically symmetric. Cole et al. (2012) adopt a spherical double-power-law profiles for the mass profile and stellar profile in their N-body simulations to study the globular cluster orbit in the Fornax. Pontzen and Governato (2012) propose an analytical description for the physical process related to the formation of the cored dark matter density profiles. One of the two restrictions of their analytical model is the assumption of the spherically symmetric potential. Errani, Peñarrubia, and Walker (2018) construct a virial mass estimator using the spherical virial theorem. Callingham et al. (2019) adopt the spherically symmetric NFW profile to model the host dark matter density profile in their mass estimator using distribution function modelling.

However, both the simulations and the observations have shown that the shape of dwarf galaxies and their host dark matter haloes are more likely to be triaxial.

On the simulation side, many N-body simulations work based on ΛCDM show that dark matter subhaloes that are likely to host dwarf galaxies usually have a triaxial shape (Kuhlen, Diemand, and Madau, 2007; Knebe et al., 2010; Vera-Ciro et al., 2014; Barber et al., 2015). The shape of the subhaloes will also be affected by the tidal stripping and the subhaloes will likely be more spherical after the tidal stripping (Kuhlen, Diemand, and Madau, 2007; Barber et al., 2015). The shape of the dark matter halo is correlated with the dark matter halo mass and the shape of the stellar distribution is correlated with the inner dark matter halo shape (Vera-Ciro et al., 2014; Zavala et al., 2016; Thob et al., 2019). In more massive dwarf galaxies the feedback from star formation can reshape and likely align the dark matter and baryon shapes (Governato et al., 2012). Some papers also point out that the orientation of inner regions of the dark matter haloes is well aligned with the galaxy shape but the outer regions can be substantially misaligned (Bailin and Steinmetz, 2005; Deason et al., 2011; Velliscig et al., 2015).

On the observation side, it is well known that many observed dwarfs have a non-spherical shape. The discrepancy between the reality of the triaxial shape and the assumption of the spherical shape in the studies is concerning. Several works show that the assumption of spherical symmetry may lead to misleading results if the actual distribution is triaxial. After their work in the analytical model using the spherically symmetric potential assumption, Pontzen et al. (2015) investigate how the spherical symmetry affect the analysis in the later work and conclude that it may lead to misleading results in both observation and simulation analysis. Read et al. (2016) argue that the galaxies with low inclinations may have systematically biased high inclination inference from the fitting, which will lead to the rotation curve with an artificial shallow rise, and this may falsely imply a large dark matter core. Campbell et al. (2017) apply the mass estimators from Walker et al. (2009a) and Wolf et al. (2010), which rely on the spherical Jeans equation, on the galaxies from APOSTLE cosmological hydrodynamical simulations, and find that the uncertainty of the estimator is strongly correlated with the 3-D shape of the galaxy. Genina et al. (2018) study the results from the cosmological hydrodynamic simulation and find that the incorrect assumption of the spherical symmetry can lead to biased density profile shape results for some mass estimators, which will under some conditions falsely statistically significantly detect a core in the profile, while the actual shape of the profile is cusp.

In addition to the potential extra uncertainty due to the triaxial shape, the use of the triaxial shape in the simulations and analysis may also lead to some new findings. Peñarrubia, Walker, and Gilmore (2009) show that the triaxiality of the galaxy potential can lead to some long-lasting substructures in the tidal disruption of globular cluster in dwarf spheroidal galaxies.

Given the importance of the triaxial shape in the analysis, it is useful to measure the triaxial shape of the observed dwarf galaxies. Some previous observational studies have measured the distribution of the shape and orientation of galaxies (Sandage, Freeman, and Stokes, 1970; Merritt and Tremblay, 1996; Kimm and Yi, 2007; Padilla and Strauss, 2008; Salomon et al., 2015; Sanders and Evans, 2017). These studies need a relatively large sample of the galaxies to have a well constrained result, and their conclusion may be correlated with which galaxy cluster they used. Given the limited number of the dwarf galaxies, it is useful to try to constrain the intrinsic shapes of individual dwarf galaxies.

However, measuring the shape of a single dwarf galaxy is generally difficult due to the lack of accurate distance measurement of the stars. In the Chapter 2 we will use the blue horizontal branch (BHB) stars as distance tracers, infer distance gradients of dwarf galaxies first, and then infer the 3-D shape based on the distance gradients and 2-D stellar density distribution.

1.4.3 Complex evolution history of dwarfs

Many dwarf galaxies are known to have multiple stellar components in metallicity and ages, which indicates the complex evolution history of dwarfs. For the dwarf galaxies inside the MW, which are also the dwarf galaxies that we can get the most detailed observation data due to the proximity, the interactions between them and other objects inside MW, as well as the tidal forces exerted by the Milky Way central region, add more complexity to the evolution history of the dwarf galaxies. Some dwarf galaxies also host the globular clusters (Huang and Koposov, 2021), which introduce more uncertainties in the evolution history, particularly regarding the origins of these globular clusters.

We can divide dwarf galaxies into several subclasses using morphology and colour. There are three common subclasses of dwarf galaxies from this perspective: dwarf spheroidal (dSph) or dwarf ellipticals (dE) galaxies which have elliptical shape, dwarf irregulars (dIrr) galaxies which have irregular shape, and blue compact dwarf (BCD) galaxies which host many young, hot stars and thus appear in blue in colour. In the context of the evolution history, a strong correlation was found between the features from the morphology and colour and the star formation histories of the dwarf galaxies. dSph and dE galaxies are usually gas-poor dwarfs without star formation events at the current time. dIrr galaxies usually are gas-rich dwarfs with low-rate star formation events, and BCD galaxies have intense bursts of star formation, which is the origin of those young stars. The correlation is strong but not necessarily true for all dwarf galaxies (Gallart et al., 2015), and the boundaries between different subclasses are not very clear either. There are transition type dwarf galaxies found in the observation which lie between the two subclasses (Mateo, 1998; Dellenbusch et al., 2008).

The dSph galaxies usually have very few gases in the central region (Knapp, Kerr, and Bowers, 1978). One of the possible explanations is the supernova feedback, which also plays an important role in the formation of a cored dark matter density profile as we have talked in Section 1.2.6. The outflow of the gas driven by the supernova explosions is considered a possible explanation for this deficit. In addition to this, ram pressure stripping and the effect of the dark matter are also possible explanations (Lin and Faber, 1983; Ferrara and Tolstoy, 2000).

The origin of the dSph galaxies is still in debate. There are several factors that may be important in the origins of the dSph: tidal interaction with the host (Mayer et al., 2001a; Mayer et al., 2002), the birth of small dark matter halos in CDM theories (Dekel and Silk, 1986), and the tidal debris of the collision between larger galaxies (Gerola, Carnevali, and Salpeter, 1983).

The origin of dwarf galaxies and the star formation histories are quite important in the test for the predictions of dark matter theories. The origin of dwarf galaxies may explain the shape and abundances of them. The star formation history is correlated with the shape of the dark matter density profile if the stellar feedback from the star formation is one of the dominant mechanisms in the formation of a cored dark matter density profile. Understanding the evolution history of the dwarf galaxies can help to understand dark matter.

1.4.4 Globular Cluster as the probe

Only a few dwarf galaxies host the globular clusters in the MW. The existence of these star clusters can be used to understand several key properties of these dwarf galaxies. There are five satellites that are known to host the globular clusters in the MW: Small Magellanic Clouds, Large Magellanic Clouds, Sagittarius dwarf spheroidal galaxy, Fornax dwarf spheroidal galaxy, and Eridanus 2 (Mackey and Gilmore, 2003b; Mackey and Gilmore, 2003a; Mackey and Gilmore, 2003c; Koposov et al., 2015; Crnojević et al., 2016). The systematic search for the globular clusters around the MW satellite dwarf galaxies did not find more host galaxies for the globular clusters (Huang and Koposov, 2021). Even though the globular cluster is a relatively simple system with barely any dark matter inside it, the problem of the origins of the globular clusters in the dwarf, whether they are accreted or formed in situ, is still in debate and is related to many other problems, such as the dark matter distribution of the host galaxy. The globular clusters in the dwarf galaxies become a great target for studying the formation of the globular clusters and testing dark matter theory.

Fornax dSph galaxy is the host for six globular clusters (Pace et al., 2021) and is in a less complex environment than the Sagittarius dSph galaxy, so it is the most common target for the study of the formation of the globular cluster and the relation between the location of them and the dark matter density profile of the Fornax dSph.

Various dynamical and N-body studies demonstrate that the efficiency and outcome of dynamical friction depend on the spatial distribution of dark matter within the host galaxy (Read et al., 2006; Goerdt et al., 2010). If the host dark matter halo has the central 'cusp' that characterises cold dark matter halos (Navarro, Frenk, and White, 1997, 'NFW' hereafter), dynamical friction operates efficiently to drag a massive GC to the centre in a fraction of a Hubble time; if instead the host halo has a central 'core' of uniform density, the infalling cluster tends to stall near the core radius, where the halo becomes effectively 'bouyant' (Cole et al., 2012; Banik and van den Bosch, 2022).

Several N-body simulation studies that are tailored for the Fornax dSph and its globular clusters have been performed. These studies try to find the solution and implications to the 'timing problem' of the Fornax dSph, where the globular clusters have not fallen into the centre of the Fornax dSph at present, while the time for falling due to the dynamical friction from the analytical estimates is much shorter than their ages (Tremaine, 1976; Hernandez and Gilmore, 1998). Some studies conclude that the Fornax dSph must have a cored dark matter density distribution so that the globular clusters did not fall into the centre of it (Goerdt et al., 2006), while a recent study argues that the current observations of the location of the globular clusters are insufficient to conclude the shape of the dark matter halo of the Fornax dSph, because the timescales for sinking and stalling would be almost the same for either the cuspy or cored dark matter halo (Meadows et al., 2020).

1.4.5 Sagittarius and M54

The Sagittarius dwarf spheroidal Galaxy (Sgr dSph), which is extremely large in the field of view, was actually discovered long after the discovery of the M54, which is the globular cluster at the centre of Sgr dSph. It is obscured by the foreground MW stars and hidden from sight until a radial velocity survey of the Galactic bulge revealed it (Ibata, Gilmore, and Irwin, 1994). Sgr dSph is one of the closest galaxies with a distance of $\sim$ 26 kpc from the Sun, $\sim$ 18 kpc from the Galactic centre. Its proximity makes it possible to study the Sagittarius in detail.

Sgr dSph is interesting because it is in the process of the tidal disruption due to the centre of MW, and left the prominent Sagittarius stream (Ibata et al., 2001; Majewski et al., 2003). The stream covers over a full 360° and has a prominent bifurcation (Belokurov et al., 2006). The Sagittarius stream has been used to constrain the orbit and stellar properties of the Sgr dSph and the mass distribution of the MW (Majewski et al., 2003; Vera-Ciro and Helmi, 2013).

Sgr is known to have a complex structure and host multiple components inside it. Among all the substructures, the centre of it is particularly interesting, where the core of Sgr and M54 reside. The central region of Sgr is composed of multiple components, which are different in size, photometry and kinematics. It is known that the centre of the Sgr includes at least old ($\gtrsim$ 10 Gyr), intermediate-age ($\sim 4-6$ Gyr) and young ($\lesssim$ 3 Gyr) stellar populations with a corresponding range of metallicity from -1.8$\lesssim$ [Fe/H]$\lesssim +0.6$, and the young and old stellar population has a more centrally concentrated spatial distribution than the intermediate-age stellar population (e.g. Sarajedini and Layden, 1995; Siegel et al., 2007; Siegel et al., 2011; Alfaro-Cuello et al., 2019). The old, metal-poor stars have a line-of-sight velocity dispersion profile that declines steeply within radius $\sim 3''$ (Ibata et al., 2009), then gradually rises until near M54's nominal tidal radius (Bellazzini et al., 2008), while the relatively metal-rich stars display approximately constant velocity dispersion $\simeq$ 9.6 km/s over the same region, and the constant velocity dispersion extends to radius $\sim 100'$ (Bellazzini et al., 2008). Interestingly, the metal-rich population also shows a metallicity gradient over the same region where the peak iron abundance goes from [Fe/H] $= -0.38$ for the radius $R \leq 2.5'$ to [Fe/H] $= -0.57$ for radius $5.0 < R \leq 9.0'$ (Mucciarelli et al., 2017).

The complexity is not limited to the nucleus, the main body of Sgr itself exhibits complex internal stellar kinematics, with a central bar-like structure that connects to 'tails' of escaping stars, a bound, rotating inner core, and apparent expansion along the long axis that characterises an overall triaxial morphology (del Pino et al., 2021).

The complex structure inside the Sgr indicates the complex formation history. Not only is the origin of M54 in debate, but it is also uncertain which populations belong to M54 and which belong to the Sgr. Different researchers often make their own assumptions about the definition of the M54. Majewski et al. (2003) use photometrically-selected M giant stars from the Two Micron All Sky Survey to argue that the overdense 'cusp' at the centre belongs to Sgr and not to M54 whose metal-poor stars are too blue to be included in the M giant sample. Monaco et al. (2005) select metal-poor and meta-rich populations from optical photometry and conclude that Sgr, which is assumed to host a metal-rich nuclear star cluster and exhibits an overdense cusp, appears as a nucleated galaxy independently of the presence of M54 at its centre. However, Alfaro-Cuello et al. (2019) suggest that the metal-rich stars are actually two populations: young ($\sim$ 2 Gyr) and intermediate-age ($\sim$ 4 Gyr) populations, with different spatial distributions. This level of complexity makes it quite difficult to disentangle M54 from its Sgr host and analyse them separately.

To make things more complex, the origin of the M54 is still uncertain. As discussed in Section 1.4.4, the status of the globular cluster which falls into the dwarf galaxy can be an indicator of the shape of the dark matter density profile. If the M54 is an example of a GC that fell to the centre of its host galaxy, then its properties may also help to constrain the shape of the dark matter density profile within Sgr.

Bellazzini et al. (2008) perform N-body simulations which are tailored for the M54 falling into the Sgr dSph with NFW dark matter halo and they find that the M54 can fall into the centre of the Sgr within relative short time (in $\lesssim 3$ Gyr) due to the dynamical friction. Herlan, Mastrobuono-Battisti, and Neumayer (2023) perform the similar studies with a focus on the effect of the shape of dark matter density profile, and they find that the dark matter density profiles with density $\rho \propto r^{-\gamma}, \gamma > 1$ can reproduce the results consistent with the observations, and a more cuspy profile will produce a highly rotating and more flattened nuclear star cluster which is not be able to reconcile with the observations.

In Chapter 3, we take an approach that is complementary to that of del Pino et al. (2021). Rather than adopting hard cuts in colour/magnitude or sky position to separate M54 and Sgr samples, we build a mixture model to analyse the 5D distribution of sky position, proper motion and line-of-sight velocity, the phase-space coordinates for which homogeneous measurements from Gaia EDR3 (Gaia Collaboration et al., 2021) and/or the Apache Point Observatory Galactic Evolution Experiment (APOGEE; Majewski et al., 2017) are available for large numbers of stars in the Sgr. The mixture modelling lets us obtain simultaneous estimates for the 5D centres of the Sgr and M54 populations, providing a direct inference about any offset in these dimensions of phase space. Any detected offset can then be used to inform subsequent models for the formation and evolution of M54 as the NSC within Sgr. Furthermore, since our mixture model does not operate separately on pre-selected M54 and Sgr samples, the result can be used to infer, rather than assume, the colour/magnitude distributions traced separately by the two objects.

Chapter 2

Constraining the shape of Milky Way satellites with distance gradients

The contents of this Chapter have been published as An and Koposov (2022) in which we analyze 3-D shape of the dwarf galaxies around the MW.

We combine the Dark Energy Camera Legacy Survey (DECaLS) DR8 photometry with *Gaia* photometry to study the 3-D structure of Bootes I, Draco, Ursa Minor, Sextans and Sculptor dwarf galaxies using blue horizontal branch (BHB) stars as distance indicators. We construct a new colour-absolute magnitude of BHB stars that we use to measure the distance gradients within the body of the dwarf galaxies. We detect a statistically significant non-zero gradient only in Sextans and Sculptor. Through modeling of the gradient and 2-D density of the systems by triaxial Plummer models we find that the distance gradients in both dwarf galaxies are inconsistent with prolate shape, but compatible with oblate or triaxial shapes. In order to explain the observed gradients, oblate models of Sextans and Sculptor need to have a significant intrinsic ellipticity larger than 0.47 for Sextans and 0.46 for Sculptor. The flattened oblate shape may imply a significant anisotropy in velocity distribution in order to be consistent with the lack of significant velocity gradients in these systems.

2.1 Introduction

The current cosmological paradigm (ΛCDM) based on cold dark matter and dark energy has been extremely successful in reproducing a vast variety of observations (Davis et al., 1985; Efstathiou, Bond, and White, 1992; Guo et al., 2011; Springel et al., 2005; Klypin, Trujillo-Gomez, and Primack, 2011) particularly at large scales. However ΛCDM predictions on small scales are still not fully supported by data. The list of problems on small scales is well known, including missing satellites problem (Klypin et al., 1999; Moore et al., 1999), core-cusp (Flores and Primack, 1994; Moore, 1994) and too-big-to-fail (Boylan-Kolchin, Bullock, and Kaplinghat, 2011). While probing the small scale behaviour of dark matter is possible with a variety of tracers, one of the best targets to resolve some of these problems and probe the nature of dark matter are the dwarf spheroidal galaxies, satellites of the Milky Way (Buckley and Peter, 2018; Bullock and Boylan-Kolchin, 2017; Simon, 2019). While being the most frequent type of galaxy in the universe, they are very dark mater dominated, making them perfect objects to study dark matter without being much influenced by baryons (Karachentseva, Karachentsev, and Börngen, 1985; Mateo, 1998; Tolstoy, Hill, and Tosi, 2009).

While twenty years ago the sample of known dwarf spheroidal galaxies contained a handful of galaxies, it has been increasing rapidly over the last years thanks to the arrival of large imaging surveys that enable the discoveries of so-called ultra-faint dwarfs (Irwin

et al., 2007; Belokurov et al., 2008; Homma et al., 2016; Torrealba et al., 2016; Koposov et al., 2015).

The dwarf spheroidal galaxies have been studied extensively both spectroscopically and photometrically over the years however their exact formation mechanism are still unclear. Specifically we have a poor understanding of how the dwarf galaxies observed now around the Milky Way looked before they were accreted onto the Milky Way and what morphological transformations the dwarf galaxies undergo in the accretion process (Mayer et al., 2001b; Mayer et al., 2007; Tomozeiu, Mayer, and Quinn, 2016). Due to resolution limits of current numerical simulations we also have a limited knowledge of what sets the detailed properties of of the dwarf galaxies such as luminosity and sizes (Guo et al., 2011; Boylan-Kolchin, Bullock, and Kaplinghat, 2012; Fitts et al., 2017).

One of the most crucial questions in studies of dwarf galaxies is the dark matter distribution inside them as this has implications not only on the origin of dwarf galaxies but also on the nature of dark matter itself (Hu, Barkana, and Gruzinov, 2000; Bode, Ostriker, and Turok, 2001). The dark matter densities been recently constrained through a variety of techniques, such as virial mass estimators (Errani, Peñarrubia, and Walker, 2018), Jeans modeling (Gilmore et al., 2007; Strigari, Frenk, and White, 2010), distribution function modeling (Li et al., 2017; Callingham et al., 2019), globular cluster kinematics (Peñarrubia, Walker, and Gilmore, 2009; Cole et al., 2012) and half-light radius mass estimators (Walker et al., 2009a; Wolf et al., 2010). While these techniques have been successful in extracting dark matter masses and densities, they are often relying on multiple assumptions, such as spherical symmetry or rotational symmetry.

With the improvement of the numerical simulation resolution, work by Kuhlen, Diemand, and Madau (2007), Knebe et al. (2010), Vera-Ciro et al. (2014), and Barber et al. (2015) used N-body simulations based on ΛCDM to show that dark matter subhaloes which are likely to host dwarf galaxies usually have a triaxial shape. Kuhlen, Diemand, and Madau (2007) and Barber et al. (2015) also show that tidal stripping will reduce the triaxiality of subhaloes and predict that luminous dSphs with relatively low dark matter content are more spherical than faint dark matter-dominated dwarfs. Furthermore in more massive dwarf galaxies the feedback from star formation can reshape and likely align the dark matter and baryon shapes (Governato et al., 2012). Zavala et al. (2016), Thob et al. (2019) show the shape of stellar distribution of galaxies is correlated with inner dark matter halo shape, and some papers show that the orientation of inner regions of the dark matter haloes is well aligned with the galaxy shape but the outer regions can be substantially misaligned (Bailin and Steinmetz, 2005; Deason et al., 2011; Velliscig et al., 2015). Several studies also show that for self-interacting dark matter, the dark matter shape may follow baryonic shape (Kaplinghat et al., 2014; Sameie et al., 2018), so studying the 3D shape of a galaxy can potentially help us test different dark matter models.

Several previous observational studies looked at distribution of projected axis ratios of galaxies to constrain the distribution of intrinsic 3-D shapes (Sandage, Freeman, and Stokes, 1970). Merritt and Tremblay (1996), Kimm and Yi (2007), and Padilla and Strauss (2008) applied this method to the elliptical galaxies and show that the bright elliptical galaxies have triaxial ellipsoid shape but the faint ones are consistent with oblate shape. A more recent study by Salomon et al. (2015) infers the intrinsic ellipticity distribution of dwarf galaxies in Andromeda system by assuming galaxies have prolate shapes and Sanders and Evans (2017) infers the distribution of 3-D shapes and alignments for dwarf spheroidal galaxies in the Local Group by using 2-D ellipticities, position angles of major axes and distance moduli. These studies using the distribution of apparent ellipticities usually require an assumption about random distribution of galaxy orientations and a large number of sample galaxies to get good constraints on the distribution of intrinsic

shapes. However as the number of observed dwarf galaxies is limited, it is useful to try to constrain the intrinsic shapes of individual dwarf galaxies.

The difficulty of constraining the intrinsic shape for single dwarf galaxy is that we only observe stars in projection, and it's hard to infer an accurate line of sight distance for each star, thus a 3-D spatial distribution for stars will have large uncertainty. In this paper we decide to first infer distance gradients of dwarf galaxies using blue horizontal branch (BHB) stars as tracers, then construct 3-D models based on the distance gradients and 2-D density distribution.

We describe the survey data we used and the how we calculate distance moduli for BHBs in Section 2.2, we then describe how we model the distance gradient of BHB stars with a mixture model in Section 2.3. In Section 2.4 we construct a 3-D shape model to distance gradient and 2-D density distribution and present the constraints on the intrinsic shapes of dwarf galaxies. We discuss our results and potential issues in our method as well as present several checks of our results in Section 2.5. The paper is concluded with Section 2.6.

2.2 Data

This work is based on the photometric data from several surveys, specifically *Gaia* DR2 [1](Gaia Collaboration et al., 2018d; Evans et al., 2018), Dark Energy Survey (DES) DR1 (Abbott et al., 2018) and Legacy Survey (Dey et al., 2019). In the next sections we briefly introduce these data in the context of measuring precise distances to BHB stars in dwarf galaxies.

2.2.1 *Gaia* photometry

Gaia satellite was launched in December 2013 (Gaia Collaboration et al., 2016a) and produced the second data release *Gaia* DR2 in Apr 2018. The *Gaia* dataset includes a large set of astrometric measurements for more than a billion sources, but also provides an exquisite space-based multi-band all-sky photometry in three bands. The broad *Gaia* G band covers the wavelength range from 330 to 1050 nm measured for almost 1.7 billion sources with typical uncertainty of 2 mmag at G=17 mag and 10 mmag at G=20 mag (Gaia Collaboration et al., 2018d; Evans et al., 2018). The two other *Gaia* photometric bands are the BP and RP that cover respectively the blue and red wavelength ranges (330 nm to 670 nm and 620 nm to 1050 nm). Due to the fact that the BP and RP photometry is measured by integrating over the dispersed spectra, the BP and RP photometry is significantly less precise than the G photometry with typical uncertainty of 200 mmag at G = 20.

The accuracy of the *Gaia* G band photometry and small level of systematics gives us possibility to explore the distance gradients in various dwarf galaxies based on photometric data alone.

2.2.2 DECaLS and DES photometry

DECaLS (DECam Legacy Survey) is a pre-imaging survey to the DESI spectroscopic survey, which uses the data collected at the Blanco telescope with the DECam camera (Flaugher et al., 2015). DECaLS data covers the entire South Galactic Cap and the $\delta \leq +34$ regions in the North Galactic Cap. DECaLS can reach magnitude limits of $g = 24$ and

[1]This paper is based on *Gaia* DR2, however we have verified that we obtain similar results if we substitute the DR2 data with *Gaia* EDR3. We have decided to stick with DR2 as the extinction prescription for DR2 from Gaia Collaboration et al. (2018b) has not been yet updated for DR3.

$r = 23.4$ (Dey et al., 2019) and the average uncertainty at 20 mag for the g and r band are 6 and 8 mmag. The DECaLS dataset also includes the sources extracted from data obtained as part of the Dark Energy Survey (DES)(Dey et al., 2019; Abbott et al., 2018) reduced using *The Tractor* software (Lang, Hogg, and Mykytyn, 2016), while the DES uses *PSFEx* (Bertin, 2011) and *SourceExtractor* (Bertin and Arnouts, 1996) to extract sources. Since in some areas of the DES footprint the DECaLS photometry is missing, we can rely on the catalogs from DR1 of DES instead.

2.2.3 Selection of BHB stars

To identify the BHB stars in the data we cross match *Gaia* with DECaLS data based on the sky position, and use G, BP and RP band from `gaia_source` table and g and r band measurements from DECaLS. The g and r band flux measurements are stored as nanomaggies in DECaLS and they are converted to magnitudes by using $\text{mag} = 22.5 - 2.5\log_{10}(\text{flux})$.

The magnitude limits we use are `phot_g_mean_mag` < 21 (Gaia Collaboration et al., 2018d), $g < 24.0$, $r < 23.4$ and $z < 22.5$ (Dey et al., 2019). We use objects with `type` = 'PSF' and `gaia_pointsource` = True in DECaLS data to select stars and `gaia_duplicated_source` = False to remove duplicate sources.

The extinction for the *Gaia* G band is calculated by by using Equation 1 and Table 1 from Gaia Collaboration et al. (2018b) and the extinction for DECaLS photometry is calculated by using coefficients $A/E_{(B-V)} = 3.995, 3.214, 2.165$ for g, r, z band, taken from DECaLS website which is computed as in Schlafly and Finkbeiner (2011). Since we use SFD dust map (Schlegel, Finkbeiner, and Davis, 1998), we also apply 14% recalibration of SFD which is reported by Schlafly et al. (2010) when calculating the extinction for the *Gaia* G band (but not for the g, r, z bands, as coefficients from Schlafly and Finkbeiner (2011) include the correction).

The colour range we used for selection of BHB stars is $-0.3 < g - r < 0$. We also use a $g - r$, $r - z$ colour-colour boundary based on the Equation 6 of Li et al. (2019) to remove possible blue stragglers contaminants.

$$\begin{aligned} r - z - 0.1 \leq & 1.07163(g-r)^5 - 1.42272(g-r)^4 \\ & + 0.69476(g-r)^3 - 0.12911(g-r)^2 \\ & + 0.66993(g-r) - 0.11368 \leq r - z + 0.1 \end{aligned} \tag{2.1}$$

We change the upper bound from $r - z$ to $r - z + 0.1$ and add the lower bound $r - z - 0.1$ comparing to the Li et al. (2019) original selection to keep as many as possible BHB stars and remove the quasars. We also apply a selection in absolute magnitude in *Gaia* G band ($0 < M_G < 1$) and we will describe how to calculate M_G in Section 2.2.5.

The selections described above are used for all the dwarf galaxies except Sculptor. The DECaLS does not have full coverage for Sculptor so we use DES DR1 data instead. And the selection for Sculptor is the same for *Gaia* data part. For the DES data, the magnitude limit is $g < 24.33$, $r < 24.08$ and $z < 22.69$. We use `EXTENDED_COADD` $<= 1$ and $-0.05 <$ `spread_model_i` < 0.05 to select stars, and we use `imaflags_iso_[grz]` $= 0$ and `flags_[grz]` < 4 to select high quality data (Abbott et al., 2018). The extinction calculation, BHB stars colour selection and colour-colour boundary are the same as described above.

Due to the magnitude limit of *Gaia* G band, in this paper we select the dwarf galaxies with BHB stars' G band magnitude less than 21. We will select a circle sky coverage with radius equal to five times half-light radius for each dwarf, and we require that the dwarf galaxy has more than 20 potential BHB stars for us to analyse after applying all the selection described above. We also remove the Sagittarius from the list due to heavy

contamination. Using the dwarf galaxies list, dwarf centre, distance moduli and half-light radius from McConnachie (2012), this leaves us with Bootes I, Draco, Ursa Minor, Sculptor and Sextans.

2.2.4 BHBs in the centre

There is substantial evidence of metallicity gradients or distinct stellar components with different metallicities inside different dwarf galaxies (Battaglia et al., 2008; Walker and Peñarrubia, 2011; Kim et al., 2019; Cicuéndez and Battaglia, 2018). It is also known that the magnitude of BHBs stars is likely metallicity dependent (Sirko et al., 2004; Fermani and Schönrich, 2013). Given the lack of certainty in these calibrations, the modeling of BHB magnitude distribution when large metallicity gradients or spreads are present is not feasible. Thus for this paper we decide to not analyse stars within one half-light radius [2] of the centre to avoid these problems.

As an example, Figure 2.1 shows the distance modulus ($m_G - M_G$) distribution in radial distance system of BHB stars from Sculptor, where m_G is apparent magnitude in *Gaia* G band and M_G is the absolute magnitude in *Gaia* G band calculated by using the formula in Section 2.2.5. We can see that the stars from inner part have larger distance modulus dispersion than stars from outer part, and our model won't consider the effect of different metallicity components, so we will remove all the blue points in the Figure 2.1.

2.2.5 Distance modulus of BHB

With the BHB selection described in previous two sections, the next step to the calculation of distance gradients is the calculate the distance moduli for individual BHB stars.

BHB stars have almost constant absolute magnitude because of narrow range of masses in the helium burning stage (Iben and Rood, 1970; Faulkner and Iben, 1966; Strom et al., 1970), which makes them excellent distance tracers and have been studied extensively (Pier, 1983; Sommer-Larsen, Christensen, and Carter, 1989; Clewley et al., 2002; Sirko et al., 2004). Work by Deason, Belokurov, and Evans (2011) shows the absolute magnitude slightly depends on the colour. The previous work on colour vs absolute magnitude relation of BHB stars is not based on *Gaia* photometry, so in this paper we determine a new absolute magnitude-color relationship for the *Gaia* G band. And as we discussed in Section 2.2.1, *Gaia* BP and RP bands have a substantial uncertainty at $G \sim 20$ mag, and most of our target dwarfs have BHB stars which are close to $G \sim 20$, so we decide to determine the relation between Gaia G vs DECaLS/DES colour $g - r$.

To determine the best absolute magnitude vs colour relation for the blue horizontal branch stars we ideally want to use the data for all the dwarf galaxies in our sample. For this we need to shift the photometric data for each dwarf galaxy by their corresponding distance modulus. The problem however is that literature distance moduli from McConnachie (2012) are in fact inconsistent with the data we have at hand. The 2-D histogram in the left panel of Figure 2.2 shows the colour-absolute magnitude distribution of all dwarfs where absolute magnitude is calculated with distance moduli from McConnachie (2012). We see that the horizontal branch is clearly much thicker than it is expected, indicating incorrect/inconsistent distances in the catalog. To correct for that we adopt the following iterative procedure. We first use the distances from McConnachie (2012) to fit for the absolute magnitude vs colour relation (left panel of Figure 2.2). Then we use the fitting result to fit a refined distance modulus for each dwarf separately, and

[2] We chose the radius based on the observed larger spread in the centers that we believe is caused by metallicity effects. We also ran several tests where we varied this masking radius to verify that our results are not too sensitive to it. The details are shown in Appendix A.1.

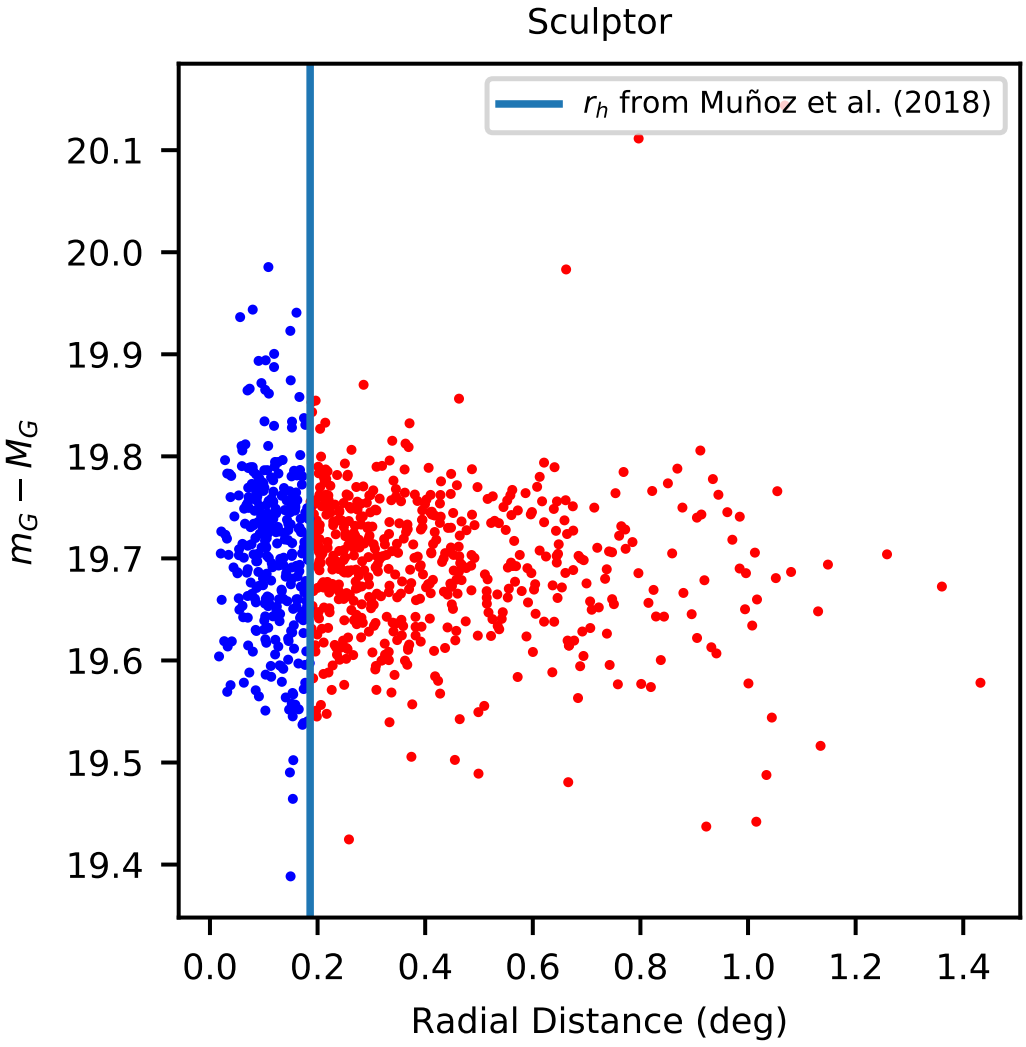

FIGURE 2.1: The distance modulus to BHB stars vs radial distance from the centre in Sculptor dwarf galaxy. The vertical line marks half-light radius from Muñoz et al. (2018), we can see the BHB stars which are inside half-light radius have larger dispersion than stars in the outer part.

finally use the refined distance moduli to fit the the absolute magnitude vs colour relation again (right panel of Figure 2.2).

We use six-knot cubic spline with not-a-knot end condition to model absolute magnitude vs colour relation. The BHB data for fitting is selected as we describe in Section 2.2.3 with M_G calculated with corresponding distance moduli data in each step. The whole fitting is done in three steps:

1. We use distance moduli from McConnachie (2012) to calculate M_G in this step. To build the model for fitting, we uniformly divide the colour range into 10 bins and use a mixture model for each bin with a different fraction of member BHB stars, which are assumed to have a Gaussian distribution in M_G. The other stars are assumed to have a uniform distribution in M_G. We also assume there is an extra uncertainty on M_G which changes with colour bin to accommodate the intrinsic uncertainty of M_G and the uncertainty on the distance modulus. We use maximum likelihood estimation to fit the model and the likelihood is shown below:

$$\begin{aligned} L &= P\left(M_G \mid S, \sigma_i, \alpha_i, g-r\right) \\ &= \alpha_i \mathcal{N}_{trunc}\left(M_G \mid f\left(\left(g-r\right) \mid S\right), \sigma_i\right) + \left(1-\alpha_i\right)\frac{1}{\Delta M_G} \end{aligned} \tag{2.2}$$

   where S is the set of M_G values of the knots of spline, i is the index of the colour bin the star belongs to, σ_i is the intrinsic dispersion for i-th colour bin, α_i is the fraction of member BHB stars in the i-th colour bin, $\mathcal{N}_{trunc}$ is normal distribution truncated from 0 to 1, f is spline function and $\Delta M_G = 1$ which is the width of M_G range that we fit.

2. Then we refine the distance to each dwarf. We use colour-absolute magnitude relationship from previous steps to fit for distance modulus for each dwarf. When fitting distance modulus, we use the same mixture model as in step (i) except we use a colour independent intrinsic dispersion and add distance modulus parameter for this fitting. We use maximum likelihood estimation and the likelihood is shown below:

$$\begin{aligned} L &= P\left(m_G \mid d, \sigma, \alpha_i, S, g-r\right) \\ &= \alpha_i \mathcal{N}_{trunc}\left(\left(m_G-d\right) \mid f\left(\left(g-r\right) \mid S\right), \sigma\right) \\ &\quad + \left(1-\alpha_i\right)\frac{1}{\Delta M_G} \end{aligned} \tag{2.3}$$

   where d is the distance modulus, S is the set of M_G values of the nodes of spline, i means the colour bin the star belongs to, σ is intrinsic dispersion, α_i is the member fraction in the i-th colour bin, m_G is the apparent magnitude in *Gaia* G band, $\mathcal{N}_{trunc}$ is normal distribution truncated from 0 to 1, f is spline function and $\Delta M_G = 1$ which is the width of M_G range that we fit. Unlike Equation 2.2, we use a colour independent intrinsic dispersion σ in this model to reduce the model complexity as we find that the intrinsic dispersions σ_i in Equation 2.2 are very close.

3. Then we replace the distance moduli in step (i) by the refined distance moduli from step (ii), and keep repeating step (i) and (ii) until convergence. It takes four iterations to get the converged distance moduli. The results are shown in the Table 2.1. We note that the distance moduli determined by our method are determined up to a constant offset common between all the galaxies as we did not calibrate the zero

TABLE 2.1: The table for literature distance moduli $m - M$ from McConnachie (2012) for dwarf galaxies we analysed and our refined distance moduli $(m_G - M_G)_{\rm fit}$.

Dwarf	$m - M$	$(m_G - M_G)_{\rm fit}$
Bootes I	19.11	19.129
Draco	19.4	19.679
Ursa Minor	19.4	19.326
Sculptor	19.67	19.678
Sextans	19.67	19.781

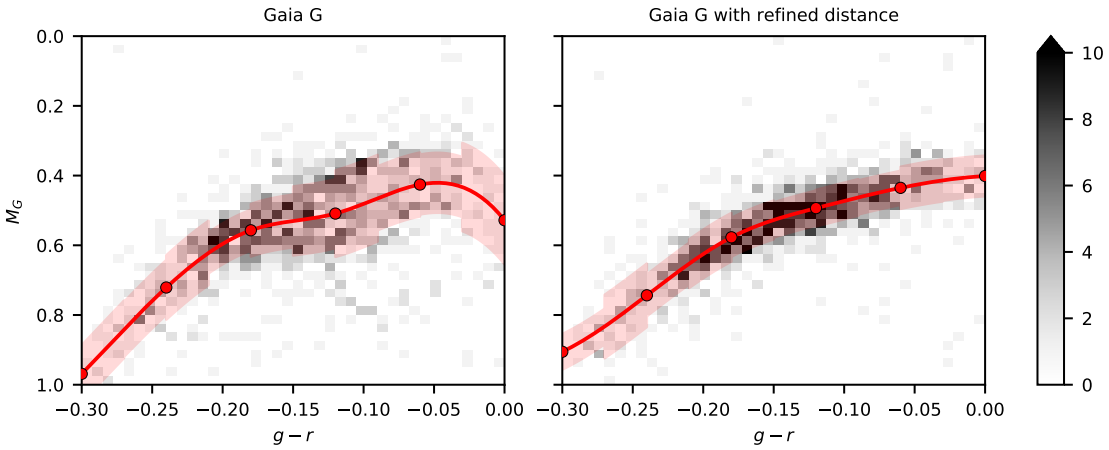

FIGURE 2.2: The graph shows the results of fitting BHB colour-absolute magnitude. The colour is DECaLS/DES g-r and the absolute magnitude is calculated from Gaia G band. The left panel is using distance moduli from (McConnachie, 2012) and the right panel is using refined distance moduli which are shown in Table 2.1. In both panels we show the 2-D histogram in colour-magnitude space for possible BHBs from Bootes I, Draco, Ursa Minor, Sextans and Sculptor. The red line is a best fit spline, the red semi-transparent region shows the fitted intrinsic dispersion; the red dots are the spline knots.

point of the absolute magnitude vs colour curve. This will not affect our analysis we are interested in distance modulus gradients.

4. Finally we fit the relation of colour vs absolute magnitude again as in step (i) but now using the converged distance moduli from step (iii).

Figure 2.2 shows plots of all these dwarfs' BHB in colour-magnitude diagram and our fitting results. The left panel is the result of step (i) and right panel is the result of step (iv). The average σ_i over all the bins is 0.092 for fitting with distance moduli from McConnachie (2012) and 0.059 for fitting with refined distance moduli, which demonstrates that improved distance moduli give a tighter colour-magnitude relation for BHBs. We can also see that by visually comparing the density distribution in the left panel with the right panel of the Figure 2.2; the density distribution in the left panel shows larger dispersion than the right panel. The BHB spline track shown on the right panel will be used for calculating distance modulus for each BHB star. The knots of the spline are given in Table 2.2. The selection from Section 2.2.3 will use M_G values calculated using refined distance moduli in further analysis.

TABLE 2.2: The spline knots for the g-r colour and M_G relationship.

$g-r$	-0.3	-0.24	-0.18	-0.12	-0.06	0
M_G (mag)	0.906	0.743	0.577	0.493	0.435	0.401

2.3 The distance gradient of BHBs

Our objective is to constrain the dwarf galaxies 3-D shapes. Here we will assume that the BHB stars in dwarf have the same 3-D spatial shape as the other stars. Under this assumption, we can get the information of a dwarf galaxy shape by modeling the distribution of BHB stars. As we discussed in Section 2.2.5, BHBs allow us to calculate distance along the line of sight, thus probing not only projected distribution of objects but also the actual 3-D structure.

In this section we will first describe the morphological parameters we use for 2-D spatial distribution of each dwarf galaxy, followed by the description of the model of distance gradient and its measurements for Bootes I, Draco, Ursa Minor, Sextans and Sculptor.

2.3.1 The spatial distribution of BHBs

We use a 2-D elliptical Plummer density distribution (Plummer, 1911) to model the spatial 2-D density distribution for each dwarf galaxy. Given that there are several studies showing that BHB stars can be more spatially extended than other stellar populations (Bellazzini, Ferraro, and Pancino, 2001; Okamoto et al., 2017; Coleman, Da Costa, and Bland-Hawthorn, 2005), we decided to fit the distribution of BHB stars and check the consistency of half-light radius (r_h) between our fitting result and value from Muñoz et al. (2018). If two values are consistent we use Plummer parameters from Muñoz et al. (2018), otherwise we use half-light radii from our BHB models and all other parameters in Plummer model from Muñoz et al. (2018) to model density distribution. In this way we can make sure the half-light radius is consistent with data and take advantage of the morphological parameters from Muñoz et al. (2018) which have small uncertainties. The model we use is a mixture model of Plummer distribution for member stars and uniform distribution for background, and the likelihood function is given below:

$$\begin{aligned} L &= P(x, y \mid x_0, y_0, r_h, \theta, \epsilon) \\ &= \alpha_{mem}\rho(x, y \mid x_0, y_0, r_h, \theta, \epsilon) + \frac{1-\alpha_{mem}}{\Delta S} \end{aligned} \tag{2.4}$$

where α_{mem} is the fraction of member stars, x, y are position in a Cartesian coordinate with units degrees where x direction is along RA and y direction is along Dec , ρ is normalized 2-D elliptical Plummer density distribution within the modeled footprint, x_0, y_0 are the centre of the dwarf galaxy, r_h is the half-light radius, θ is the position angle of semi-major axis, ϵ is the ellipticity and ΔS is the area of modeled footprint. We use Markov chain Monte Carlo (MCMC) and uniform prior on all parameters to get the posterior mean and 1σ level uncertainty of the half-light radius for the distribution of BHB stars.

We find only Sextans and Sculptor have posterior mean half-light radii inconsistent with the value from Muñoz et al. (2018). The half-light radius in Plummer model from Muñoz et al. (2018) is 11.17 ± 0.05 arcmin for Sculptor and 16.5 ± 0.10 arcmin for Sextans, while the half-light radius given by ou r posterior mean is 15.14 ± 0.67 arcmin for Sculptor and 43.3 ± 3.8 arcmin for Sextans. We note that our half-light radius for BHB stars in Sextans has large difference compared with 27.80 ± 1.20 arcmin in McConnachie

(2012), 16.5 ± 0.10 arcmin in Muñoz et al. (2018) and 19.48 ± 0.35 arcmin in Moskowitz and Walker (2020), we think the reason is that the BHB stars are much more extended than than other population in Sextans. Cicuéndez et al. (2018) also shows the half-light radius for BHB stars in Sextans is 42 ± 7 arcmin which is consistent with our result. We decide to use half-light radii from our model for Sextans and Sculptor. The centre of dwarf galaxy, ellipticity and position angle of semi-major axis for Sextans and Sculptor are still taken from Muñoz et al. (2018). For other dwarf galaxies all morphological parameters are taken from Muñoz et al. (2018). When masking the centre BHB stars as we said in Section 2.2.4 and performing 3-D model fitting, we always use half-light radius from Muñoz et al. (2018).

2.3.2 BHB distance gradient model

With the model of density distribution, we can construct the model for the distance gradient. Since the adopted selection of BHB candidates (see Section 2.2.3) still includes some foreground contaminant stars on top of BHBs, in order to be able to extract a possible distance gradient we adopt a mixture model for the magnitude distribution.

To model the distribution of BHB's distance moduli, we assume that for member BHBs it linearly depends on the position in the galaxy

$$\mu_{\text{predict}} = c_0 + c_{\text{major}} x_{\text{major}} + c_{\text{minor}} x_{\text{minor}} \tag{2.5}$$

where μ_{predict} is average distance modulus at a given location, x_{major} and x_{minor} are coordinates along semi-major and semi-minor in degrees and c_{major} and c_{minor} are distance modulus gradients along semi-major/semi-minor axis. We also assume that the observed distance moduli of individual stars are normally distributed around the prediction as shown below:

$$\mu \sim \mathcal{N}(\mu_{\text{predict}}, \sqrt{\sigma_{\text{data}}^2 + \sigma_0^2}) \tag{2.6}$$

where μ is the distance modulus of individual BHB star, σ_{data} is the uncertainty of the observed distance modulus due to photometric errors and σ_0 is the intrinsic dispersion. The intrinsic dispersion of the calculated BHB absolute magnitudes can be caused by both intrinsic spread of absolute magnitudes of BHBs (i.e. due to age/metallicity spread) or physical distance spread. For the foreground contaminants we assume that distance moduli are uniformly distributed in the selected magnitude range. We note that some foreground contaminants are not necessarily BHBs at correct distance, i.e. they can be more nearby blue stragglers, however this is not an issue for our model as we are not interested in the true distances to the contaminant population.

To take into account different spatial distribution for member stars and contaminant stars, we assume Plummer distribution for dwarf galaxy member stars and uniform distribution for contaminant stars (described in Section 2.3.1). By combining the spatial distribution model with magnitude distribution we can write down the likelihood function.

$$\begin{aligned} L &= P\left(x_{\text{major}}, x_{\text{minor}}, \mu | c_0, c_{\text{major}}, c_{\text{minor}}, \Phi, \sigma_0\right)\right) \\ &= \Phi\beta\rho(x_{\text{major}}, x_{\text{minor}})\mathcal{N}(\mu \mid \mu_{\text{predict}}, \sqrt{\sigma_{\text{data}}^2 + \sigma_0^2}) \\ &\quad + (1-\Phi)\frac{1}{S}\frac{1}{\Delta\mu} \end{aligned} \tag{2.7}$$

TABLE 2.3: Distance gradient model parameters and their priors. $m_G - M_G$ is the refined distance modulus which is shown in Table 2.1.

Parameter	Comment	Prior
c_0 (mag)	Distance modulus at the centre of galaxy	U[-3+$(m_G - M_G)$, 3+$(m_G - M_G)$]
$c_{\rm major}$ (mag/deg)	Distance gradient along semi-major axis	U[-5, 5]
$c_{\rm minor}$ (mag/deg)	Distance gradient along semi-minor axis	U[-5, 5]
σ_0 (mag)	Intrinsic distance dispersion	U[0, 1]
Φ	Fraction of member stars	U[0, 1]

TABLE 2.4: 3D shape model parameters and their priors.

Parameter	Comment	Prior
A (deg)	Longest principal axis of ellipsoid	U[0.1, 1]
ϵ_{3d}	Ellipticity of ellipsoid	U[0, 1]
η	Triaxiality of ellipsoid	U[0, 1]
$\cos\theta_{\rm axis}$	$\theta_{\rm axis}$ is a polar angle of the rotation axis	U[-1, 1]
ϕ (rad)	Azimuthal angle of the rotation axis	U[0, 2π]
$\psi - \sin\psi$	ψ is a rotation angle	U[0, π]

Φ is fraction of member stars, $\rho(x_{\rm major}, x_{\rm minor})$ is a normalized 2-D elliptical Plummer density distribution within the modeled footprint, S is the area of selected sky coverage, $\Delta\mu$ is the width of selected magnitude range. β is normalization factor for the Gaussian given that we only model a finite interval in distance modulus, the equation is shown below,

$$\beta = 1 \Big/ \int_{\mu_{min}}^{\mu_{max}} \mathcal{N}(\mu \mid \mu_{\rm predict}, \sqrt{\sigma_{\rm data}^2 + \sigma_0^2})) \, d\mu \tag{2.8}$$

2.3.3 Gradient fit results

Using the models described in the previous section we can obtain the posterior distribution of distance gradient (c_{major}, c_{minor}). We use MCMC to sample the posterior while adopting a uniform prior for all the parameters. The priors are specified in the Table 2.3.

The posterior mean of intrinsic dispersion σ_0 for these dwarf galaxies is between 0.023 and 0.064, which is close to the intrinsic dispersion in the absolute magnitude-colour relationship fitting from Section 2.2.5, and the posterior mean of member fraction Φ is between 0.72 and 0.96 which shows most of stars are from targeted galaxies. Figure 2.3 shows marginal posteriors for measured distance gradients in five dwarf galaxies that we analyze. The zero gradient is marked by dashed lines. Instead of showing the distance modulus gradients in mag/deg as given in Equation 2.5, we convert them into dimensionless gradients along semi-major/semi-minor axis.

$$\begin{aligned} \hat{c}_{major} = \frac{\partial d}{\partial \hat{x}_{major}} &= \frac{\partial d}{\partial (m_G - M_G)} \frac{\partial x_{major}}{\partial \hat{x}_{major}} \frac{\partial (m_G - M_G)}{\partial x_{major}} \\ &= \frac{36 \ln(10)}{\pi} \frac{\partial (m_G - M_G)}{\partial x_{major}} \\ \hat{c}_{minor} = \frac{\partial d}{\partial \hat{x}_{minor}} &= \frac{36 \ln(10)}{\pi} \frac{\partial (m_G - M_G)}{\partial x_{major}} \end{aligned} \tag{2.9}$$

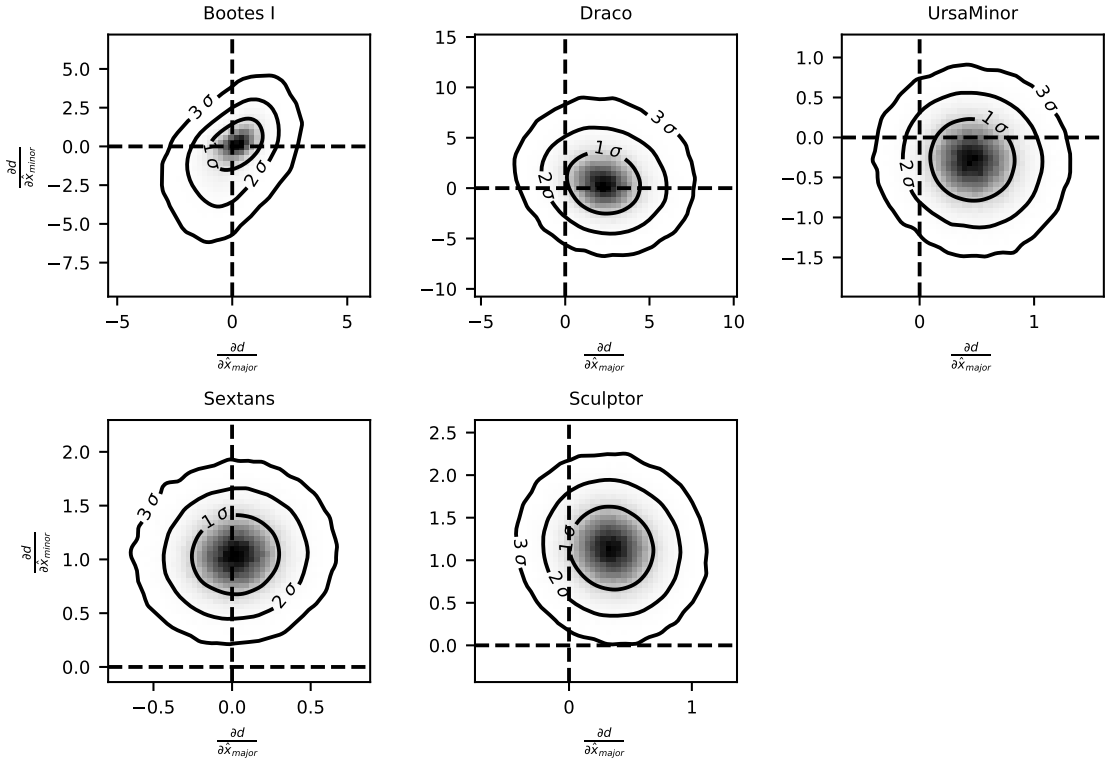

FIGURE 2.3: The marginal posterior distribution of distance gradient along semi-major and along semi-minor axes for different dwarf galaxies. d is the distance in pc, $\hat{x}_{\rm major}$ and $\hat{x}_{\rm minor}$ are the coordinates aligned with the major/minor axes of each dwarf in pc. The zero gradient is marked by the dashed line.

where x_{major}, x_{minor} are the coordinates on the sky aligned with the major/minor axis expressed in degrees, and $\hat{x}_{major}, \hat{x}_{minor}$ are the same coordinates expressed in physical units (pc), d is the line of sight distance in pc. If we assume the galaxy has an oblate or prolate shape, then the dimensionless $\hat{c}_{major}$ and $\hat{c}_{minor}$ depend on inclination (i), we will have $\hat{c}_{minor} = \tan(i), \hat{c}_{major} = 0$ for an oblate shape and $\hat{c}_{major} = \tan(i), \hat{c}_{minor} = 0$ for a prolate shape.

In the Figures 2.3, Sextans and Sculptor show distance gradient at the level above 3 sigma significance. In the case of dwarf galaxies Bootes I, Draco and Ursa Minor, the observed distance gradient is consistent with zero.

Even though we do not observe statistically significant non-zero distance gradient in Bootes I, Draco and Ursa Minor, that is probably because the number of stars is too small and the uncertainty is too large to show any possible distance gradient. A recent paper by Muraveva et al. (2020) observes the possible difference of distance between the eastern and western regions of Draco by using RR Lyrae stars, however the error is still too large to get statistically significant conclusion.

We notice that in the case of Sextans and Sculptor the gradient seems to be mostly along the semi-minor axis. We will discuss the implication of this for choosing 3-D model in the next section.

2.4 The 3-D structure of galaxy

The results shown in the previous section provide us with the evidence of the distance gradient in two dwarf galaxies. To be able to further investigate the intrinsic 3-D shapes of the Sextans and Sculptor in this section we will construct a 3-D ellipsoidal model to distance gradient and 2-D density distribution of Sextans and Sculptor.

2.4.1 3-D structure model

We assume the 3-D structure of each dwarf galaxy has a shape of an ellipsoid. As it is often done in the literature to parameterize the ellipsoid we use the 3-D major axis, intrinsic ellipticity and triaxiality. I.e. if we assume the three principal axes of an ellipsoid are A, B, C with $A \geq B \geq C$, then 3-D major axis is defined as A, intrinsic ellipticity (or flattening) is defined as $\epsilon_{3d} = 1 - \frac{C}{A}$ and triaxiality is defined as $\eta = (1 - \frac{B^2}{A^2})/(1 - \frac{C^2}{A^2})$ (Franx, Illingworth, and de Zeeuw, 1991) .

In this paper we focus on 3 families of ellipsoids. The first one is a general triaxial ellipsoid model that allows arbitrary intrinsic major axis, intrinsic ellipticity and triaxiality. The second family is oblate ellipsoid model (disc-shaped model) which has triaxiality equal to 0, and the last one is prolate ellipsoidal model (cigar-shaped model) which has triaxiality equal to 1.

For each triaxial model we also need to parameterize the orientation of an ellipsoid. This is done by the axis-angle representation, where we parameterize rotation axis by using polar angle θ_{axis} and azimuthal angle ϕ and we denote rotation angle by ψ. The polar angle and azimuthal angle is based on a spherical coordinate system where zenith direction is along line of sight and azimuth reference direction is along RA. We use rotation matrix $R(\theta_{\text{axis}}, \phi, \psi)$ to describe the rotation from the longest principal axis to the RA direction.

With this parameterization and the assumption of the 3-D Plummer profile, we can write the density distribution for our ellipsoid model with principal axes A, B and C:

$$\rho(x, y, z) = \frac{3N}{4\pi} \left(1 + X^T R^T S R X\right)^{-\frac{5}{2}} \frac{1}{ABC} \tag{2.10}$$

where N is the total number of stars, R is the rotation matrix described above, S is diagonal matrix with diagonal elements $(1/A^2, 1/B^2, 1/C^2)$, and X is the coordinate in a Cartesian coordinate system where x direction is along RA, y direction is along Dec and z direction is along line of sight.

From the 3-D density distribution, we are able to determine the projected semi-major axis of the stellar distribution (r_{major}), 2-D ellipticity (ϵ_{2d}), positional angle (θ_{pos}) and the average gradient of the distance along z axis (line of sight direction) across the body of the galaxy.

$$h(x, y) = \frac{\int_{-\infty}^{+\infty} \rho(x, y, z) z \, dz}{\int_{-\infty}^{+\infty} \rho(x, y, z) \, dz} = c_x x + c_y y + c_0 \tag{2.11}$$

where c_x and c_y are average distance gradients along x axis and y axis respectively. We then project the distance gradient along semi-major and semi-minor direction to the x and y direction when doing 3-D model fitting. For the Plummer distribution the calculation of these parameters can be done symbolically. See Appendix A.2 for the Mathematica code we use to do this calculation. We note that the definition of distance gradient we use in Equation 2.11 assumes the observer is at a infinite distance, while the actual observer has a finite distance to the dwarf galaxy. This difference is negligible in our case.

We then model the observed parameters such as 2-D semi-major axis and semi-minor axis, 2-D position angle of semi-major axis and distance gradient using the model described above. We assume that the measured parameters have Gaussian uncertainties. Based on this assumption we construct the likelihood function:

$$\begin{aligned} L_{3d} &= P\left(\hat{r}_{\rm major}, \hat{r}_{\rm minor}, \hat{\theta}_{\rm pos}, \hat{c}_x, \hat{c}_y | A, \epsilon_{3d}, \eta, \theta_{\rm axis}, \phi, \psi\right) = \\ &= \mathcal{N}\left(\hat{r}_{\rm major} \mid r_{\rm major}, \sigma_{r_{\rm major}}\right) \mathcal{N}\left(\hat{r}_{\rm minor} \mid r_{\rm minor}, \sigma_{r_{\rm minor}}\right) \\ &\quad \times \mathcal{N}\left(\hat{\theta}_{\rm pos} \mid \theta_{\rm pos}, \sigma_\theta\right) \mathcal{N}\left(\hat{c}_x \mid c_x, \sigma_x\right) \mathcal{N}\left(\hat{c}_y \mid c_y, \sigma_y\right) \end{aligned} \tag{2.12}$$

$\hat{r}_{\rm major}, \hat{r}_{\rm minor}, \hat{\theta}_{\rm pos}$ are projected semi-major axis, projected semi-minor axis and position angle of dwarf galaxy, $\hat{c}_x, \hat{c}_y$ are gradient along x axis and y axis which is projected from gradient along semi-major and semi-minor axes of dwarf galaxy, all the σ are the uncertainty of the corresponding parameters of dwarf galaxy, and $r_{\rm major}, r_{\rm minor}, \theta_{\rm pos}, c_x, c_y$ are corresponding parameters calculated from 3-D model parameterised by $A, \epsilon_{3d}, \eta, \theta_{\rm axis}, \phi, \psi$.

2.4.2 Distance gradient under different 3-D shapes

Before looking at the results of the modeling we first look at several simulations to build intuition on how ellipticity and triaxiality control the distance gradient. Following the definition of distance gradient in Section 2.4.1, we calculate the possible distance gradient for shapes with different ellipticity and triaxiality. For each combination of ellipticity and triaxiality, we calculate the distance gradients under all possible rotations, and draw regions of possible distance gradients along two axes. The results are shown in Figure 2.4. The left panel shows the boundary of the distance gradient distribution when the models have fixed ellipticity 0.7 but different triaxiality, and the right panel shows the same thing when the models have fixed triaxiality 0.7 but different ellipticity. From the left panel we can see that oblate shape (triaxiality $= 0$) has zero gradient along semi-minor axis and prolate shape (triaxiality $= 0$) has zero gradient along semi-major axis, and the triaxiality controls the ratio of the maximum gradient along semi-major axis to the maximum gradient along semi-minor axis. The right panel shows ellipticity controls the maximum magnitude of the gradient. Based on the results from Section 2.3.3 where the gradient of Sextans and Sculptor seems to be mostly aligned along the semi-minor axis, the prolate shape is expected to be incompatible with Sextans and Sculptor, so we will only model them with triaxial and oblate shapes.

2.4.3 3-D shape fit results

Using the models we described in Section 2.4.1, we can sample the posterior distribution of each model to infer the the possible intrinsic 3-D shape. Similarly to previous analyses we use MCMC to sample the posterior of our 3-D shape model, and the priors are given in Table 2.4. The specific prior for rotation angle ψ from axis-angle representation $(\psi - \sin\psi) \sim U[0, \pi]$ is to make sure the sampled rotation matrix from the prior is uniformly distributed with respect to the Haar measure on SO(3) (Miles, 1965).

Figure 2.5 shows the posterior distribution for the parameters of the 3-D model for the oblate and triaxial shapes based on Sextans data. For the triaxial model (left panel), we see that the peak of triaxiality distribution is at zero and the 95% credible interval for intrinsic ellipticity is $[0.48, 1]$ with peak at 0.6. This says that in order to be consistent with the observed distance gradient and shape the system needs to be quite flattened and of oblate shape. The right panel of the figure shows the posterior for the oblate model, and it provides similar intrinsic ellipticity constraints $[0.47, 1]$.

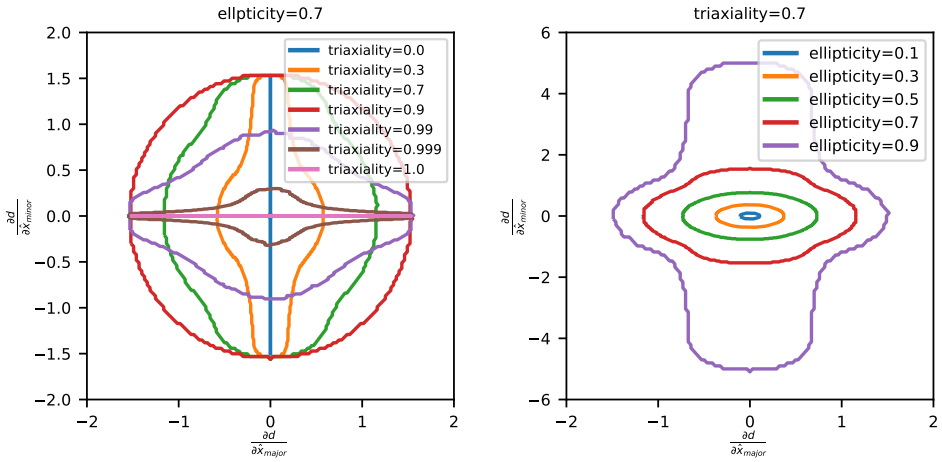

FIGURE 2.4: Possible distance gradient values of ellipsoids with different ellipticities and triaxialities along minor $\frac{\partial d}{\partial x_{min}}$ or major axes $\frac{\partial d}{\partial x_{maj}}$. d is the distance in pc, $\hat{x}_{\rm major}$ and $\hat{x}_{\rm minor}$ are the coordinates aligned with the major/minor axes in pc. In each panel, different colors represent ellipsoids of different ellipticities and triaxialities. For each ellipsoid the corresponding line shows the boundary of the region of possible distance gradients. I.e. for a triaxial ellipsoid with ellipticity of 0.7 and triaxiality of 0.3 the measured gradients can only be sit within the orange countour depending on the orientation.

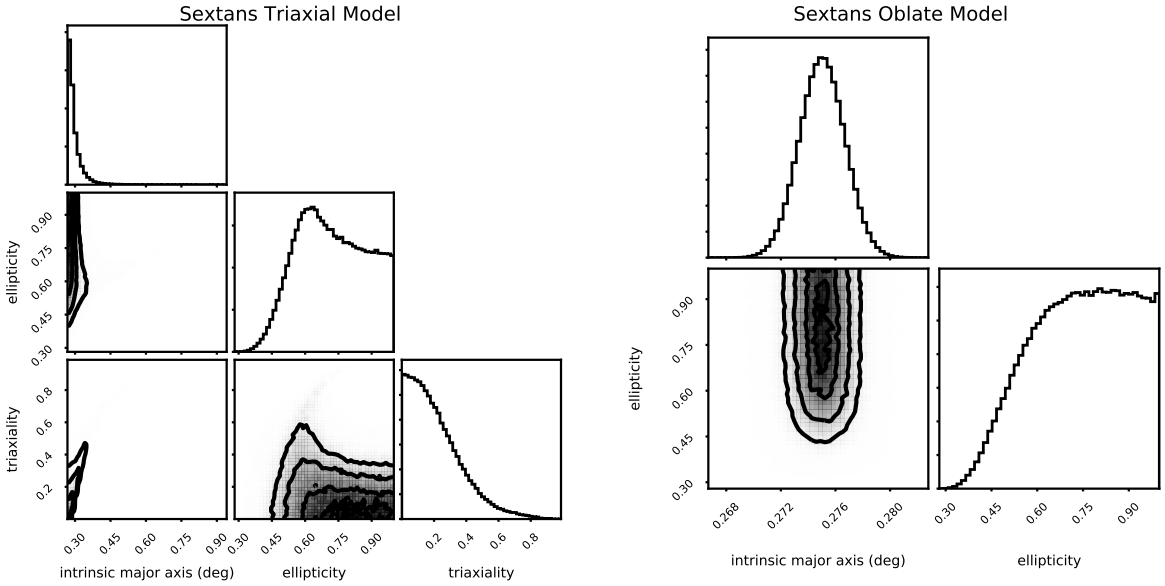

FIGURE 2.5: Posterior probability distributions of the parameters of the 3-D model of Sextans. The left panel shows the results for the triaxial model, while the right one shows the oblate model. We do not show here the orientation parameters.

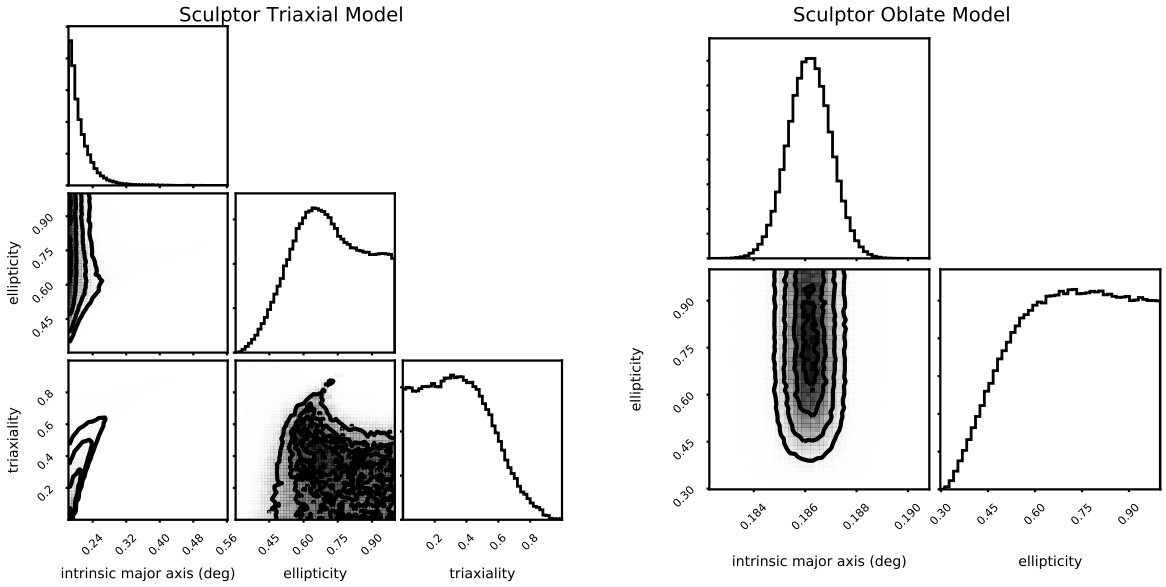

FIGURE 2.6: Posterior probability distributions of the parameters of the 3-D model of Sculptor. The left panel shows the results for the triaxial model, while the right one shows the oblate model. The orientation parameters are not shown.

Figure 2.6 shows the posterior distribution for the parameters of the 3-D model for the oblate and triaxial shapes based on Sculptor data. For the triaxial model (left panel), we see that there is a broad peak in triaxiality distribution at 0.4 and the 95% credible interval for it is $[0, 0.71]$, which suggests the oblate is possible for Sculptor but the triaxial model doesn't show strong preference for oblate shape. The 95% credible interval for intrinsic ellipticity is $[0.46, 1]$ with the peak at 0.7. The right panel of the figure shows the posterior for the oblate model, and it provides similar flattening constraints as the triaxial model.

To validate that the 3-D model can actually fit the measurements we perform posterior predictive checks (Gelman et al., 2013) by comparing the measured distance gradient and 2D Plummer parameters to the predicted values based on the samples from the posterior. We check the agreement by computing one tail p-values for each parameter. For Sextans, the one tail p-values are well within $[0.30, 0.5]$ which indicates that the models are in agreement with the data. For Sculptor, the p-values for most parameters are well within $[0.26, 0.5]$ except for the p-value for gradient along semi-major is 0.059 for oblate model, which indicates the oblate model doesn't fit well to the gradient along semi-major axis. This is understandable since the oblate model is supposed to have exactly zero gradient along semi-major axis, but the last panel of Figure 2.3 shows the data is consistent with zero gradient along semi-major axis at 1σ and 2σ level. Considering the p-value is not extremely small, the oblate model is still acceptable for Sculptor data. The detailed posterior predictive check distributions for Sculptor are shown in the Appendix A.3.

2.4.4 Orientation of 3-D shape

With the posterior of the rotation parameters at hand, we can analyse the orientation of Sextans and Sculptor. Considering that direction of the the major axis of an oblate ellipsoid is not defined and the results of the triaxial model prefer the oblate shape, we decide to use the direction of minor axis as the orientation. To describe the orientation,

TABLE 2.5: Orientation results of Sextans and Sculptor. $\theta_{\rm vel}$ is the angle between the minor axis and the velocity of the dwarf. $\theta_{\rm centre}$ is the angle between the minor axis and the direction from the centre of the dwarf to the Galactic centre. We use 1 sigma level asymmetrical uncertainty

Galaxy	Model	$\theta_{\rm vel}$ (degree)	$\theta_{\rm centre}$ (degree)
Sextans	Oblate	$120.3^{+3.7}_{-3.4}$	$53.6^{+3.6}_{-3.3}$
Sextans	Triaxial	$122.5^{+7.9}_{-7.0}$	$56.1^{+7.9}_{-7.0}$
Sculptor	Oblate	$36.62^{+0.90}_{-0.96}$	$49.4^{+4.8}_{-4.3}$
Sculptor	Triaxial	$43.4^{+7.0}_{-6.8}$	$51.0^{+10}_{-8.8}$

we calculate the angle between the minor axis and the velocity of the dwarf ($\theta_{\rm vel}$) and the angle between the minor axis and the direction from the centre of the dwarf to the Galactic centre ($\theta_{\rm centre}$). We adopt the peculiar motion of the Sun from (Schönrich, Binney, and Dehnen, 2010), the Sun's distance to the Galactic centre of 8.3 kpc (Gillessen et al., 2009), and the position of the Galactic centre from (Reid and Brunthaler, 2004). We use the dwarfs' mean proper motions from Qi et al. (2021) and heliocentric velocity and heliocentric distances from McConnachie (2012).

We sample the rotation parameters from the posterior and the velocity and the distance from the literature values, then calculate $\theta_{\rm vel}$ and $\theta_{\rm centre}$. The mean value and the 1 sigma level asymmetric uncertainties are shown in Table 2.5. We notice the uncertainty of the oblate model is smaller than the uncertainty of the triaxial model, and we think the reason is that oblate model puts a stronger constraint on the possible orientation. The values listed in the Table 2.5 do not show clear alignment neither along the velocity of the dwarfs, nor towards the Galactic centre.

2.5 Discussion

In this section we will discuss possible implications of our measurements presented in Section 2.4.3, potential issues caused by non-axisymmetric metallicity distribution in the galaxies and the possibility of that the shape is the result of tidal disruption. We will discuss the consistency between our measurements and other paper. We also verify that our results are robust to small changes in extinction and the details of this check are shown in the Appendix A.4.

2.5.1 Intrinsic ellipticity and rotation

Taken at face value the measurements presented in Section 2.4.3 show that the the systems require significant flattening, which has implications on the dynamical structure the systems. Specifically we expect that if the flattening is strong enough that may be only possible if the system is rotating (Binney, 2005). Because the results from Section 2.4.3 show that both Sextans and Sculptor can have oblate shapes, it is possible for us to perform the consistency check between intrinsic ellipticity, anisotropy and rotation (which is constrained by existing observations).

Multiple studies (Hargreaves et al., 1994; Walker, Mateo, and Olszewski, 2008; Battaglia et al., 2011) show there isn't a statistically significant velocity gradient in Sextans, so we

need to check whether our intrinsic ellipticity is consistent with the observation of velocity gradient. From our 3-D model fitting results, we find the intrinsic ellipticity $1 - C/A$ for Sextans needs to be above 0.47, and according to Walker, Mateo, and Olszewski (2008) the 3σ upper bound for the absolute value of line of sight velocity gradient is $|-2.1 - 0.8 \times 3| = 4.5\ \mathrm{km\,s^{-1}\,deg^{-1}}$. Walker et al. (2009b) shows the velocity dispersion is 7.9 $\mathrm{km\,s^{-1}}$ in Sextans. To check whether these results are consistent, we can rely on the anisotropic rotating spheroids models presented in Emsellem et al. (2011), who provides the models for oblate with different tangential anisotropy and different amount of rotation measured by dimensionless parameter λ_R (Emsellem et al., 2007) which is defined as $\lambda_R \equiv \frac{<R|V|>}{<R\sqrt{V^2+\sigma^2}>}$ (here R is distance to the centre, V is mean stellar velocity and σ is mean stellar velocity dispersion and $<>$ refers to luminosity-weighted sky average).

The flattening of the object can be explained by both rotation and anisotropy of orbits (Binney, 1976; Binney, 1978). And for a fixed anisotropy we expect a monotonic relationship between intrinsic ellipticity and rotation. And higher anisotropy can support slower rotation at fixed flattening. With the velocity dispersion and velocity gradient limit of Sextans, we can estimate λ_R at half-light radius instead of taking luminosity-weighted sky average, which gives an upper bound $\lambda_R < 0.15$. Using the models presented in Appendix B of Emsellem et al. (2011) (see figure B4), we expect that the models with mild anisotropy $\beta \sim 0.4 - 0.6$ should be able to support flattened spheroids with $\epsilon \sim 0.5$ with small or no amount of rotation $\lambda_R \lesssim 0.2$, which is consistent with our estimation. Thus at the face value the flattened shape can be consistent with observed lack of rotation. We note that previous relation assumes that the dark matter density distribution follows the stellar density and the galaxy is axisymmetric(Cappellari et al., 2006).

We did the same analysis for oblate shape fitting result of Sculptor. We use 3σ upper bound for the absolute value of line of sight velocity gradient $|-5.5 - 0.5 \times 3| = 7$ $\mathrm{km\,s^{-1}\,deg^{-1}}$ (Walker, Mateo, and Olszewski, 2008) and velocity dispersion 9.2 $\mathrm{km\,s^{-1}}$ (Walker et al., 2009b) to estimate an upper bound $\lambda_R < 0.14$. The lower bound of intrinsic ellipticity from Section 2.4.3 is 0.46. We expect that the models with mild anisotropy $\beta \sim 0.4 - 0.6$ should be able to support flattened spheroids with $\epsilon \sim 0.5$ with small or no amount of rotation $\lambda_R \lesssim 0.2$, which is also consistent with our estimation.

2.5.2 Non-axisymmetric metallicity distribution in Sextans

Our modeling assumes that the stellar distribution is described by ellipsoids and the metallicity distribution is axisymmetric. If the galaxies have substructures with drastically different metallicities, these can affect BHB absolute magnitude calculation, and can mimick themselves as structures at different distances or distance gradients in our model.

One of two systems in which we have detected a significant gradient is Sextans, whose structure has been studied extensively and several possible non-axisymmetric substructures were detected (Kim et al., 2019; Cicuéndez and Battaglia, 2018).

According to the Figure 3 of Kim et al. (2019) and Figure 5 of Cicuéndez and Battaglia (2018), there are different metallicity components near the galaxy centre of Sextans. However the sky coverage in these two papers is not large enough and the different metallicity component which is shown in their figures is removed when we remove all the stars inside $1r_h$ as discussed in Section 2.2.4. Due to limited sky coverage, it is hard to conclude whether there is non-axisymmetric metallicity distribution in the BHB stars we used for the distance gradient fitting.

We also notice that the numbers of BHB stars at different sides of Sextans semi-major axis are somewhat different. Figure 2.7 shows the histogram of distance modulus for two galaxy sides ($x_{minor} > 0$ is northwest side and $x_{minor} < 0$ is southeast side) without

removing the stars within $1r_h$ of Sextans, and the number of BHB stars at northwest side is larger than the other side by a factor of 1.24. The side with more BHB stars is the same side where Kim et al. (2019) claims there is a overdensity of metal-poor stars. Due to the limit of their sky coverage and the small number of BHB stars in the centre region, we cannot get a reliable conclusion about whether the this overdensity is related with the difference of number of BHB stars between different side of semi-major axis. We did a similar analysis of the BHB spatial distribution in Sculptor and we do not find any significant difference between the different sides of the axes.

The non-axisymmetric metallicity distribution in Sextans is a potential issue that may affect our distance calculation, but with current data we cannot know how much it affects. Future data with larger sky coverage may help to resolve this.

2.5.3 Tidal disruption

One of the possible explanations of the flattening and elongation of dwarf galaxies is tidal disruption. The most famous example around the Milky Way is the Sagittarius dwarf galaxy. Sagittarius core which is undergoing strong tidal disruption shows a high ellipticity $\epsilon = 0.62 - 0.65$ (Majewski et al., 2003). For Sextans and Sculptor, the orbits of both galaxies imply that they are not likely to be affected by tides (Kaplinghat, Valli, and Yu, 2019), and Roderick et al. (2016) performs structural analysis and conclude that Sextans is not undergoing significant tidal disruption from the Milky Way, however a recent study by Vivas et al. (2019) found two RR Lyrae stars and one anomalous Cepheid that may be extratidal stars of Sextans, which suggest that this galaxy may be undergoing tidal destruction. For Sculptor, Westfall et al. (2006) states the possibility of past tidal disruption could have occurred given that there is possible presence of unbound tidal debris and Peñarrubia et al. (2009) also states the possibility of past tidal disruption considering the shape of its density distribution, but a more recent study by de Boer et al. (2011) shows that the clear radial gradients in Sculptor means lack of signs of recent tidal interactions. Our shape modeling results also prefer oblate shapes and do not show alignment of the best-fit ellipsoids towards the Galactic centre, while the numerical simulations suggest that tidally stripped subhaloes should have prolate shapes oriented towards the Galactic centre (Cooper et al., 2010; Vera-Ciro et al., 2014; Barber et al., 2015). With all this evidence, we think it is unlikely that the observed 3-D shape is caused by tidal disruption.

2.5.4 Consistency with other shape studies

Our results for Sextans and Sculptor are consistent with results from Sanders and Evans (2017), where the authors measured the intrinsic shapes and alignments of dSph galaxies of Local Group and find the dSph of the Milky Way have mean intrinsic ellipticities around 0.6. There is also a recent work by Xu and Randall (2020) shows that faint Local Group dwarf galaxies are more likely to be oblate while the bright one are more likely to be prolate based on the correlation between 2D ellipticity and central surface brightness, and the mass-to-light threshold between bright and faint is between $70 - 200 M_\odot / L_\odot$. Our result for Sextans which has mass-to-light $98 M_\odot / L_\odot$ is consistent with their conclusion, however the distance gradient of Sculptor which has mass-to-light $12 M_\odot / L_\odot$ is not consistent with prolate shape. Xu and Randall (2020) doesn't reject the possibility that the shape could be triaxial, and our result shows that Sculptor possibly have a non-zero triaxiality.

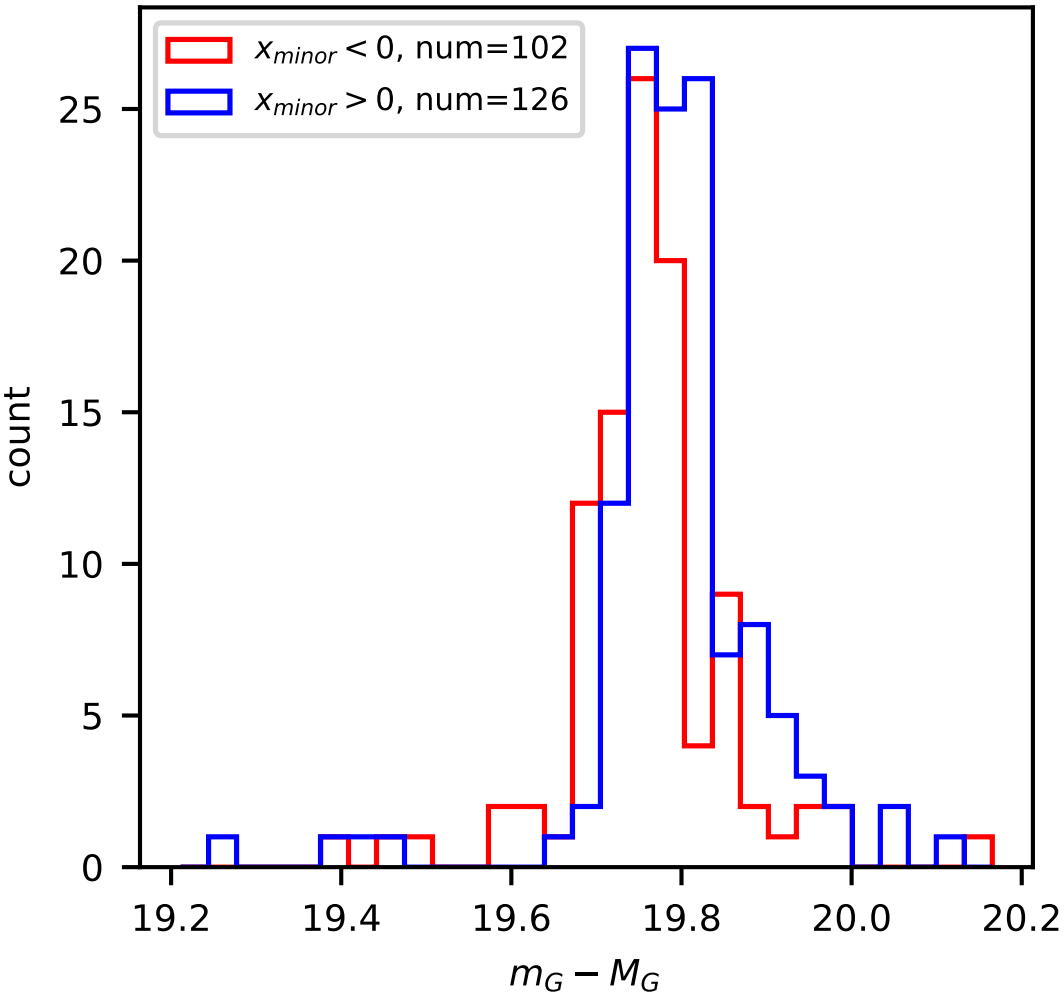

FIGURE 2.7: The plot shows the distance modulus distribution of Sextans' BHB stars for different sides separated by semi-minor axis. x_{minor} is the position along semi-minor axis, and the centre of Sextans has $x_{minor} = 0$. $x_{minor} > 0$ is northwest side and $x_{minor} < 0$ is southeast side

2.6 Conclusions

Using the data from *Gaia* DR2, DECaLS and DES, we perform the modeling of possible distance gradient in five dwarf galaxies using BHB stars. The results from Bootes I, Draco and Ursa Minor are all consistent with zero gradient within 3σ, but Sextans and Sculptor show statistically significant non-zero distance gradient. In both of these cases the distance gradient is along semi-minor axis, with the distance gradient along semi-major axis consistent with zero.

We construct 3-D ellipsoid models for Sextans and Sculptor to explain the distance gradient. The results show that an oblate shape is preferred for Sextans and intrinsic ellipticity ($1 - C/A$) larger than 0.47. For Sculptor the result of triaxial model shows possible oblate shape with intrinsic ellipticity larger than 0.46 and possibly non-zero triaxiality.

We explore the validity of the oblate models for Sextans and Sculptor by checking the relationship between galaxy rotation, anisotropy and intrinsic ellipticity, we find our results are consistent with current constraints on the velocity gradient in these systems with mild anisotropy.

One potential issue that could bias our detections is the presence of non-axisymmetric structures with different metallicities, such as have been previously seen in Sextans. We also see a different number of BHB stars at different sides of the galaxy that could be related with this, however we cannot get a reliable conclusion with current data.

We show that with our method it is possible to constrain the 3-D shape of individual dwarf galaxies. With more systems and other distance indicators such as RR Lyrae, red clump stars we can hope to obtain better constraints on the 3-D shapes of dwarf galaxies.

Chapter 3

Offset of M54 from the Sagittarius Dwarf Spheroidal Galaxy

We present results from simultaneous modeling of 2D (projected along the line of sight) position, proper motion and line-of-sight velocity for *Gaia*- and APOGEE-observed stars near the centre of the Sagittarius (Sgr) dwarf spheroidal galaxy. We use a mixture model that allows for independent sub-populations contributed by the Sgr galaxy, its nuclear star cluster M54, and the Milky Way foreground. We find an offset of 0.295 ± 0.029 degrees between the inferred centroids of Sgr and M54, corresponding to a (projected) physical separation of 0.135 ± 0.013 kpc. The detected offset might plausibly be driven by unmodelled asymmetry in Sgr's stellar configuration; however, standard criteria for model selection favour our symmetric model over an alternative that allows for bilateral asymmetry. We infer an offset between the proper motion centres of Sgr and M54 of $[\Delta\mu_\alpha \cos\delta, \Delta\mu_\delta] = [4.9, -19.7] \pm [6.8, 6.2]$ μas yr^{-1}, with magnitude similar to the covariance expected due to spatially-correlated systematic error. We infer an offset of 4.1 ± 1.2 km s^{-1} in line-of-sight velocity. Using inferred values for the systemic positions and motions of Sgr and M54 as initial conditions, we calculate the recent orbital history of a simplified Sgr/M54 system, which we demonstrate to be sensitive to any line-of-sight distance offset between M54 and Sgr, and to the distribution of dark matter within Sgr.

3.1 Introduction

Observations reveal that a significant fraction of galaxies host dense nuclear star clusters (NSCs) at their centres (Côté et al., 2006; Turner et al., 2012; Baldassare et al., 2014; Brok et al., 2014; Sánchez-Janssen et al., 2019; Neumayer, Seth, and Böker, 2020). However, the formation of NSCs is still a debated question. Possible explanations range from in situ star formation at the galactic centre (Bekki, Couch, and Shioya, 2006; Bekki, 2007; Antonini, Barausse, and Silk, 2015) to the infall of globular clusters (GCs), whose orbits decay and spiral to the centre due to dynamical friction Tremaine, Ostriker, and Spitzer (1975), Capuzzo-Dolcetta (1993), Arca-Sedda and Capuzzo-Dolcetta (2014), and Gnedin, Ostriker, and Tremaine (2014).

Some NSCs are found to host metal-poor stars (Rose, 1985; Carretta et al., 2010; Do et al., 2015), which can be naturally explained by old, metal-poor GCs bringing those stars into the nucleus. Deficits of bright non-nuclear GCs near the central regions of elliptical galaxies also seem to indicate that the central nuclei formed via the orbital decay of massive clusters (Capuzzo-Dolcetta and Mastrobuono-Battisti, 2009; Lotz et al., 2001). In early-type galaxies with stellar mass $\lesssim 10^9\,M_\odot$, the NSCs and GC systems have similar occupation distributions and comparable total masses (Sánchez-Janssen et al., 2019), consistent with NSC formation by infalling GCs.

However, many NSCs also contain young stellar populations (Seth et al., 2006; Walcher et al., 2006; Nguyen et al., 2014; Bender et al., 2005; Paumard et al., 2006), suggestive of in situ star formation within the host galaxy. Thus, it seems that both the GC infall and in situ star formation contribute to NSC formation. Indeed some NSCs display both young and old stellar populations with different morphology and kinematics, which indicates different origins for different components and multiple star formation episodes (Seth et al., 2006; Rossa et al., 2006; Walcher et al., 2006). For example, Hartmann et al. (2011) show that it is necessary to consider both stellar dynamical mergers and in situ star formation to reproduce observations of the NSCs at the centres of NGC 422 and M33. Antonini, Barausse, and Silk (2015) use a semi-analytical galaxy formation model that includes both dynamical-friction-driven migration of stellar clusters and star formation triggered by infalling gas to simulate the co-evolution of NSCs and central black holes, finding that in situ star formation contributes a significant fraction (up to $\sim 80\%$) of the total mass of NSCs.

Considering the various pathways of NSC formation, it is useful to make detailed comparisons between the spatial and chemodynamical properties of NSCs and their host galaxies. Notably, some works find evidence for offsets between the centres of some NSCs and the centres of their hosts. For example, Binggeli, Barazza, and Jerjen (2000) search for off-centre nuclei in 78 nucleated dwarf elliptical galaxies of the Virgo Cluster, finding that roughly 20% of the sample are significantly off-centre. Côté et al. (2006) study 100 early-type galaxies of the Virgo Cluster, identifying five candidates with nuclei offset from the host galaxy photocentre; they note, however, it is possible that some of these cases are due to non-nuclear globular clusters that happen to be projected close to the galaxy photocentre. Such offsets, if real, may indicate oscillations of the NSC that may help constrain, e.g., the mass of a central black hole (Taga and Iye, 1998) and/or other physical processes like counterstreaming instability (De Rijcke and Debattista, 2004).

The nearest NSC, Messier 54 (M54 also known as NGC 6715) within the Sagittarius (Sgr) dwarf spheroidal (dSph) galaxy, offers a unique opportunity to observe detailed spatial and chemodynamic properties of individual stars within a NSC and its local environment. Originally discovered in a line-of-sight velocity survey of the Galactic bulge (Ibata, Gilmore, and Irwin, 1994), Sgr lies at a distance of $\sim$ 26 kpc from the Sun, $\sim$ 18 kpc from the Galactic centre, and is the progenitor of the prominent Sagittarius stream, stellar debris from the ongoing process of Sgr's tidal disruption within the Milky Way (Ibata et al., 2001; Majewski et al., 2003; Belokurov et al., 2006). The central region of Sgr, which includes M54, displays a complex formation history, with various photometric and spectroscopic studies identifying old ($\gtrsim$ 10 Gyr), intermediate-age ($\sim 4-6$ Gyr) and young ($\lesssim$ 3 Gyr) stellar populations with a corresponding range of metallicity from -1.8$\lesssim$ [Fe/H]$\lesssim$ +0.6 (e.g. Sarajedini and Layden, 1995; Siegel et al., 2007; Siegel et al., 2011; Alfaro-Cuello et al., 2019).

This complexity extends to the observed stellar kinematics. The old, metal-poor stars have a line-of-sight velocity dispersion profile that declines steeply with cluster-centric radius (Ibata et al., 2009), then gradually rises near M54's nominal tidal radius (Bellazzini et al., 2008). Over the same region, the relatively metal-rich stars display approximately constant velocity dispersion, as is characteristic of the Milky Way's dwarf spheroidal satellite galaxies (Bellazzini et al., 2008). Even outside the nucleus, the main body of Sgr itself exhibits complex internal stellar kinematics, with a central bar-like structure that connects to 'tails' of escaping stars, a bound, rotating inner core, and apparent expansion along the long axis that characterises an overall triaxial morphology (del Pino et al., 2021).

Given this complexity, it is difficult to disentangle M54 from its Sgr host. Analysing the spatial distribution of a large photometrically-selected sample of M giant stars from

the Two Micron All Sky Survey, Majewski et al. (2003) find an overdense 'cusp' at the position of M54; however, they argue that this feature belongs to Sgr and not to M54, whose metal-poor stars are too blue to be included in the M giant sample. Analysing metal-rich and metal-poor populations selected from optical photometry, Monaco et al. (2005) conclude similarly, finding that the metal-rich stars (presumed to belong to Sgr) exhibit an overdense cusp at the same location as the cusp seen in metal-poor stars (presumed to belong to M54). However, a MUSE spectroscopic survey of M54 by Alfaro-Cuello et al. (2019) finds that the metal-rich stars can be separated into young ($\sim$ 2 Gyr) and intermediate-age ($\sim$ 4 Gyr) populations, associating the more compact, younger subpopulation with late star formation within M54, and the more extended, intermediate-age sub-population with the Sgr host.

If the old, metal-poor component of M54 is an example of a GC that fell to the centre of its host galaxy, then its properties may also help to constrain the spatial distribution of dark matter within Sgr. Various dynamical and N-body studies demonstrate that the efficiency and outcome of dynamical friction depend on the spatial distribution of dark matter within the host galaxy (e.g., Goerdt et al., 2006; Read et al., 2006; Goerdt et al., 2010; Meadows et al., 2020). If the host dark matter halo has the central 'cusp' that characterises cold dark matter halos (Navarro, Frenk, and White, 1997, 'NFW' hereafter), dynamical friction operates efficiently to drag a massive GC to the centre in a fraction of a Hubble time; if instead the host halo has a central 'core' of uniform density, the infalling cluster tends to stall near the core radius, where the halo becomes effectively 'bouyant' (Cole et al., 2012; Banik and van den Bosch, 2022). Using N-body models to simulate specifically the infall of M54 within Sgr, Bellazzini et al. (2008) find that for a variety of initial conditions, if the Sgr host has an NFW-like cusp, then M54 sinks efficiently (in $\lesssim$ 3 Gyr) to the very centre of Sgr, where it remains virtually at rest, with a systemic velocity offset of $\lesssim 1-2$ km s^{-1}. These results are broadly consistent with those of Herlan, Mastrobuono-Battisti, and Neumayer (2023), who also find that a more (than NFW) steeply cusped dark matter halo in Sgr would result in a NSC that (internally) rotates faster and is morphologically flatter than M54.

Thus the observed properties of the Sgr/M54 system impact our understanding not only of NSC formation, but also the nature of dark matter. In any case, the degree to which M54 and the centre of Sgr are either distinct or coincident in phase space remains an interesting open question. The answer is complicated for several reasons. First, as mentioned above, the central regions of Sgr display a mixture of several stellar populations with different ages, metallicities, structural parameters and kinematics, and the assignment of a given population to one or the other object can be ambiguous. Second, published measurements of centroids, distances and systemic velocities often pertain to just one of Sgr or M54. For example, the infrared M-giant sample of Majewski et al. (2003) is relatively insensitive to the metal-poor population in M54; conversely, Hubble Space Telescope and the MUSE observations of M54 typically lack the sky coverage to map Sgr over a significant fraction of its core region (e.g., Siegel et al., 2011; Alfaro-Cuello et al., 2019). As a result, comparisons of published measurements for Sgr and M54 must contend with systematic errors (e.g., zero-point offsets) introduced by the use of different data sets.

A notable exception is the recent study by del Pino et al. (2021), which uses the Gaia (DR2) catalogue, supplemented with training data from spectroscopic (line-of-sight velocity) catalogues, to construct a catalog of 6D phase-space coordinates for a final sample of $\sim 1.2 \times 10^5$ stars within $\sim 6^\circ$ of the Sgr centre. With this catalogue, they iteratively measure the centre-of-mass coordinates of a Sgr sample that excludes all stars within the fiducial tidal radius of M54, and separately the center-of-mass coordinates for the M54

sample that includes only the stars excluded from the Sgr sample. They find a statistically significant offset only among the plane-of-sky centroids, which they discount as likely driven by systematic error due to incompleteness that results from the Gaia scan pattern that is apparent in their sample (their Figure 4).

Here we take an approach that is complementary to that of del Pino et al. (2021). Rather than adopting hard cuts in colour/magnitude or sky position to separate M54 and Sgr samples, we use the mixture models to analyse the 5D distribution of sky position, proper motion and line-of-sight velocity, the phase-space coordinates for which homogeneous measurements from Gaia EDR3 (Gaia Collaboration et al., 2021) and/or the Apache Point Observatory Galactic Evolution Experiment (APOGEE; Majewski et al., 2017) are available for large numbers of stars in the Sgr. The mixture modelling lets us obtain simultaneous estimates for the 5D centres of the Sgr and M54 populations, providing a direct inference about any offset in these dimensions of phase space. Any detected offset can then be used to inform subsequent models for the formation and evolution of M54 as the NSC within Sgr. Furthermore, since our mixture models do not operate separately on pre-selected M54 and Sgr samples, the result can be used to infer, rather than assume, the colour/magnitude distributions traced separately by the two objects.

We describe the data selection procedure in Section 3.2. In Section 3.3, we describe the construction of the mixture model. In Section 3.4, we present results from our modelling. In Section 3.5, we compare our results to previous work and discuss the robustness of our results, the colour/magnitude distribution of the M54, and the recent orbital history of the Sgr/M54 system. In Section 3.6, we summarise our conclusions.

3.2 Data

This work is based on data presented in the Early Data Release 3 (EDR3, Gaia Collaboration et al., 2021) of the Gaia mission (Gaia Collaboration et al., 2016b), and on line-of-sight velocity data presented by APOGEE Data Release 17 (DR17; Abdurro'uf et al., 2022). *Gaia* EDR3 consists of astrometry and photometry for 1.8 billion sources brighter than magnitude $G \approx 21$. Compared with *Gaia* DR2, *Gaia* EDR3 improves the parallax precision by 30% and increases proper motion precision by a factor of 2. At magnitude $G = 17$, it provides typical uncertainties of 0.07 mas yr^{-1} in proper motion, 0.07 mas in parallax angle, 0.05 mas in position, 1 mmag in G-band magnitude, 12 mmag in G_{BP} magnitude, and 6 mmag in G_{RP} magnitude (Gaia Collaboration et al., 2021). APOGEE DR17 is the continuation of the Apache Point Observatory Galactic Evolution Experiment (APOGEE, Majewski et al., 2017) and Data Release 17 of APOGEE-2/SDSS-IV (Majewski, APOGEE Team, and APOGEE-2 Team, 2016). APOGEE spectroscopic catalogues include stellar-atmospheric parameters and line-of-sight velocities measured from twin, multi-plexed, near-infrared, high-resolution spectra covering both the northern and southern sky (Abdurro'uf et al., 2022; Wilson et al., 2019). The extracted line-of-sight velocities have a median reported uncertainty of 0.015 km s^{-1}.

3.2.1 *Gaia* EDR3 Data Selection

We begin by considering all sources from Gaia EDR3 that lie within 4° of a fiducial center of M54 ($\alpha_{2000} = 283.76353°, \delta_{2000} = -30.477006°$; Alfaro-Cuello et al., 2019). Within this region, one immediately obvious systematic effect is the tendency for sources near the centre of M54 to have relatively poor astrometric solutions due to crowding. Figure 3.1 demonstrates that application of the standard filter for selecting astrometrically well-behaved sources, `astrometric_excess_noise_sig` < 2 (Lindegren et al., 2012) removes

almost all sources within $\sim$ 1 arcmin, or $\sim$ 2 half-mass radii of M54 ($r_h = 0.43 \pm 0.08$ arcmin; Alfaro-Cuello et al. 2019). To avoid this selection bias, we mask the entire region within $\sim 0.03^\circ$ (1.8 arcmin) of the fiducial centre of M54. We note that special Service-Interface Function (SIF) images of dense area, which includes the centre of the Sgr dSph, are acquired in the sky-mapper CCDs (Gaia Collaboration et al., 2016b), and that can be used to analyse the centre of the Sgr dSph. One example is the data for ω Centauri in Gaia Collaboration et al. (2023b). However, these special SIF data are not part of Gaia DR3.

Next, following Vitali et al. (2022), we impose a magnitude cut at $G < 17.3$ in order to ensure high-quality astrometry and homogeneous coverage over the region of interest. Then we cut on proper motion based on a data-driven filter as shown in Fig 3.2. We make additional cuts on parallax to remove stars with distance less than 20 kpc and apply data quality flags. Our complete initial selection uses the following criteria:

$0.03^\circ \leq \sqrt{x^2 + y^2} \leq 4^\circ$
$\texttt{phot\_g\_mean\_mag} < 17.3$,
$\texttt{astrometric\_excess\_noise\_sig} < 2$,
$\texttt{parallax} < 0.05 + 3 \times \texttt{parallax\_error}$,
$\texttt{pmra} \in [-3.12, -2.22]$, $\texttt{pmdec} \in [-1.91, -0.91]$
$\texttt{ipd\_frac\_multi\_peak} < 2$
$\texttt{ruwe} < 1.3$
$\texttt{duplicated\_source} = \texttt{False}$
$|C^\star| < 3\varpi_{C^\star}$.

Here, (x, y) are rectilinear coordinates obtained via gnomonic projection of the Gaia-measured sky coordinates, assuming an origin at the previously-published center of M54 ($\alpha_{2000} = 283.76353^\circ, \delta_{2000} = -30.477006^\circ$; Alfaro-Cuello et al., 2019). $C^\star$ is the corrected BP and RP flux excess factor, defined in Equation (6) of Riello et al., 2021 and $\varpi_{C^\star}$ is the 1σ scatter, calculated according to Equation (18) of Riello et al. (2021). Using the 'astrometric fidelity' parameter of (Rybizki et al., 2022), all of the sources in our final sample have $\texttt{fidelity} > 0.5$ (Rybizki et al., 2022), indicating good data quality. The *Gaia* EDR3 photometry is corrected for extinction using the code from Appendix A of Gaia Collaboration et al. (2021). The extinction is calculated using Equation 1 and Table 1 from Gaia Collaboration et al. (2018c).

3.2.2 APOGEE DR17 Data Selection

From APOGEE DR17 we select stars within a 4-degree circle centred at $(\alpha, \delta) = (283.76353, -30.477006)$. We remove stars for which any of the following conditions are met : STAR_BAD (bit position 23 in ASPCAPFLAG) is set to 1, STARFLAG is nonzero, or DUPLICATE (bit position 4 in EXTRATARG) is set to 1. The APOGEE DR17 catalogue is cross-matched with *Gaia* EDR3, allowing us to apply to the APOGEE sample the same proper motion selection that we adopt for the *Gaia* EDR3 sample (Sec 3.2.1). Our selections reduce the number of stars in our APOGEE DR17 sample from 6890 to 683. Fig. 3.3 shows the spatial distribution of stars in the selected APOGEE sample. Since APOGEE DR17 has only partial coverage in this sky area, we cannot directly combine the APOGEE and *Gaia* samples. Therefore, below, we choose to analyse the line-of-sight velocity data separately from the sky position and proper motion data. (Sec 3.3.3).

3.2.3 CMD mask

The samples selected according to the above criteria will have contamination from Milky Way stars that belong to neither M54 nor Sgr. In order to minimise this contamination,

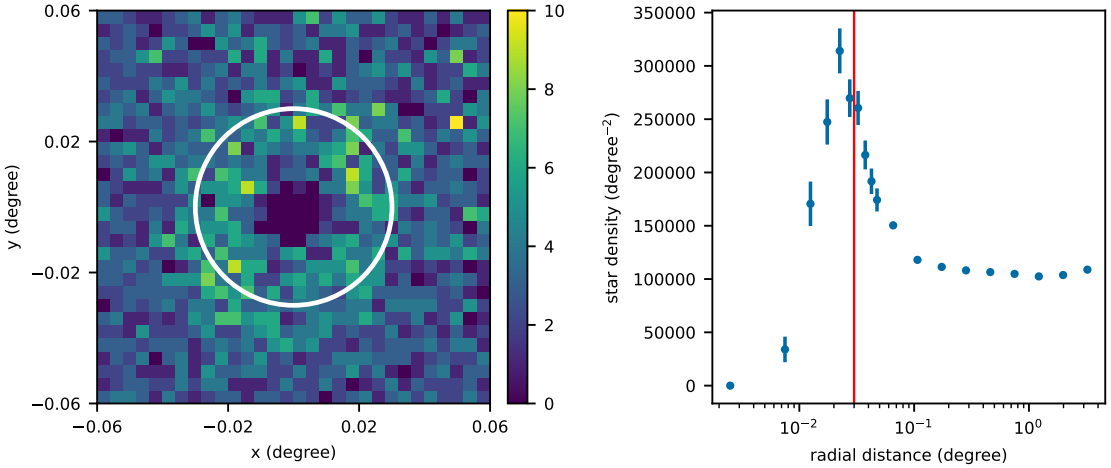

FIGURE 3.1: Projected density of stars around the centre of M54, from *Gaia* EDR3, with filters `phot_g_mean_mag` $<$ 20, `astrometric_excess_noise_sig` $<$ 2 and `phot_bp_mean_mag` and `phot_rp_mean_mag` exist. The left panel shows the 2D density field and the color is coded by the number of the stars in the bin; the right panel shows the mean density within circular annuli. The white circle and the red line denote a radius of 0.03°, inside which we mask the sample.

we construct an additional mask in the colour/magnitude diagram (CMD), combining a mask derived from the data and a mask derived from isochrone templates.

To construct the CMD mask from the data, we consider two annuli that are centred on M54, the first with inner and outer radii of $0.03, 0.2^\circ$, respectively, and the second with radii of $2.0, 4.0^\circ$. Then, from the selected sources within each annulus, we calculate 2-D histograms in colour-magnitude space, with 40 uniform bins from -0.2 to 2 in the $BP - RP$ colour dimension and 40 uniform bins from 13 to 19 in the G magnitude dimension (only for the purpose of constructing the CMD masks, we relax the magnitude limit of $G < 17.3$ that we apply when analysing the samples). Both 2-D histograms are divided by the annulus area, so that the result indicates the density of stars. We then subtract the histogram corresponding to the outer annulus from the histogram corresponding to the inner annulus. Since the outer annulus should contain a larger fraction of Milky Way contaminants, we expect this difference to be more positive in colour/magnitude bins that are less contaminated by the Milky Way. We mask sources within colour/magnitude bins for which the difference histogram has value $<$ 20 stars per degree^2. In order to decrease the effect of noise, we perform a 'closing' operation, using a 2×2 matrix of ones as the structuring element on the CMD mask.

To construct the CMD mask from isochrone templates, we consider three sets of theoretical isochrones that are motivated by the age/metallicity relations derived from MUSE spectroscopy of M54 by Alfaro-Cuello et al. (2019): young metal-rich, with [Fe/H]$=-0.04$ and age between $1.4 - 2.8$ Gyr, 2) intermediate-age metal-rich, with [Fe/H]$=-0.29$ and age between $1 - 7.8$ Gyr, and old metal-poor, with [Fe/H]=-1.41 and age between $9.4 - 15$ Gyr. For each set, we obtain the corresponding isochrones in Gaia passbands from the Dartmouth Stellar Evolution Database (DSED) (Dotter et al., 2008). We sample the age ranges with a step size of 0.2 Gyr. Shifting each isochrone for a fiducial distance modulus of 17.27 (Siegel et al., 2007), we then mask all CMD bins (using the same binning scheme adopted above for the data-derived mask) that do not contain any of the sampled isochrones.

Finally, we combine data-derived and isochrone-derived masks by masking only those

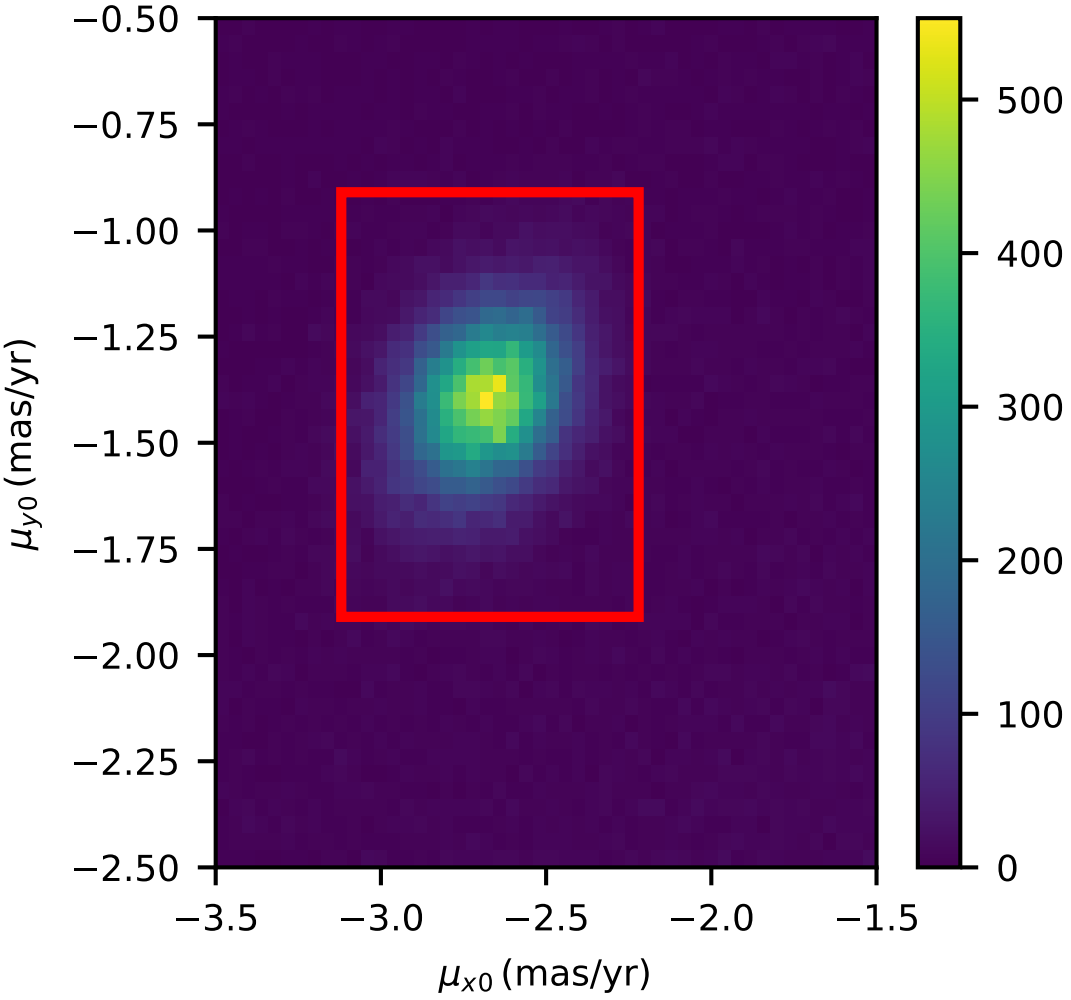

FIGURE 3.2: Distribution of proper motions of stars within 4° of the nominal center of M54, from *Gaia* EDR3, with all filters (except the proper motion filter) listed in Sec 3.2.1 applied. Color is coded by the number of stars within each pixel. The red rectangle indicates our proper motion filter.

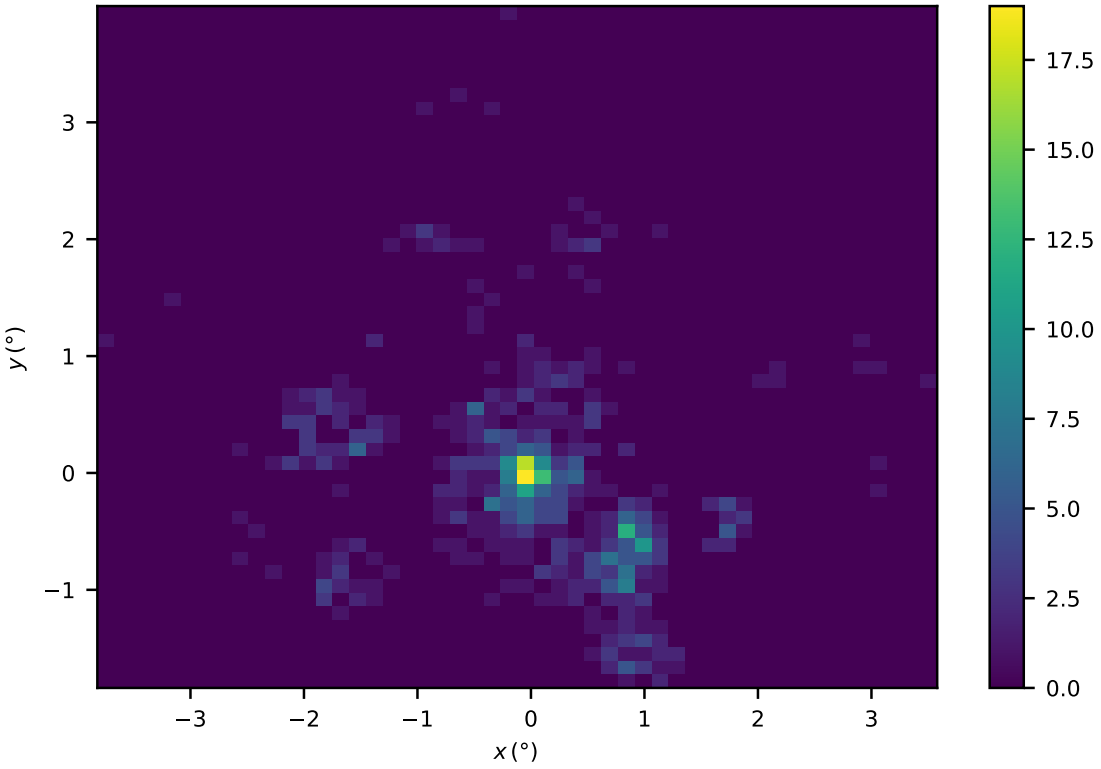

FIGURE 3.3: Spatial distribution of sources selected from APOGEE (DR17; Abdurro'uf et al., 2022). Pixels are color-coded by the number of the stars within that pixel.

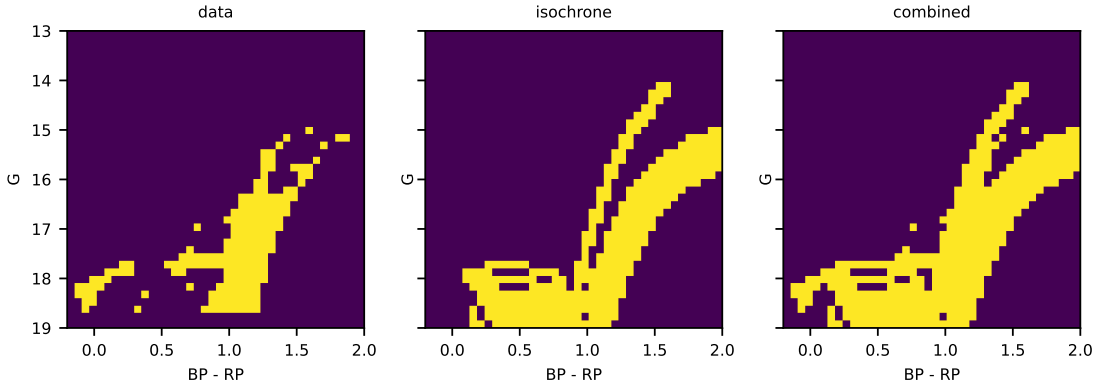

FIGURE 3.4: CMD mask for data selection, with yellow/blue indicating unmasked/masked. The left panel is the empirical CMD mask derived directly from the data; the centre panel is the CMD mask derived from theoretical isochrones; the right panel is the combined CMD mask used in our analysis.

bins that are masked in both schemes. Fig 3.4 shows the data-derived, isochrone-derived and combined CMD masks. Application of the combined mask reduces the number of stars in our selected *Gaia* EDR3 sample from 44337 to 34265.

3.3 Mixture Model for the Sgr/M54 system

We assume the sample of unmasked stars includes contributions from Sgr, M54 and the Milky Way. First we construct and fit a mixture model for the joint 4D distribution of *Gaia*-observed positions and proper motions.

3.3.1 Projected position

For M54 and Sgr, we assume that the 2D positions,

$$\boldsymbol{s} = \begin{pmatrix} x \\ y \end{pmatrix}, \tag{3.1}$$

of stars are drawn independently from analytic surface density profiles that allow for elliptical symmetry about centers specified by

$$\boldsymbol{s_0} = \begin{pmatrix} x_0 \\ y_0 \end{pmatrix}. \tag{3.2}$$

For ellipticity $\epsilon \equiv 1 - b/a$ specified by semi-major and semi-minor axes a and b, and with semi-major axis pointing along position angle θ_0 (increasing northward of the zero-point at due East), a star's 'elliptical radius', R_e, relative to the center satisfies

$$R_e^2 = \boldsymbol{R}^\top \boldsymbol{R} = (\boldsymbol{s} - \boldsymbol{s_0})^\top \boldsymbol{R}_\theta^\top \begin{pmatrix} 1 & 0 \\ 0 & \frac{1}{(1-\epsilon)^2} \end{pmatrix} \boldsymbol{R}_\theta (\boldsymbol{s} - \boldsymbol{s_0}), \tag{3.3}$$

where

$$\boldsymbol{R}_\theta = \begin{pmatrix} \cos(\theta) & \sin(\theta) \\ -\sin(\theta) & \cos(\theta) \end{pmatrix} \tag{3.4}$$

is the rotation matrix.

We assume that within the observed region, the 2D spatial distribution of stars belonging to M54 is drawn from the probability distribution specified by King (1962),

$$f_{s,\mathrm{King}}(\boldsymbol{s} \mid \Theta_{\mathrm{King}}) = k_{\mathrm{King}} \left(\frac{1}{\sqrt{1+(R_e/r_c)^2}} - \frac{1}{\sqrt{1+(r_t/r_c)^2}} \right)^2, \tag{3.5}$$

with $\Theta_{\mathrm{King}} \equiv \{x_0, y_0, r_c, r_t, \epsilon, \theta\}$ the vector of free parameters that specify the centroid, 'core' and 'tidal' radii, ellipticity and position angle, respectively. The normalisation constant k_{King} guarantees that $\int_{\mathrm{field}} f_s(x,y)\,dx\,dy = 1$, where the integration integrates only over the sampled field.

We assume that the 2D spatial distribution of stars belonging to Sgr is drawn from the probability distribution specified by Plummer (1911)

$$f_{s,\mathrm{Plummer}}(\boldsymbol{s} \mid \boldsymbol{\Theta}_{\mathrm{Plummer}}) = \frac{k_{\mathrm{Plummer}}}{(1+R_e^2/r_p^2)^2}, \tag{3.6}$$

with $\Theta_{\mathrm{Plummer}} \equiv \{x_0, y_0, r_p, \epsilon, \theta\}$ the vector of free parameters that specify the centroid, Plummer scale radius, ellipticity and position angle, respectively, and k_{Plummer} the normalisation constant.

We assume the Milky Way contaminants are drawn from a probability distribution specified by a first order polynomial function,

$$f_{s,n}(\boldsymbol{s} \mid \Theta_L) = k_L\,|1 + b_0 x + b_1 y| \tag{3.7}$$

with $\Theta_L \equiv (b_0, b_1)$ the vector of free parameters that specify the polynomial coefficients, and k_L the normalisation constant.

3.3.2 Proper motion

For each of the M54, Sgr and Milky Way components, we assume that the proper motions,

$$\boldsymbol{\mu} = \begin{pmatrix} \mu_x \\ \mu_y \end{pmatrix}, \tag{3.8}$$

are drawn independently from bivariate normal probability distributions with centers

$$\boldsymbol{\mu_0}(x, y \mid \boldsymbol{A}) = \begin{pmatrix} \mu_{0_x} \\ \mu_{0_y} \end{pmatrix} + \boldsymbol{A} \begin{pmatrix} x \\ y \end{pmatrix}, \tag{3.9}$$

where

$$\boldsymbol{A} = \begin{pmatrix} a_1 & a_2 \\ a_3 & a_4 \end{pmatrix} \tag{3.10}$$

specifies dependence on projected sky position, and covariance matrix

$$\boldsymbol{\Sigma} = \boldsymbol{R}_\psi^\top \boldsymbol{S} \boldsymbol{R}_\psi, \tag{3.11}$$

where

$$\boldsymbol{S} \equiv \begin{pmatrix} d_0^2 & 0 \\ 0 & d_1^2 \end{pmatrix} \tag{3.12}$$

and

$$\boldsymbol{R}_\psi \equiv \begin{pmatrix} \cos(\psi) & -\sin(\psi) \\ \sin(\psi) & \cos(\psi) \end{pmatrix}, \tag{3.13}$$

with ψ corresponding to the position angle of the long axis of the proper motion ellipsoid (increasing from the positive direction of proper motion in right ascension direction toward the negative direction of proper motion in declination direction).

For a given component, then, the observed proper motion has probability density

$$f_\mu(\boldsymbol{\mu} \mid \Theta_\mu) = \frac{\mathcal{N}(\boldsymbol{\mu} \mid \boldsymbol{\mu_0}, \boldsymbol{\Sigma} + \boldsymbol{\Sigma_0})}{C}, \tag{3.14}$$

where $\boldsymbol{\Theta_\mu} \equiv \{\mu_{0_x}, \mu_{0_y}, a_1, a_2, a_3, a_4, d_0, d_1, \psi\}$ specifies free parameters and $\boldsymbol{\Sigma_0}$ is the covariance matrix of the observed proper motion coordinates (adopted from the Gaia EDR3 catalog), and

$$C \equiv \int_{\mu_{x_1}}^{\mu_{x_2}} \int_{\mu_{y_1}}^{\mu_{y_2}} \mathcal{N}(\boldsymbol{\mu} \mid \boldsymbol{\mu_0}, \boldsymbol{\Sigma} + \boldsymbol{\Sigma_0})\, d\mu_x\, d\mu_y \tag{3.15}$$

is a normalizing factor that accounts for the finite proper motion selection window (Section 3.2.1), chosen to ensure $\int\int f_\mu(\boldsymbol{\mu} \mid \boldsymbol{\Theta}_\mu)\, d\boldsymbol{\mu} = 1$.

3.3.3 Line-of-sight Velocity

We assume that the line-of-sight velocities, v, sampled by APOGEE are drawn independently from a mixture that includes contributions from Sgr, M54 and the Milky Way, all of which are assumed to have velocities that follow univariate normal probability distributions. That is, for each of the three components we assume the APOGEE-observed velocities are drawn from

$$f_v(v \mid \boldsymbol{\Theta}_v) = \mathcal{N}(v \mid v_0 + e_x x + e_y y, \sigma^2 + \delta_v^2), \tag{3.16}$$

where the free parameters in $\boldsymbol{\Theta}_v$ specify a mean velocity, $v_0 + e_x x + e_y y$, that can vary linearly with sky position and has central value v_0, and intrinsic velocity dispersion σ. δ_v is the observational error associated with the velocity measurement (adopted from the APOGEE catalogue). In practice, we assume $e_x = e_y = 0$ for the M54 and MW components, allowing for a non-zero line-of-sight velocity gradient only in Sgr.

3.3.4 Likelihood Functions

With the normalized probability distributions specified for observed position and proper motion coordinates, the 4D observation of position and proper motion coordinates has joint probability density

$$f_{\boldsymbol{s},\boldsymbol{\mu}}(\boldsymbol{s}, \boldsymbol{\mu} \mid \Theta) = \sum_{i=1}^{N_{\text{comp}}} \phi_i\, f_s(\boldsymbol{s} \mid \boldsymbol{\Theta}_{\boldsymbol{s}_i}) f_\mu(\boldsymbol{\mu} \mid \boldsymbol{\Theta}_{\boldsymbol{\mu}_i}), \tag{3.17}$$

where $\boldsymbol{\Theta}$ specifies all free parameters and the sum is over the N_{comp} different mixture components, each of which has contribution weighted by ϕ_i, the fraction of the sample that is contributed by the i^{th} component. For each of the $N_{\text{comp}} = 3$ components, we specify ϕ_i in terms of parameters p_i, with the latter defined according to

$$\phi_i = \begin{cases} p_i \left(1 - \sum_{j=1}^{i-1} \phi_j\right) = p_i \prod_{j=1}^{i-1} (1 - p_j) & i < N_{\text{comp}} \\ 1 - \sum_{j=1}^{i-1} \phi_j = \prod_{j=1}^{i-1} (1 - p_j) & i = N_{\text{comp}} \end{cases} \tag{3.18}$$

As described in Section 3.3.1, for different components we adopt different analytic functions for the probability density of stellar positions. For M54 we use $f_{\boldsymbol{s}}(\boldsymbol{s} \mid \boldsymbol{\Theta}_{\boldsymbol{s}}) = f_{\boldsymbol{s},\text{King}}(\boldsymbol{s} \mid \boldsymbol{\Theta}_{\text{King}})$; for Sgr we use $f_{\boldsymbol{s}}(\boldsymbol{s} \mid \boldsymbol{\Theta}_{\boldsymbol{s}}) = f_{\boldsymbol{s},\text{Plummer}}(\boldsymbol{s} \mid \boldsymbol{\Theta}_{\text{Plummer}})$; for the Milky Way we use $f_{\boldsymbol{s}}(\boldsymbol{s} \mid \boldsymbol{\Theta}_{\boldsymbol{s}}) = f_{\boldsymbol{s},\boldsymbol{n}}(\boldsymbol{s} \mid \boldsymbol{\Theta}_{\boldsymbol{L}})$.

For all three components, we assume that the observed proper motions follow the general form of $f_{\boldsymbol{\mu}}(\boldsymbol{\mu} \mid \boldsymbol{\Theta}_{\boldsymbol{\mu}})$ given by Equation 3.14. For both M54 and the Milky Way, we assume that the proper motion centre, $\boldsymbol{\mu_0}$, is independent of the spatial position within the sampled region, with $a_1 = a_2 = a_3 = a_4 = 0$. For Sgr, following Vasiliev and Belokurov (2020), we allow for a linear dependence of the mean proper motion on projected sky position, letting the components of $\boldsymbol{A}$ be nonzero.

Assuming the observations of different sources are uncorrelated, the 4D Gaia sample of $N = 34265$ stars has likelihood

$$\mathcal{L}_4 = \prod_{k=1}^{N} f(\boldsymbol{s}_k, \boldsymbol{\mu}_k \mid \boldsymbol{\Theta}) \tag{3.19}$$

Similarly, the 1D Apogee sample of $N_v = 683$ stars has likelihood

$$\mathcal{L}_1 = \prod_{k=1}^{N_v} \sum_{i=1}^{N_{\text{comp}}} q_{k,i} f_v(v_k \mid \boldsymbol{\Theta}_{v,\text{i}}), \tag{3.20}$$

where the weight

$$q_{k,i} = \frac{c_i f_{\boldsymbol{s},\boldsymbol{\mu}}(\boldsymbol{s}_k, \boldsymbol{\mu}_k \mid \boldsymbol{\Theta}_i)}{\sum_{j=1}^{N_{\text{comp}}} c_j f_{\boldsymbol{s},\boldsymbol{\mu}}(\boldsymbol{s}_k, \boldsymbol{\mu}_k \mid \boldsymbol{\Theta}_j)} \tag{3.21}$$

is the probability of the k^{th} star's membership in the i^{th} component, given the *Gaia*-observed position and proper motion parameters $\boldsymbol{\Theta}_i$ of the 4D model for the i^{th} component. The three parameters c_1, c_2 and c_3 represent the mixing fractions within the spectroscopic sample. We use the analogue of Equation 3.18 to specify the c_i in terms of two independent free parameters m_1, m_2, requiring that $\sum_{i=1}^{N_{\text{comp}}} c_i = 1$.

3.3.5 Inference

From the 4D and 1D data sets, denoted D_4 and D_1, respectively, we are interested in inferring posterior probability distributions

$$f_4(\boldsymbol{\Theta} \mid D_4) = \frac{\mathcal{L}_4 \, \pi(\boldsymbol{\Theta})}{\int \mathcal{L}_4 \, \pi(\boldsymbol{\Theta}) \, d\boldsymbol{\Theta}} \tag{3.22}$$

and

$$f_1(\boldsymbol{\Theta}_v \mid D_1) = \frac{\mathcal{L}_1 \, \pi(\boldsymbol{\Theta}_v)}{\int \mathcal{L}_1 \, \pi(\boldsymbol{\Theta}_v) \, d\boldsymbol{\Theta}_v}, \tag{3.23}$$

where $\pi(\boldsymbol{\Theta})$ and $\pi(\boldsymbol{\Theta}_v)$ are priors and the denominator on the right-hand side of each equation is the marginalized likelihood, or 'evidence'. In order to estimate $f_1(\boldsymbol{\Theta}_v \mid D_1)$, when evaluating the component membership probabilities in Equation 3.20 we hold 4D

TABLE 3.1: Free parameters of the model fit to 4D Gaia sample of projected position and proper motion, including priors, quantiles at $(0.1587, 0.5, 0.8413)$ and maximum a posteriori (MAP).

	Prior	Params	$(0.1587, 0.5, 0.8413)$ Quantile	MAP
Member Fraction	Dirichlet$(1,1,1)$[1]	p_1	$(0.01555, 0.01696, 0.01837)$	0.0179
		p_2	$(0.970, 0.972, 0.974)$	0.9724
M54 Spatial ($\mathbf{\Theta}_{s,\mathrm{M54}}$)	$\mathrm{U}[-0.03, 0.03]$	x_0 (°)	$(-0.003968, -0.001318, 0.001358)$	0
	$\mathrm{U}[-0.03, 0.03]$	y_0 (°)	$(-0.004626, -0.001924, 0.0007959)$	−0.0030
	$\mathcal{N}(0.0015, 0.0015^2)$	r_c (°)	$(0.0007815, 0.001938, 0.003343)$	0.0017
	$\mathrm{U}[0.03, 10.0]$	r_t (°)	$(6.483, 8.274, 9.499)$	9.7
	$\mathrm{U}[-0.5\pi, 0.5\pi]$	θ (rad)	$(-0.8814, -0.1925, 0.686)$	−0.24
	$\mathrm{U}[0.1, 1.0]$	$1-\epsilon$	$(0.8612, 0.9326, 0.9803)$	0.88
M54 proper motion ($\mathbf{\Theta}_{\mu,\mathrm{M54}}$)	$\mathrm{U}[-4.32, -1.32]$	μ_{0_x} (mas yr^{-1})	$(-2.689, -2.682, -2.676)$	−2.6779
	$\mathrm{U}[-3.01, -0.02]$	μ_{0_y} (mas yr^{-1})	$(-1.386, -1.380, -1.374)$	−1.3769
	$\mathrm{U}[0.0, 2.0]$	s_0 (mas yr^{-1})	$(0.04562, 0.05254, 0.05951)$	0.0542
	$\mathrm{U}[0.0, 2.0]$	s_1 (mas yr^{-1})	$(0.03546, 0.04439, 0.05283)$	0.0411
	$\mathrm{U}[0.0, 0.5\pi]$	ψ (rad)	$(0.3421, 0.8044, 1.263)$	0.87
MW Spatial ($\mathbf{\Theta}_{s,\mathrm{MW}}$)	$\mathrm{U}[-0.3, 0.3]$	b_0 (deg^{-1})	$(-0.1619, -0.1318, -0.1018)$	−0.128
	$\mathrm{U}[-0.3, 0.3]$	b_1 (deg^{-1})	$(0.05190, 0.08108, 0.1100)$	0.101
MW proper motion ($\mathbf{\Theta}_{\mu,\mathrm{MW}}$)	$\mathrm{U}[-9.0, 5.0]$	μ_{0_x} (mas yr^{-1})	$(-7.276, -3.646, 1.393)$	−2.1
	$\mathrm{U}[-20.0, 0.0]$	μ_{0_y} (mas yr^{-1})	$(-16.78, -12.34, -7.502)$	−9.6
	$\mathrm{U}[1.0, 17.0]$	s_0 (mas yr^{-1})	$(3.841, 7.398, 13.59)$	15.0
	$\mathrm{U}[1.0, 17.0]$	s_1 (mas yr^{-1})	$(2.609, 3.745, 5.937)$	2.7
	$\mathrm{U}[0.0, 0.5\pi]$	ψ (rad)	$(0.1999, 0.515, 1.189)$	0.41
Sgr Spatial ($\mathbf{\Theta}_{s,\mathrm{Sgr}}$)	$\mathrm{U}[1.0, 20.0]$	r_h (°)	$(5.013, 5.093, 5.174)$	5.083
	$\mathrm{U}[-3.0, 3.0]$	x_0 (°)	$(0.2580, 0.2856, 0.3136)$	0.252
	$\mathrm{U}[-3.0, 3.0]$	y_0 (°)	$(-0.08488, -0.0733, -0.06153)$	−0.063
	$\mathrm{U}[-0.5\pi, 0.5\pi]$	θ (rad)	$(-0.2785, -0.2725, -0.2665)$	−0.2704
	$\mathrm{U}[0.1, 1.0]$	$1-\epsilon$	$(0.3928, 0.3987, 0.4046)$	0.4008
Sgr proper motion ($\mathbf{\Theta}_{\mu,\mathrm{Sgr}}$)	$\mathrm{U}[-1.0, 1.0]$	a_1 (mas yr^{-1} deg^{-1})	$(0.007206, 0.007693, 0.008193)$	0.00782
	$\mathrm{U}[-1.0, 1.0]$	a_2 (mas yr^{-1} deg^{-1})	$(0.004597, 0.005317, 0.006028)$	0.00515
	$\mathrm{U}[-1.0, 1.0]$	a_3 (mas yr^{-1} deg^{-1})	$(-0.02349, -0.02305, -0.02262)$	−0.02305
	$\mathrm{U}[-1.0, 1.0]$	a_4 (mas yr^{-1} deg^{-1})	$(-0.01427, -0.01364, -0.01299)$	−0.01315
	$\mathrm{U}[-4.32, -1.32]$	μ_{0_x} (mas yr^{-1})	$(-2.680, -2.679, -2.678)$	−2.67913
	$\mathrm{U}[-3.01, -0.02]$	μ_{0_y} (mas yr^{-1})	$(-1.395, -1.394, -1.393)$	−1.39374
	$\mathrm{U}[0.0, 2.0]$	s_0 (mas yr^{-1})	$(0.1037, 0.1044, 0.1051)$	0.10433
	$\mathrm{U}[0.0, 2.0]$	s_1 (mas yr^{-1})	$(0.1483, 0.1492, 0.1502)$	0.14856
	$\mathrm{U}[0.0, 0.5\pi]$	ψ (rad)	$(0.9237, 0.9351, 0.9466)$	0.938

model parameters $\mathbf{\Theta}$ fixed at the maximum a posteriori (MAP) value obtained when estimating $f_4(\mathbf{\Theta} \mid D_4)$. Table 3.1 lists the priors that we adopt for all model parameters. For all parameters except M54's core radius and those that specify member fractions, we adopt uniform priors over finite ranges. For the core radius of M54, since our sample excludes the core region (Figure 3.1), we adopt a truncated Gaussian prior that is centred on the previous measurement by Harris (1996) (2010 edition) which is 0.0015°. The reported measurement does not include uncertainty, so we use 0.0015° as the standard deviation of the Gaussian prior to allow a broad distribution. We also set a lower bound $r_c > 1 \times 10^{-4}$ degree to ensure numerical stability of the calculation of the normalisation factor in the King profile. For the parameters p_i (and m_i) that specify member fractions in the 4D (1D) model according to Equation 3.18, we adopt a Dirichlet prior over $(\phi_1, \ldots, \phi_{N_{\mathrm{comp}}})$ and $(c_1, \ldots, c_{N_{\mathrm{comp}}})$ which can be interpreted as the uniform distribution under the constraints $\sum_i \phi_i = 1, \phi_i > 0$ and $c_i = 1, c_i > 0$.

Independently for each data set, we obtain random samples from the posteriors using the software package emcee (Foreman-Mackey et al., 2013), which implements a Markov chain Monte Carlo (MCMC) method. When fitting the 4D sample, we use 3000 walkers, 5000 steps and thinning parameter of 2. When fitting the 1D sample, we use 500 walkers, 5000 steps and thinning parameter of 1. In both cases, we discard the first half of the chain as burn-in.

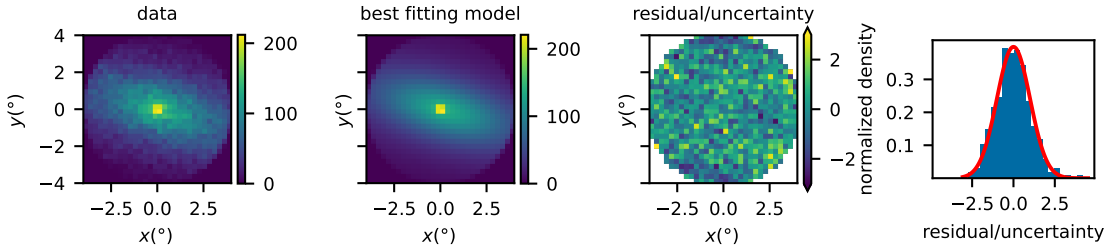

FIGURE 3.5: Projected density of stars in the selected sample (left), best-fitting model (middle left), residuals normalised by Poisson uncertainties (middle right), and normalized distribution of the residuals/uncertainty. The colour bars indicate the number of stars in each bin (left, middle left) and residual/uncertainty in the corresponding bin (middle right right). The red curve in the right plot is the normal distribution centred at 0 with variance 1.

3.4 Results

Random samples sampled from posterior distributions are publicly available at `https://doi.org/10.5281/zenodo.10659516`. Table 3.1 and Table 3.2 summarise the marginalised 1D posterior for each model parameter in the 4D and 1D mixture models, respectively, identifying the quantile at $(0.1587, 0.5, 0.8413)$ for each parameter. The member fraction (ϕ_i) for each component in the 4D mixture model, taking the posterior mean, is 95.55% for Sgr, 2.75% for MW, and 1.70% for M54. The member fraction (c_i) for each component in the 1D mixture model, taking the posterior mean, is 71.65% for Sgr, 2.38% for MW, and 25.97% for M54. We note that the tidal radius r_t for M54 tends to be very large in the posterior distribution. We have tried to enforce a strong Gaussian prior using the literature value 0.165° (Harris, 1996, 2010 edition) as the mean, which will restrict the range of posterior distribution around 0.165°, but we do not observe any improvement in the residual distribution or any change in our results. If we take the MAP estimation, the probability mass of normalized King profile within radial distance $8° \leq r \leq 1°$ is 13%. The distribution is still dominated by the central area. With these considerations, we decide to use the less informative prior which will lead to a large tidal radius.

We note first that our estimate of the posterior PDF for the Milky Way component of the proper motion distribution is not well converged. This is due to the relatively small number of MW stars that survive our initial proper motion selection (Figure 3.2; the inferred contribution of MW stars to the 4D model is $\lesssim 3\%$).

Figure 3.5 displays the distribution of projected positions in the data (left panel), best-fitting model (middle-left panel), residuals normalised by Poisson uncertainties estimated from the expected values under the best-fitting model (middle-right panel), and the histogram of the normalised residuals (right panel). Figure 3.6 displays the probability distribution for circular radial coordinate $R_{\rm circ} = \sqrt{x^2 + y^2}$, with individual contributions from the modelled M54, Sgr and MW components indicated. Here the observed data are binned for illustrative purposes only, as the models are fit to the discrete data for stellar position. The lower sub-panel in Figure 3.6 shows residuals, normalised by the Poisson uncertainty. We find that our mixture model provides a reasonably good fit, with normalised residuals approximately following a unit-normal distribution (right panel of Figure 3.5 and bottom panel of Figure 3.6).

The contours in Figure 3.7 represent posterior PDFs that we estimate for spatial centroids (left panel) of M54 and Sgr, and mean proper motions (right panel); for Sgr, for which we allow the mean proper motion to vary linearly with projected positions from

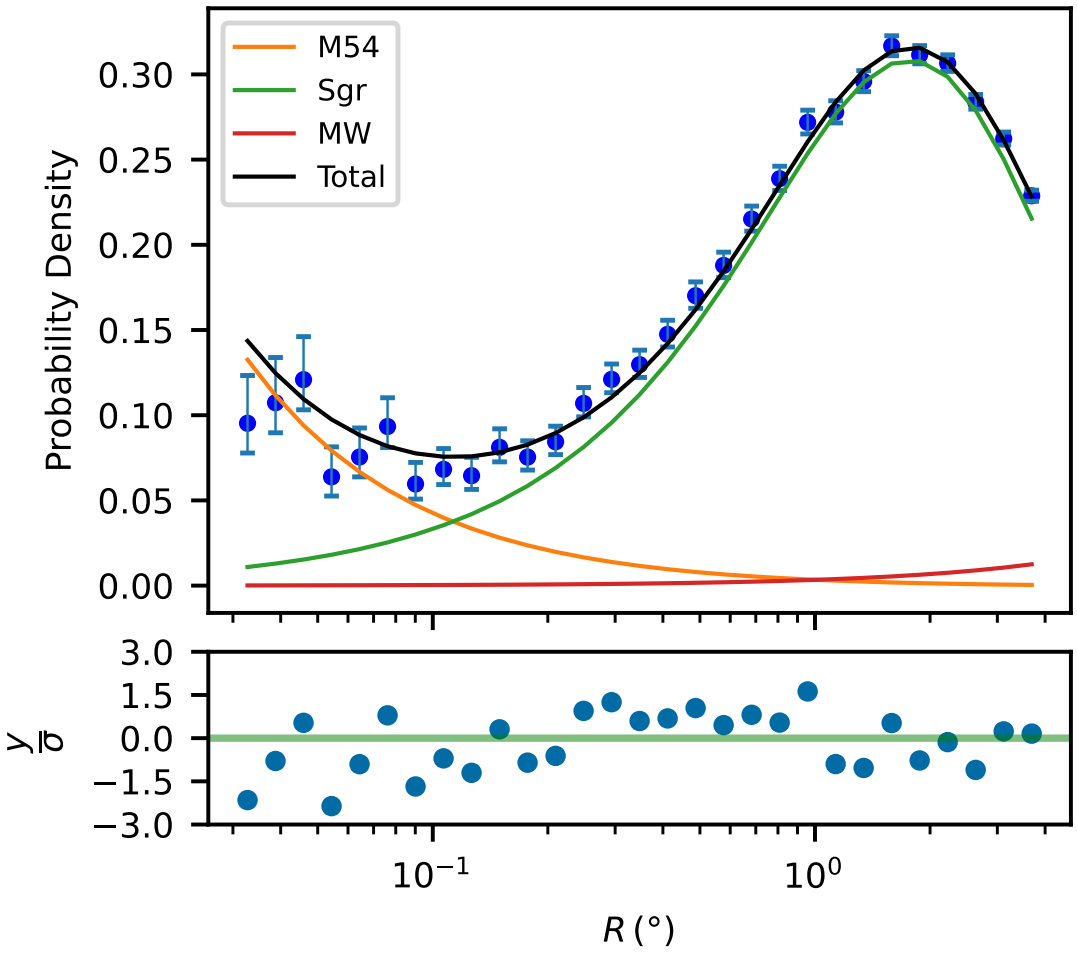

FIGURE 3.6: *Top:* Probability density of circular radial coordinate $R_{\rm circ} = \sqrt{x^2 + y^2}$. Points with errorbars are the data. Overplotted is our best-fitting model, with individual contributions from M54, Sgr and Milky Way components indicated by colored curves. *Bottom:* residuals normalized by Poisson uncertainties.

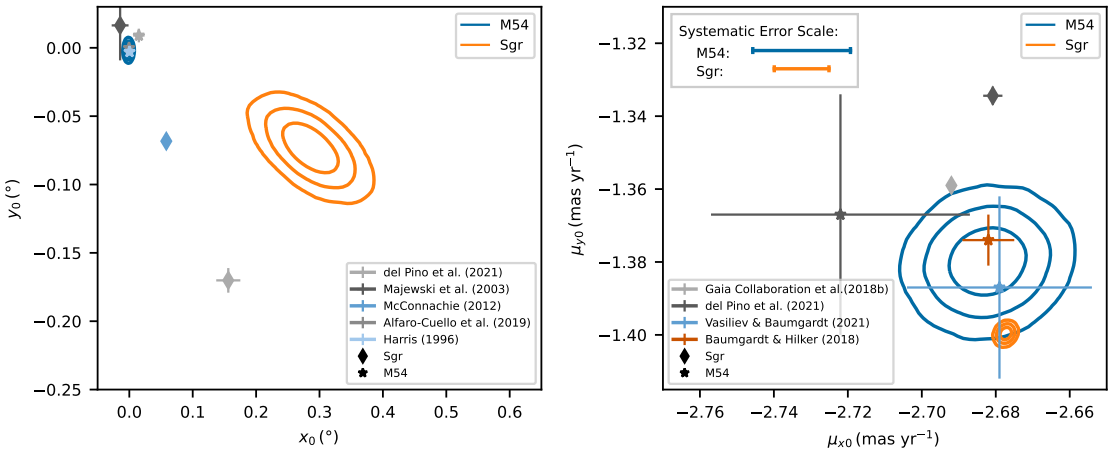

FIGURE 3.7: Contours enclosing 68%, 95% and 99% of posterior probability for model parameters specifying projected centroids (left) and mean proper motion coordinates (right) of M54 and Sgr components. For the Sgr component, for which our proper motion model has mean varying linearly with position, the plotted mean is calculated at the centre of Sgr. Markers indicate previously-published measurements (filled circles for M54, filled stars for Sgr). The top left lines in the right plot indicate the expected magnitude of systematic error in the mean proper motion estimated for each object (Vasiliev and Baumgardt, 2021).

the spatial centroid, the mean proper motion is evaluated at the fitted centroid. The inferred spatial centres of M54 and Sgr are offset by an angle of $|\Delta \boldsymbol{s}| = 0.295 \pm 0.029°$—corresponding to a physical separation of 0.135 ± 0.013 kpc at the adopted distance of 26.28 kpc—with M54 projected to the northwest of the Sgr centre.

The inferred mean (central) proper motions of M54 and Sgr are offset by $\Delta \boldsymbol{\mu} = [0.0049, -0.0197] \pm [0.0068, 0.0062]$ mas yr^{-1}, with M54 moving more slowly than Sgr toward the south. However, the precision of mean proper motions estimated for extended objects is limited by spatial covariance within the *Gaia*'s EDR3 proper motion catalog (Lindegren et al., 2021). We use Equation 2 from Vasiliev and Baumgardt (2021) to estimate the magnitude of this systematic error 'floor', which depends on the angular size of the object in question. Using the core radius $r_c = 0.0017°$ for M54 and half-light radius $r_h = 5.083°$ for Sgr to represent the relevant angular scales of these objects, the corresponding systematic errors are $\epsilon_{\rm sys} \approx 0.026$ mas yr^{-1} for M54 and $\epsilon_{\rm sys} \approx 0.015$ mas yr^{-1} for Sgr. Thus the offset that we infer between the mean proper motions of M54 and Sgr is similar to the expected contribution from systematic error. Thus the offset that we infer between the mean proper motions of M54 and Sgr has a similar magnitude to the expected systematic error.

Fig 3.8 displays posterior PDFs for mean line-of-sight velocities of M54 and Sgr. We infer mean values of $v_0 = 139.63 \pm 0.92$ km s^{-1} for M54 and $v_0 = 143.74 \pm 0.69$ km s^{-1} for Sgr (evaluated at the inferred centroid of Sgr), for an offset of $\Delta v_0 = 4.1 \pm 1.2$ km s^{-1}. We infer a significant gradient in Sgr's line-of-sight velocities, $e_x = -1.68 \pm 0.57$ km s^{-1} deg^{-1} and $e_y = -4.80 \pm 0.74$ km s^{-1} deg^{-1}, implying a gradient of magnitude ~ 5 km s^{-1} deg^{-1} (~ 10 km s^{-1} kpc^{-1}), similar to the gradient previously reported by del Pino et al. (2021).

Taken at face value, these results suggest that M54 and Sgr are offset in phase space, with the detected offsets significant at the 10σ and 3.4σ levels in projected sky position and line-of-sight velocity components, respectively. The inferred proper motion offset,

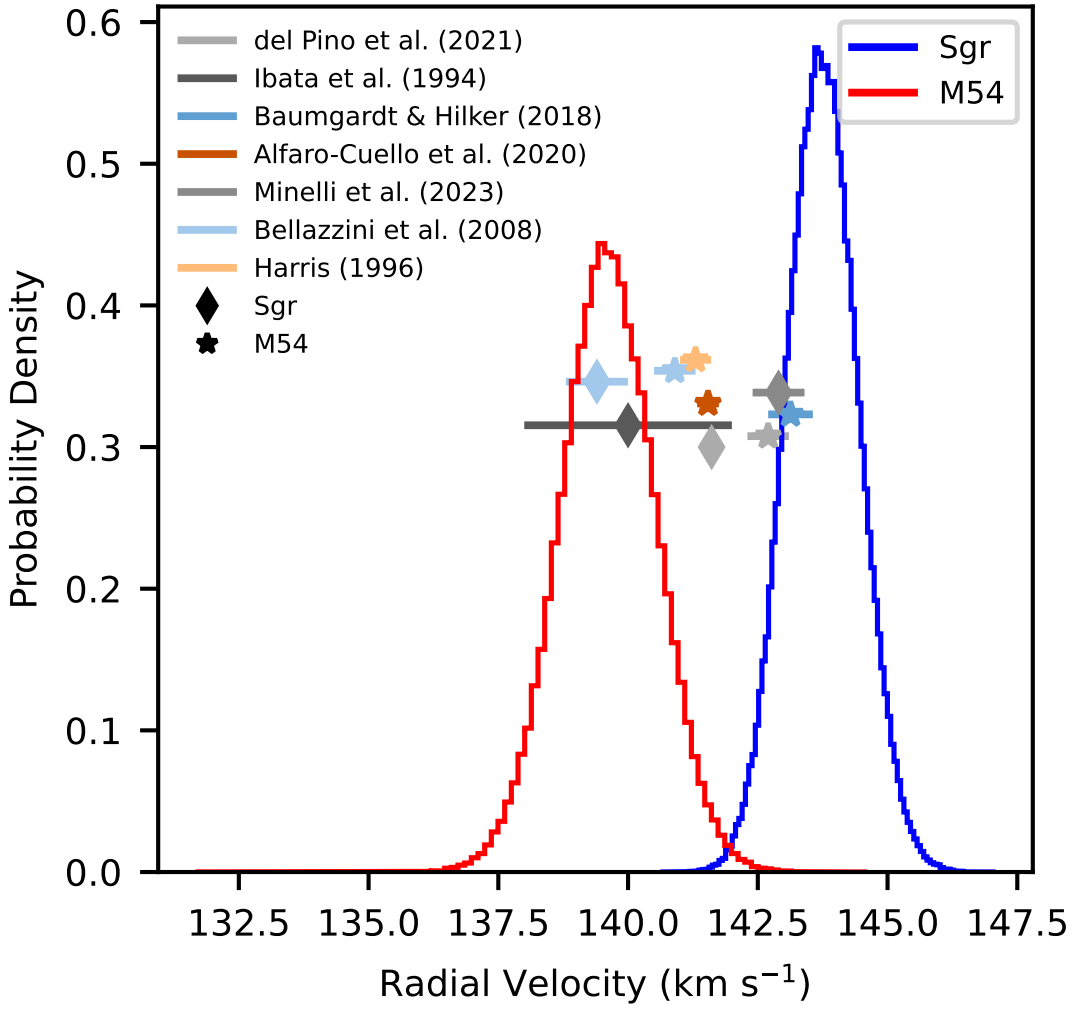

FIGURE 3.8: Posterior probability distribution of the mean line-of-sight velocity of Sgr (blue) and M54 (red), from our mixture modeling of our sample selected from the Apogee (DR17) survey. Dots and stars represent previously-published measurements for Sgr and M54, respectively, with error bars representing 1σ uncertainty.

while significant at the $\sim 3\sigma$ level based on our posterior PDF alone, is similar to the expected level of systematic error.

3.5 Discussion

3.5.1 Comparison to Previous work

For comparison with our inferences of the centroids and mean motions of M54 and Sgr, Figures 3.7 and 3.8 indicate previous measurements found in the literature. Our inference for the spatial centre of M54 is consistent with those reported by del Pino et al. (2021), Alfaro-Cuello et al. (2019), and Harris (1996). However, our inference for the spatial centre of Sgr is offset, by $\sim$ 15 arcmin, from the center listed in the review by McConnachie (2012) (which uses the value originally reported by Ibata, Gilmore, and Irwin (1994)), and by similar amounts from measurements reported by Majewski et al. (2003)

TABLE 3.2: Free parameters of model fit to 1D APOGEE sample of line-of-sight velocity, including priors and quantiles at $(0.1587, 0.5, 0.8413)$.

	Prior	Params	$(0.1587, 0.5, 0.8413)$ Quantile
Member Fraction	Dirichlet$(1,1,1)$	m_1	$(0.6047, 0.7206, 0.8242)$
		m_2	$(0.03337, 0.06656, 0.1336)$
Sgr $v_{\rm LOS}$	U$[100, 200]$	v_0 (km s^{-1})	$(143.2, 143.9, 144.6)$
	U$[10, 100]$	σ (km s^{-1})	$(12.48, 12.91, 13.37)$
	U$[-10, 10]$	e_x (km s^{-1} deg^{-1})	$(-2.252, -1.675, -1.115)$
	U$[-10, 10]$	e_y (km s^{-1} deg^{-1})	$(-5.534, -4.798, -4.064)$
MW $V_{\rm LOS}$	U$[-50, 50]$	v_0 (km s^{-1})	$(-30.07, -11.62, 8.933)$
	U$[10, 150]$	σ (km s^{-1})	$(49.34, 62.69, 80.41)$
M54 $V_{\rm LOS}$	U$[100, 200]$	v_0 (km s^{-1})	$(138.7, 139.6, 140.5)$
	U$[1, 100]$	σ (km s^{-1})	$(8.153, 8.907, 9.630)$

and del Pino et al. (2021). Notably, *none* of the listed measurements of Sgr's centre agree with each other. This situation is not entirely surprising, given the different instrumental sensitivities and complex mix of stellar populations near Sgr's centre. The measurement by Majewski et al. (2003) coincides with a steep 'cusp' that they detect at the position of M54, which might reflect contamination of the M giant sample by the relatively young and metal-rich M54 component reported in later work (Alfaro-Cuello et al., 2019). Indeed del Pino et al. (2021) find that the inclusion of M54 stars in their sample would shift the fitted centroid of Sgr toward M54. Their measurement that we show in Figure 3.7 uses a sample that masks a circular region of radius 0.16° centred on M54, chosen to excise the cluster within its King tidal radius (for comparison, our central mask described in Section 3.2.1 has radius 0.03°). However, del Pino et al. (2021) downplay the resulting offset from M54, noting the potential for systematic errors due to the *Gaia* scanning pattern that is apparent in their chosen sample from Gaia DR2. Thus ours is the first inference of an offset between the spatial centres of M54 and Sgr that is based on a mixture model that simultaneously accounts for both objects within the same data set. Given our selection of a relatively bright magnitude limit ($G < 17.3$; Section 3.2.1), our data does not show an visible scanning pattern, and thus our result of offset should be less susceptible to systematic errors arising from the spatial dependence of *Gaia's* faint magnitude limit.

Our inference for M54's proper motion vector is consistent with other recent *Gaia*-based measurements reported by Baumgardt and Hilker (2018), del Pino et al. (2021), and Vasiliev and Baumgardt (2021). However, our inference for Sgr's proper motion (evaluated at Sgr's centre) is statistically inconsistent with those reported by Gaia Collaboration et al. (2018a) and del Pino et al. (2021), with our measurement indicating a larger component toward the south. Again we see that all reported measurements for Sgr disagree with each other. Gaia Collaboration et al. (2018a) note that their PM measurements are affected by *Gaia*'s scanning pattern and varying astrometric incompleteness in *Gaia* DR2, which contributes to a systematic error that they estimate to be $\sigma_{sys} \sim 0.030\,\mathrm{mas\ yr^{-1}}$ and $\sim 0.036\,\mathrm{mas\ yr^{-1}}$ in $\mu_\alpha \cos\delta$ and μ_δ, respectively, similar to the offset between their result and ours. The measurements by Gaia Collaboration et al. (2018a) and del Pino et al. (2021) are based on the *Gaia* DR2 catalogue and the proper motion zero-points are both different and spatially varying between the DR2 and DR3 catalogue and this systematic error may account for the offset compared to our result. In any case, even taking any of the available measurements for Sgr's proper motion vector at face value, one finds a similarly significant offset (albeit with reversed direction in the case of the previous measurements based on *Gaia* DR2) with respect to our inference for the proper motion of M54. Again, however, we note that the apparent offset is similar in magnitude to the

expected contribution from systematic error.

Finally, Fig 3.8 shows that previously published measurements of the mean line-of-sight velocities of M54 and Sgr are scattered between the values we infer. For M54, our estimate (evaluated at the inferred centre of Sgr) is in reasonable agreement with those reported by Harris (1996), Bellazzini et al. (2008) and Alfaro-Cuello et al. (2020), but more discrepant (with our measurement having a smaller line-of-sight velocity) with those of Baumgardt and Hilker (2018) and del Pino et al. (2021). For Sgr, our result agrees well with that of Minelli et al. (2023), marginally with those reported by McConnachie (2012) and del Pino et al. (2021), and poorly (with our measurement being $\sim$ 4 km s^{-1} more positive) with that of Bellazzini et al. (2008). This scatter likely reflects not only systematic errors due to the different zero-points of the different instrumental setups, but also the different criteria used to select and/or identify M54 and Sgr samples. For example, Minelli et al. (2023) select their Sgr sample from fields observed outside the central region containing M54, with a broad CMD filter chosen to pass a wide range of age and metallicity. Other studies (Bellazzini et al., 2008, e.g.) define M54 and/or Sgr samples by applying relatively blue and red filters along the red giant branch sequences; as previously discussed (Section 3.1), this selection can confuse a young, metal-rich component in M54 (Alfaro-Cuello et al., 2019) with Sgr, perhaps helping to explain why many of the previous results lie between the mean velocities we measure for the two objects. Again we emphasise that our mixture model's separation between M54 and Sgr components is based only on the observed distribution of phase-space coordinates, and is agnostic regarding the colour/magnitude and hence age/metallicity properties of each object.

3.5.2 Robustness to sample selection and modelling assumptions

The most significant offset we detect between Sgr and M54 is between their 2D spatial centroids. We now examine the extent to which this offset may be driven by our choice of modelling assumptions and sample selection. As described in Section 3.2.1, we selected our sample of stellar positions (and proper motions) to be spread over a circular field of radius 4° (excluding the crowded region within a field of radius 0.03°) centred on M54. Our model assumes that within this region, the stellar surface density of Sgr is well described by an elliptical Plummer profile. However, as a result of ongoing tidal interaction with the Milky Way, Sgr is known to display distorted morphology in its outer regions, ultimately extending to tidal tails that encircle the sky (Mateo et al., 1996; Majewski et al., 2003). To date, the most detailed view of Sgr's internal stellar structure and kinematics comes from the *Gaia*-based study by del Pino et al. (2021), who report a central bar-like feature extending out to the tidal tails, and an overall triaxial morphology, with a slowly rotating ($V_{\rm rot} \sim 4$ km s^{-1}) central region of radius $\sim$ 500 pc that is embedded within an outer envelope that appears to be expanding along its longest axis.

In order to gauge the effect of Sgr's complicated morphology on our inference about its centre, we repeat our fits using samples selected over smaller fields (still centred on M54). Fig 3.9 shows 3σ contours (i.e., enclosing 99.7% of the probability mass) from posterior PDFs for the centroids of M54 and Sgr, obtained using samples spanning fields of radius 4° (the original choice), 3° and 2°. Unsurprisingly, all cases return statistically identical inferences for the centroid of M54. For Sgr, contours for all cases continue to enclose the centroid inferred from our original sample; however, as the field size decreases, the contours expand and we see a systematic reduction in the inferred offset from M54. For a field radius of 2°, the offset is detected only marginally, with the 3σ contour overlapping the inferred centroid of M54.

The inflation of statistical uncertainty as the field radius decreases is unsurprising, as the sample becomes more confined to the region well within Sgr's fitted Plummer radius

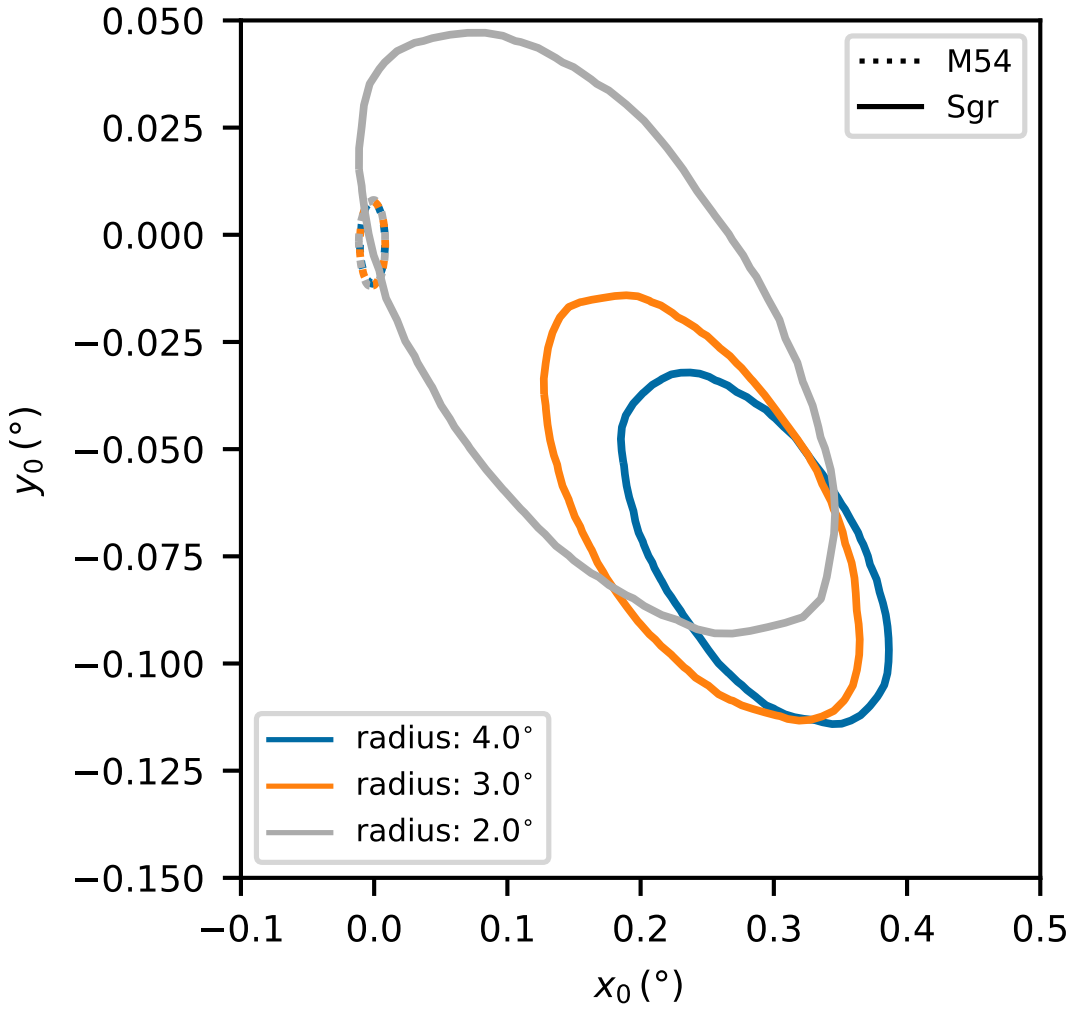

FIGURE 3.9: 3σ level contour of the posterior probability distributions for the spatial centres of M54 (dotted) and Sgr (solid). Contours are color-coded by the radius of the sky coverage for different adopted samples.

($R_p \sim 5°$), where the 2D density is close to uniform. The systematic shift in the inferred Sgr centroid, toward M54 as the field radius decreases, is similar in magnitude to the increase in statistical error. Thus the systematic component cannot be neglected, and we must acknowledge that the significance with which we detect a spatial offset between M54 and Sgr is vulnerable to model mismatch, particularly with regard to the stellar density distribution toward the outer regions of Sgr. However, residuals with respect to best-fitting models (Figures 3.5 and 3.6) do not reveal obvious signs of model mismatch.

In order to examine more quantitatively the potential for asymmetric morphology within Sgr to induce spurious detection of an offset from M54, we fit an alternative model for Sgr's 2D spatial configuration that explicitly includes an asymmetric component.

The alternative asymmetric model is constructed by modifying Equation 3.3. The original matrix $\boldsymbol{R}$ from Equation 3.3 is

$$\boldsymbol{R} = \begin{pmatrix} 1 & 0 \\ 0 & \frac{1}{(1-\epsilon)} \end{pmatrix} \boldsymbol{R}_\theta \left(\boldsymbol{s} - \boldsymbol{s_0}\right) \tag{3.24}$$

Now we construct the asymmetric model to stretch the distribution along just one of the semi-major axes:

$$\boldsymbol{R'} = \begin{pmatrix} \frac{|\boldsymbol{R}_{00}|(1-s_p)}{2s_p} + \frac{\boldsymbol{R}_{00}(1+s_p)}{2s_p} \\ \boldsymbol{R}_{10} \end{pmatrix} \tag{3.25}$$

where $\boldsymbol{R}_{ij}$ represents the element of the ith row and jth column from $\boldsymbol{R}$ (index starts from 0). This expression ensures that

$$\boldsymbol{R'}_{00} = \begin{cases} \boldsymbol{R}_{00} & \text{if } \boldsymbol{R}_{00} >= 0 \\ \boldsymbol{R}_{00}/s_p & \text{if } \boldsymbol{R}_{00} < 0. \end{cases} \tag{3.26}$$

We construct the asymmetric model by replacing the $R_e^2 = \boldsymbol{R}^\top \boldsymbol{R}$ in Equation 3.6 with $R_e^2 = \boldsymbol{R'}^\top \boldsymbol{R'}$. The normalisation factor k_P in Equation 3.6 is recalculated using the new expression. The new parameter s_p controls how much one side of the Sgr spatial distribution is elongated. The prior on the parameter s_p is $\mathrm{U}[1, 5]$.

We fit the asymmetric model using the software package Dynesty (Speagle, 2020; Koposov et al., 2023; Skilling, 2004; Higson et al., 2019; Feroz, Hobson, and Bridges, 2009), which returns an estimate of the marginalised likelihood, or 'evidence', as well as a random sample from the posterior. The evidence provides a metric for model selection.

The contours in Figure 3.10 represent posterior PDFs for the asymmetric stretch factor, s_p, and the inferred centroid of Sgr. The observed degeneracy indicates that for sufficiently large s_p, near the 2σ contour of our posterior PDF, Sgr's centroid can shift to coincide with the center of M54 at $(x, y) = (0, 0)$. However, comparing results from our asymmetric and original symmetric model, the natural logarithm of the evidence ratio is 3.13 ± 0.45, in favor of the simpler, symmetric model. In order to interpret this numerical result, we perform a simulation in which we fit our symmetric and asymmetric models to mock data generated under our best-fitting (to the real data) symmetric model. In this case we know the input model has no inherent asymmetry, and we obtain a similar evidence ratio, which has a logarithm of 3.03 ± 0.44, again in favor of the symmetric model. We conclude that, while the offset we infer between centroids of M54 and Sgr can potentially be caused by asymmetry in Sgr's morphology, the real data do not give reason to prefer at least our simple asymmetric model over the original symmetric one.

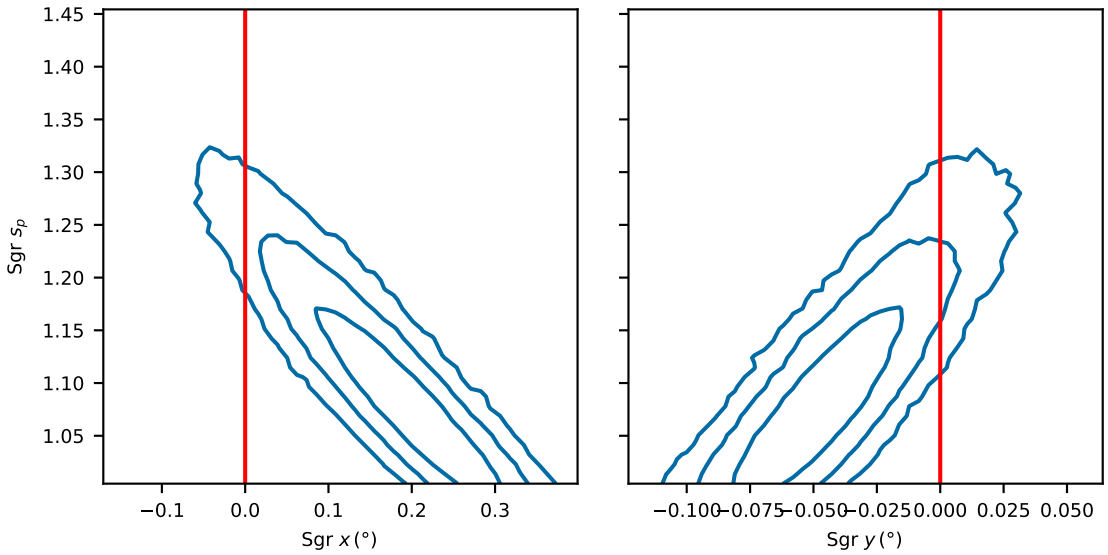

FIGURE 3.10: Contours enclosing 68%, 95% and 99% of posterior probability for model parameters specifying the one-sided 'stretch' factor of an asymmetric model for Sgr, and the x, y components of Sgr's centroid. Red vertical lines mark the origin, which is chosen to coincide with the center of M54 (from Alfaro-Cuello et al. 2019.

3.5.3 Colour/magnitude distribution

We reiterate that our mixture model is agnostic regarding the colour/magnitude distribution of stars belonging to the individual components of M54, Sgr and the Milky Way. This represents a departure from most previous analyses of M54 and/or Sgr, which typically analyse separate samples that are pre-selected from relatively blue and red sequences defined along the red giant branch (e.g., Majewski et al., 2003; Bellazzini et al., 2008). In contrast, our inferences of mixing fraction and structural/kinematic parameters for each mixture component are informed only by the observed stellar positions and motions. Afterwards, however, we can use the inferred parameters and mixing fractions to examine the corresponding colour/magnitude distribution of each component. For each of M54, Sgr and the Milky Way, Figure 3.11 displays the number of stars per pixel in colour/magnitude space having probability of membership $> 50\%$ in that component.

We see that the Milky Way contribution tends to be fainter and bluer than the M54 and Sgr populations, only sparsely populating the red giant sequences. Sgr stars lie primarily to the red side of our CMD filter, with a prominent red clump visible at $G \sim 16.7$. Finally, we see that while M54 is composed primarily of stars along the blue ridge of our CMD filter, it has a population of high-probability members along the redder sequence as well. This result is broadly consistent with that of Alfaro-Cuello et al. (2019), who use MUSE spectroscopy to separate the M54 region into an old (12.2 Gyr), metal-poor ([Fe/H]$= -1.41$) population a young (2.2 Gyr), metal-rich ([Fe/H]$= -0.04$) population and an intermediate-age (4.3 Gyr), metal-rich ([Fe/H]$= -0.29$) population, with the first two being more centrally concentrated than the last. It is this central concentration that associates the young, metal-rich population with M54 in our model. Alfaro-Cuello et al. (2019) speculate that these stars may have formed in situ in the nuclear region, in response either to the funnelling of gas during Sgr's most recent pericentric passage of the Milky Way, or to the sinking of enriched gas to the centre of a sufficiently massive M54.

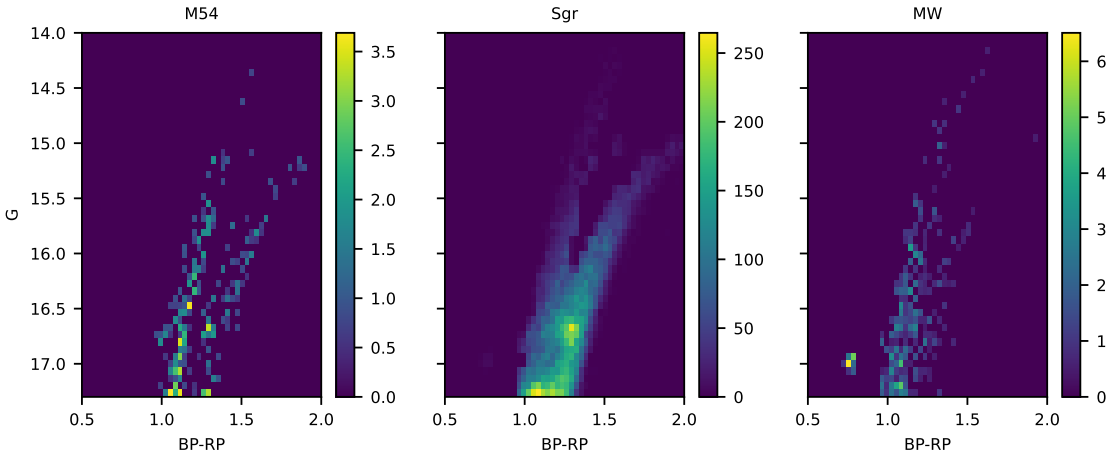

FIGURE 3.11: Color/magnitude distributions for stars inferred to have > 50% probability of membership in the M54 (left), Sgr (middle) and MW (right) components. The colour bar indicates the number of stars in each bin.

3.5.4 Orbits of M54 and Sgr

If M54 is offset from the centre of Sgr in phase space, then it becomes interesting to trace the history of the M54/Sgr interaction, which will depend on the masses and internal structure of both objects as well as the external tidal field. In order to explore at least some aspects of this dependence, we consider here a simplified 'toy' model in which M54 is a point mass and Sgr is embedded within an extended dark matter halo that follows the flexible 'CoreNFW' (cNFW) density profile of Read, Walker, and Steger (2018). This spherically-symmetric halo model is defined by the enclosed-mass profile

$$M_{\rm cNFW}(r) = f^n M_{\rm NFW}(r), \tag{3.27}$$

where

$$M_{\rm NFW}(r) = M_{200}\frac{\ln(1+r/r_s) - r/r_s(1+r/r_s)^{-1}}{\ln(1+c_{200}) - c_{200}(1+c_{200})^{-1}} \tag{3.28}$$

is the 'NFW' profile that characterizes halos produced in cosmological N-body simulations that assume 'cold' dark matter (Navarro, Frenk, and White, 1996; Navarro, Frenk, and White, 1997). Here, $M_{200} = M_{\rm NFW}(r_{200})$ is a proxy for halo mass, with r_{200} the radius of the sphere inside which the mean density is $3M_{200}/(4\pi r_{200}^3) = 200\rho_c$, where $\rho_c = 3H_0^2/(8\pi G)$ is the critical density of the Universe (we assume the Hubble constant has value $H_0 = 70$ km s^{-1} Mpc^{-1}). With r_{200}, the scale radius r_s defines halo concentration, $c_{200} \equiv r_{200}/r_s$. The function

$$f^n \equiv \left[\tanh\left(\frac{r}{r_c}\right)\right]^n \tag{3.29}$$

allows the 'cuspy' ($d\log\rho/d\log r = -1$) inner behavior of the NFW profile to be transformed, to a degree controlled by parameter $0 < n \leq 1$, to a 'core' of uniform density within a sphere of radius r_c.

In order to examine sensitivity to the structure of Sgr's dark matter halo, we consider two possibilities, both of which assume that M54 is a point particle of mass $M_{\rm M54} = 1.41 \times 10^6\,{\rm M}_\odot$ (Baumgardt and Hilker, 2018) and Sgr consists of a stellar component, described by a spherical Plummer model, embedded within a cNFW dark matter halo.

In the first case, the cNFW halo has $r_c = 0$, which simplifies to the original NFW profile. In the second case, the cNFW halo has a fully-formed ($n = 1$) core of radius, $r_c = r_p$, that is assumed to equal the Plummer radius fit to the observed stellar density profile (Read, Agertz, and Collins, 2016). In both cases, we adopt a dark matter halo concentration of $c_{200} = 10$, and for Sgr a total stellar mass (within the bound Plummer sphere) of $M_{*,\mathrm{Sgr}} = 2 \times 10^7\,\mathrm{M}_\odot$ (McConnachie, 2012) (we find no sensitivity to different plausible choices for Sgr's stellar mass, such as the value of $M_{*,\mathrm{Sgr}} = 1 \times 10^8\,\mathrm{M}_\odot$ from Vasiliev and Belokurov (2020)). For both dark matter profiles, we choose M_{200} so that the dark matter mass enclosed within the Plummer radius matches dynamical mass estimated as $M(r_{\mathrm{half}}) = 2.5 r_{\mathrm{p}} \sigma_v^2 / G$ (Walker et al., 2009a), where we adopt $r_p = 5.092°$ as the MAP result from our modeling and $\sigma_v = 11.4$ km s^{-1} is the velocity dispersion Ibata et al. (1997). For the NFW and cNFW profiles, this requirement gives $M_{200} = 1.29 \times 10^9\,\mathrm{M}_\odot$ and $M_{200} = 2.10 \times 10^9\,\mathrm{M}_\odot$, respectively. In order to account for any effect of the Large Magellanic Cloud (LMC) on the orbits of M54 and Sgr, we include an LMC potential that we model using a Hernquist profile with total mass 1.38×10^{11} M$_\odot$ and scale radius 16.09 kpc (Erkal et al., 2019); however, we find that the inclusion or exclusion of the LMC potential has negligible effect on our results.

We sample the present-day 2D position, proper motions and line-of-sight velocities for both M54 and Sgr from the posterior PDFs inferred from our mixture models. We include the systematic errors (Vasiliev and Baumgardt, 2021) in the proper motion samples by adding Gaussian noise to the proper motion components sampled from our posterior PDF, accounting for uncertainty 'floors' of $\epsilon_{\mathrm{sys}} = 0.026$ mas yr^{-1} for the proper motion components of M54 and $\epsilon_{\mathrm{sys}} = 0.015$ mas yr^{-1} for Sgr. We draw present-day line-of-sight distances to M54 and Sgr independently from a normal distribution with mean 26.28 kpc and standard deviation 0.33 kpc, corresponding to the measurement by Baumgardt and Vasiliev (2021) of the distance to M54. For Sgr, assumed here to be spherically symmetric, we sample the Plummer radius from our posterior PDF for r_h. For the LMC, we adopt the present-day phase space coordinates from Gaia Collaboration et al. (2018a).

Given the stated initial conditions, we use the software package `gala` (Price-Whelan et al., 2022) to calculate the orbits of M54, Sgr and the LMC within a Milky Way potential that adopts `gala`'s MilkyWayPotential class, which assumes a disk model from Bovy (2015). We choose `gala`'s RK5Integrator, which uses a fifth order Runge-Kutta method. In order to gauge the effects of dynamical friction on M54 from both Sgr and the MW and on Sgr and the LMC from the MW, we calculate orbits with and without using galpy's ChandrasekharDynamicalFrictionForce class (Bovy, 2015), which implements the Chandrasekhar dynamical friction force following Petts, Read, and Gualandris (2016). For each combination of NFW vs. cNFW for Sgr's dark matter profile and with/without dynamical friction implemented, we draw 100 samples from our posterior PDFs that provide initial conditions, and then calculate the corresponding orbits over the past 1 Gyr. The timestep is 5 Myr and the number of steps is 200.

For each computed orbit, Fig 3.12 depicts the recent history of the (3D) spatial offset between M54 and the centre of Sgr, tracing back 1 Gyr from the present day. Left and right columns show results using the NFW and coreNFW model, respectively, for Sgr's dark matter halo; top and bottom panels show results obtained without and with dynamical friction implemented.

For cases where the present-day offset is $\lesssim 0.7$ kpc, we observe a dependence on the dark matter density profile within Sgr. If Sgr's dark matter halo follows the NFW profile, we find that most orbits are approaching apocentre, with the M54/Sgr separation increasing from an offset as small as ~ 0.1 kpc at the most recent pericentric passage, which occurred between $\sim 15 - 40$ Myr ago. In the absence of dynamical friction, the orbit remains approximately unchanged for the past Gyr for most of the samples (upper

left panel of Figure 3.12). With dynamical friction implemented (lower left panel of 3.12), the offset at apocentre has decreased steadily from a value of ~ 1.5 kpc over the past 700 Myr.

In contrast, if Sgr's dark matter halo follows the adopted coreNFW profile, then present-day offsets that are $\lesssim 0.7$ kpc are close to pericentre for most of the samples, after a most recent apocentre $\gtrsim 100$ Myr ago, at which the offset was $\gtrsim 0.5$ kpc (right panels of Figure 3.12). As expected, the implementation of dynamical friction has relatively little effect when the dark matter halo is cored (Read et al., 2006; Inoue, 2009), allowing M54 to 'wobble' about the centre indefinitely (Cole et al., 2012).

If the present-day offset is $\gtrsim 0.7$ kpc, and thus dominated by a large offset in line-of-sight distance between M54 and Sgr, all sampled orbits would imply that M54 fell into Sgr within the past 200 Myr, regardless of whether Sgr's dark matter halo follows a NFW or cNFW profile. However, this scenario seems unlikely, as one expects Sgr to be losing mass, not accreting, during this timeframe that includes Sgr's own pericentric passage about the Milky Way (Vasiliev, Belokurov, and Erkal, 2021).

We emphasise that our orbit calculations neglect realistic details of the Sgr/M54 system—most notably, Sgr's tidal disruption by the Milky Way. The orbits that we calculate imply that Sgr's most recent pericentric passage about the Milky Way brought it within ~ 15 kpc of the Galactic centre, just ~ 45 Myr ago, consistent with the Sgr orbit inferred by (Vasiliev, Belokurov, and Erkal, 2021). However, even if we restrict our calculations only to the previous 50 Myr, the qualitative conclusion remains that an M54/Sgr system that has internal offset $\lesssim 0.7$ kpc tends to be appropaching apocentre if Sgr is embedded within an NFW halo, and near pericentre if Sgr is embedded within a cored halo. A more thorough investigation of the history of the M54/Sgr interaction would require updating previous N-body approaches (e.g., Bellazzini et al., 2008; Herlan, Mastrobuono-Battisti, and Neumayer, 2023) in light of the present-day phase-space coordinates presented above.

3.6 Summary & Conclusions

Motivated by longstanding questions regarding the formation and orbital histories of nuclear star clusters, here we have analyzed the 5D (sky positions and proper motions from *Gaia* EDR3, line-of-sight velocities from APOGEE DR17) structure and kinematics of the M54/Sgr system, the only example of a NSC/host system for which such multi-dimensional data are available. In order to obtain simultaneous estimates of the centers of M54 and Sgr in each of these coordinates, we have constructed and fit a mixture model that accounts also for contamination from the Milky Way foreground/background. Our approach differs from most previous efforts, which consider M54 and/or Sgr samples separately after filtering according to colour/magnitude and/or 2D spatial criteria. In analysing both M54 and Sgr populations simultaneously within the same sample, our inferences about offsets between the two objects incur fewer systematic errors that arise when comparing estimates made using either independent data sets or independent subsamples of those data sets.

We have reported statistically significant offsets in the spatial centres and line-of-sight velocities of M54 and Sgr. The offset between the spatial centres is 0.295 ± 0.029 degrees, corresponding to a projected (2D) offset of 0.135 ± 0.013 kpc at the distance of 26.28 kpc. The offset between the line-of-sight velocities is 4.1 ± 1.2 km s^{-1}. The offset between the PM centres of the M54 and Sgr dSph is $[\Delta\mu_\alpha \cos\delta, \Delta\mu_\delta] = [0.0049, -0.0197] \pm [0.0068, 0.0062]$ mas yr^{-1}, comparable to the expected systematic error.

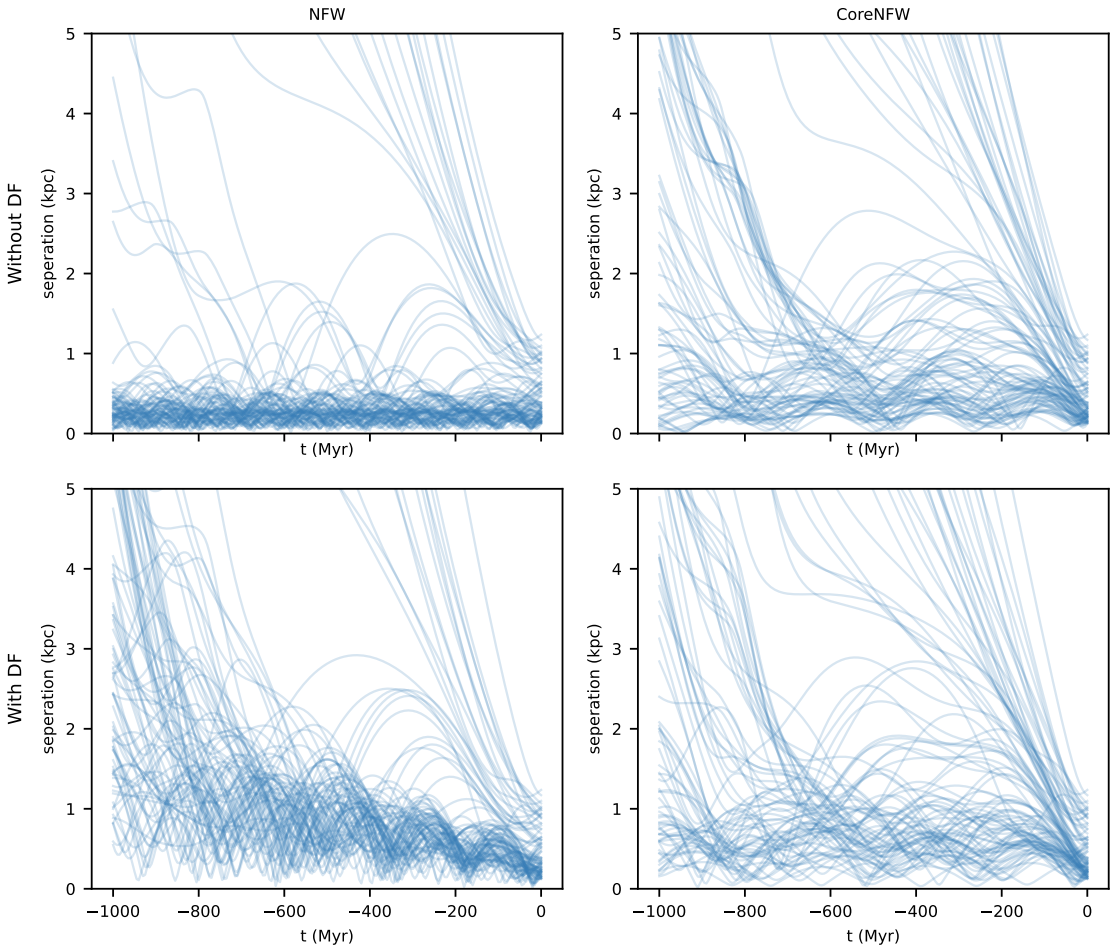

FIGURE 3.12: Evolution of the 3D spatial offset between the centers of M54 and Sgr, with orbits integrated backward in time from the present day ($t = 0$), with boundary conditions drawn from posterior PDFs of our 5D phase-space models (present-day distances to M54 and Sgr are drawn independently from a normal distribution with mean 26.28 kpc and standard deviation 0.33 kpc, based on the distance measurement of Baumgardt and Vasiliev (2021)). Each line represents the orbits calculated from one set of initial conditions drawn from the posterior. Results shown in left/right panels are calculated using NFW/CoreNFW potentials for Sgr's dark matter halo. Orbits shown in the top/bottom rows neglect/include an implementation of dynamical friction.

By far the most significant offset we infer is between the spatial centres of M54 and Sgr. However, this result comes with the caveat that the degree of statistical significance is sensitive to our choice of sample field size. This sensitivity points to the possibility that the inferred offset may be driven by large-scale asymmetry of the spatial distribution of stars within Sgr. While our fiducial model allows flattened elliptical morphology, we find that the inferred offset between M54 and Sgr can be reduced if we further allow for bilateral asymmetry. However, we find that standard criteria for model selection disfavour our asymmetric model over the fiducial one. We conclude, then, that the present data are reasonably well fit by our fiducial model, with M54 significantly offset from Sgr, and do not favour an alternative in which M54 is located exactly at the centre of an asymmetric Sgr host.

Based on our estimates of the 5D phase-space coordinates of M54 and Sgr at the present day, we also investigated the recent orbital history of the interacting pair. Treating M54 as a point mass and neglecting mass lost from Sgr due to tidal disruption, we calculate orbits within a potential that includes both objects as well as the Milky Way and LMC. We find that if Sgr is embedded in a cuspy (NFW) dark matter halo, then the M54/Sgr orbit is currently most likely approaching apocentric when the present-day offset is $\lesssim 0.7$ kpc, having decayed under dynamical friction from earlier apocentres $\gtrsim 1$ kpc. In contrast, if Sgr's dark matter halo has a central core, then the M54/Sgr orbit is near pericentre if the present-day offset is $\lesssim 0.7$ kpc. If the present-day offset between M54 and Sgr is $\gtrsim 0.7$ kpc, and thus dominated by an offset in the line-of-sight distance, the calculated orbits would imply that M54 fell into Sgr within the past 200 Myr regardless of whether Sgr's dark matter halo is cored or cusped.

Finally, the results of our mixture model imply that in addition to a dominant population of old, metal-poor stars, the M54 component includes a population of young, metal-rich stars. This finding is consistent with the MUSE spectroscopy of Alfaro-Cuello et al. (2019), who associate a young, metal-rich and spatially compact stellar population with M54, and supports the suggestion by Alfaro-Cuello et al. (2019) that these stars may have formed in response to the sinking of enriched gas into the center of a massive M54, perhaps triggered during Sgr's most recent pericentric passage of the Milky Way. Further exploration of this scenario in future work will require N-body simulations, which can be constrained by the results presented above.

Chapter 4

Conclusions

The small-scale problems have haunted the CDM theory for a long time. As the centre of the problems, dwarf galaxies have been studied many times. Dwarf galaxies have high mass-to-light ratios and low luminosities, which makes them particularly hard targets to observe. Dwarf galaxies are the most frequent type of galaxy in the universe, and one advantage is that we have a relatively rich amount of dwarf galaxies in the MW and Local Group. Their proximity allows for detailed observations of individual stars, and the improvement in sky surveys makes it possible to analyse these dwarf galaxies at an unprecedented precision level. However, measuring the distance to individual stars is still quite difficult, even for the dwarf galaxies around the MW, making it hard to infer the 3D shape and orientation of the dwarf galaxies. In addition to the difficulty in observations, modelling the distribution of stars in a complicated environment like the Sgr dSph is also very challenging because of the mixture of the multiple stellar components inside it and the contamination from the MW stars. In this work, we provide a method to infer the 3D shape and the orientation of the dwarf galaxies around the MW and then study the centre of the Sgr dSph and model the Sgr dSph and M54 simultaneously to infer the offset between them in the spatial, proper motion, and line-of-sight velocity space.

In Chapter 2, we use the BHB stars as the distance indicators to model the distance gradient of Bootes I, Draco, Ursa Minor, Sextans and Sculptor dwarf galaxies. We combine DECaLS DR8 photometry and *Gaia* photometry to cover as many dwarf galaxies around the MW as possible. We create an iterative procedure to find the colour-magnitude relation of BHB stars using the aggregated data from the multiple dwarf galaxies. We then use this relation to calculate the distance for each BHB star, and we use a mixture model based on the 2-D spatial distribution and the distance distribution to fit the distribution of BHB stars inside each dwarf separately. From the result of the distance gradient fitting, we use analytic formulas which connect the 3D shape to the distance gradient and 2D shape, and then we infer the posterior distribution of the parameters of the triaxial shape and the orientation. We find statistically significant non-zero gradients in both Sextans and Sculptor dwarf galaxies. The distance gradients in both dwarf galaxies are inconsistent with the prolate shape but compatible with the oblate or triaxial shapes. Assuming an oblate shape, Sextans and Sculptor need to have significant intrinsic ellipticities larger than 0.47 (Sextans) and 0.46 (Sculptor). The flattened shape may imply a significant anisotropy in the velocity distribution in order to be consistent with the lack of significant velocity gradients in these systems.

In Chapter 3, we study the centre of the Sgr dSph, where M54 resides. We construct a mixture model to model the Sgr and M54 simultaneously in the spatial and proper motion space using *Gaia* EDR3 data. We then take the MAP estimation from the previous modelling and use it in another mixture model for the line-of-sight velocity distribution using APOGEE DR17. We find a statistically significant offset between the spatial centres and the line-of-sight velocity space of the M54 and Sgr dSph. The offset between the spatial centres is 0.295 ± 0.029 degrees, corresponding to a projected (2D) offset of $0.135 \pm$

0.013 kpc at the distance of 26.28 kpc. The offset between the mean line-of-sight velocities is 4.1 ± 1.2 km s^{-1}. The offset between the PM centres of the M54 and the Sgr dSph is $[\Delta\mu_\alpha \cos\delta, \Delta\mu_\delta] = [0.0049, -0.0197] \pm [0.0068, 0.0062]$ mas yr^{-1}, with magnitude similar to the covariance expected due to spatially-correlated systematic error. We then sample sky positions, proper motions (including the systematic errors) and line-of-sight velocity from the posterior distributions of these models. Combined with other parameters from the literature, we calculate the possible orbits for the past 1 Gyr with considering the effect dynamical friction, both cuspy and cored dark matter profile, MW and LMC. The orbits are sensitive to the line-of-sight distance offset and the shape of the Sgr's dark matter profile. We find that if Sgr is embedded in a cuspy (NFW) dark matter halo, then the M54/Sgr orbit is currently most likely near an apocentric when the present-day offset is $\sim 0.13 - 0.7$ kpc (the lower limit is set by the 2D spatial offset we infer; the upper allows for different distances to M54 and Sgr), having decayed under dynamical friction from earlier apocentres $\gtrsim 1$ kpc. In contrast, if Sgr's dark matter halo has a central core, then the M54/Sgr orbit is possibly near pericentre currently when the present-day offset is $\sim 0.13 - 0.7$ kpc. Finally, if the present-day offset between M54 and Sgr is $\gtrsim 0.7$ kpc, which means it is dominated by an offset in the line-of-sight distance, then the calculated orbits would imply that M54 fell into Sgr within the past 200 Myr no matter whether it is cored or cuspy dark matter halo.

Our analysis of the distribution of each component in the colour-magnitude space using the MAP indicates that there are possibly two components in our M54 data: an old, metal-poor stellar component and a young, metal-rich stellar component. This finding is consistent with the MUSE spectroscopy of Alfaro-Cuello et al. (2019), who associate a young, metal-rich and spatially compact stellar population with M54, and supports the suggestion by Alfaro-Cuello et al. (2019) that these stars may have formed in response to the sinking of enriched gas into the centre of a massive M54, perhaps triggered during Sgr's most recent pericentric passage of the Milky Way.

There are multiple possible paths to continue our studies in the future. In the modelling of the shape of dwarf galaxies, we could consider the possibility of combining multiple distance indicators like RR Lyrae and red clump stars. However, this requires delicate analysis and modelling because of the different precisions and inhomogeneous distribution of the different stars. The combination of multiple different distance indicators will be a non-trivial task and will have great potential to improve the precision of the inferred 3D shape. With data with better precision, it is possible to use this method to model further galaxies and study the statistical behaviour of the shape and orientation of the galaxies. For example, we need the results of more galaxies to have a reliable distribution of the orientation of the galaxies, which can be used to compare with the predictions from the simulations (Kuhlen, Diemand, and Madau, 2007; Schneider, Frenk, and Cole, 2012). The distribution of the shape and the correlation of the orientation of the galaxies are also important in other studies, such as the study of weak gravitational lensing (Troxel and Ishak, 2015).

In our study of the Sgr and M54, one caveat is that we made several assumptions and simplifications in the orbit calculation. The globular cluster is modelled by a point mass, and the tidal disruption is ignored. A more realistic modelling is necessary to calculate the orbit for longer time. Due to the tidal disruption, the Sgr dSph has an asymmetric spatial distribution in the sky. We have considered a simple asymmetric model, but it fails to outperform the symmetric model in model selection. The most likely reason is that the model we construct does not properly capture the asymmetric features. A more realistic asymmetric model is required to improve the accuracy of the modelling. We also need the results from the N-body simulations to test whether the offset between the centres of the M54 and Sgr can help constrain some meaningful parameters. For example,

it may help to put the constraints on the origin of the M54 or the shape of the dark matter density profile inside the Sgr dSph. In our study, we build a model for the radial velocity distribution separately due to the data inhomogeneity issue. It will improve the accuracy of the modelling if we can model the sky position, proper motion and radial distance simultaneously, which requires the homogeneous observational data. It is also possible to bring the distance analysis in to get a 6-D analysis of the M54 and Sgr dSph. It is also possible to combine the two works together to build a multi-component model with 6-D analysis, which should be able to detect the complex structure inside the dwarf galaxies. Our analysis indicates that there is possibly an old, metal-poor stellar component and a young, metal-rich stellar component; however, we do not have any data at the centre of the M54, which means that we cannot detect any components if it lies only within the very central region. A more complete observational dataset of M54 is necessary for a more accurate modelling of this region and may reveal more substructures.

Appendix A

Appendix for Chapter 2

A.1 Masking of central regions

In Figure 2.1 we showed the distance modulus versus radial distance of Sculptor, which suggested the masking of stars within one half light radius. While this might seem reasonable for Sculptor based on this plot, it might not be suitable for other dwarfs. To further check how sensitive our results are to the masking radius, we run our distance gradient analysis with different masking radius. The distance gradient results are shown in Figure A.1. For most dwarfs, the change of the distance gradient distribution is small and negligible and our conclusion remains the same. The large change of Bootes I is due to the small number of BHB stars, so the masking of inner part will dramatically decrease the total number of BHB and leads to the large change in the posterior. And for Sculptor, we notice when we do not mask stars at all or only mask stars within a small radius, we do not have 3 sigma level significance of non-zero gradient, but when we remove with a radius no less than $0.6r_h$ we find the non-zero gradient is significant. Considering Figure 2.1 shows the Sculptor has large distance dispersion in the inner part, we think it is reasonable to mask the inner part, and our results are not too sensitive to the choice of the masking radius.

A.2 3-D Model Projection Code

First we define parameters for triaxial ellipsoid. Here we use Euler angles to parameterize rotation, the parameterization will be converted to axis-angle representation when we perform 3-D shape fitting.

```
Rx[a_]:=RotationMatrix[a, {1, 0, 0}]
Ry[b_]:=RotationMatrix[b, {0, 1, 0}]
Rz[c_]:=RotationMatrix[c, {0, 0, 1}]
B=DiagonalMatrix[{1/mx^2,1/my^2,1/mz^2}]
```

Then we integrate over z to get 2-D Plummer distribution. We will use m, n, p to represent the factors which are independent of z in integral. `EllipExpression` is quadratic function of x and y which is extracted from the result of previous integral, and it will be used for calculating the shape of 2-D distribution.

```
CoeffZ=CoefficientList[
    1+X.Transpose[Rx[a]].Transpose[Ry[b]].
    Transpose[Rz[c]].B.Rz[c].Ry[b].Rx[a].X, z]
Integrate[1/(m+n*z+p*z^2)^(5/2),
    {z, -\[Infinity], \[Infinity]}, Assumptions->
    m\[Element]Reals&&n\[Element]Reals&&
```

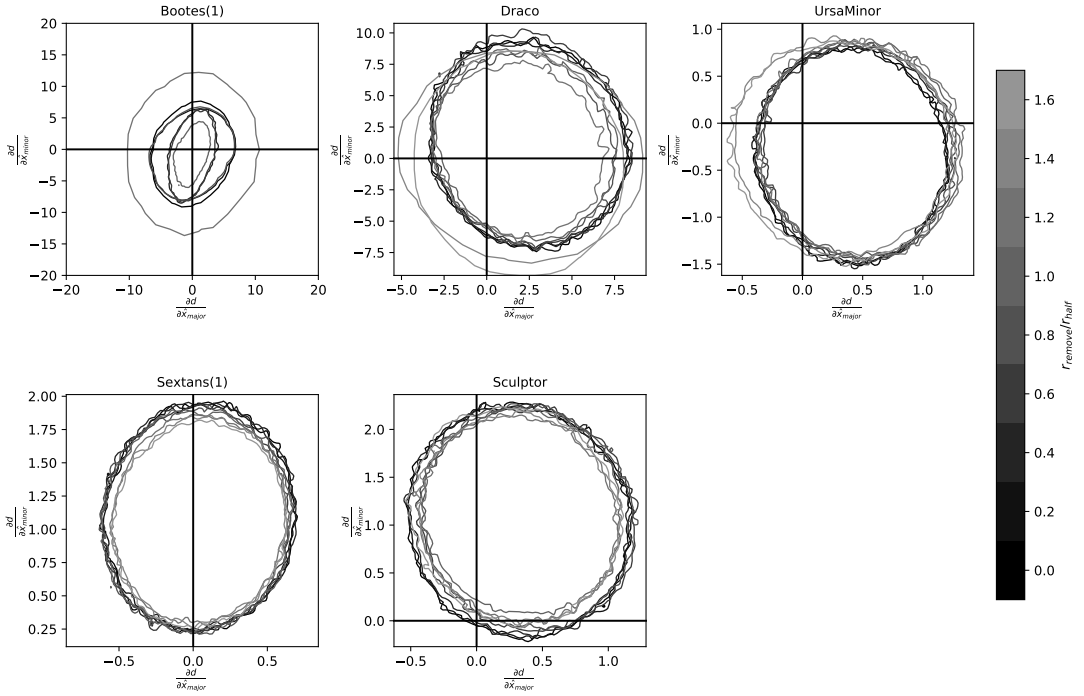

FIGURE A.1: The posterior of distance gradient with different masking radius. d is the distance in pc. $\hat{x}_{\rm major}$ and $\hat{x}_{\rm minor}$ are the coordinates aligned with the major/minor axes of each dwarf in pc. The zero gradient is marked by the dashed line. Each contour line represents a 3σ boundary of distance gradient posterior with a specific masking radius; the ratio of masking radius to half light radius is coded by the grayscale of the contour.

```
    p\[Element]Reals&&n^2-4 m p<0&&m>0
EllipExpression=n^2-4 m p/.{m->CoeffZ[[1]],
    n->CoeffZ[[2]], p->CoeffZ[[3]]}
```

Then we calculate position angle of semi-major axis vector and ratio of semi-major to semi-minor. The calculation is done by finding the eigenvalues and eigenvectors of the symmetric matrix of quadratic function of x, y. The values in `Evalues` are semi-minor and semi-major axis, and the corresponding column in the `Evectors` represents the vector along semi-minor/semi-major axis.

```
CoeffXY=CoefficientList[EllipExpression, {x, y}]
EllipCoefMatrix={{D1, D2/2}, {D2/2,D3}}
Evalues=Eigenvalues[EllipCoefMatrix]
Evectors=Eigenvectors[EllipCoefMatrix]
Evalues[[2]]/.{D1->CoeffXY[[3, 1]]/CoeffXY[[1, 1]],
    D2->CoeffXY[[2, 2]]/CoeffXY[[1, 1]],
    D3->CoeffXY[[1, 3]]/CoeffXY[[1, 1]]}
Evectors/.{D1->CoeffXY[[3, 1]]/CoeffXY[[1, 1]],
    D2->CoeffXY[[2, 2]]/CoeffXY[[1, 1]],
    D3->CoeffXY[[1, 3]]/CoeffXY[[1, 1]]}
```

A.3 Posterior Predictive Check

Here we perform the posterior predictive check for the 3-D model fitting of Sextans and Sculptor. We sample from the posterior of 3-D model, then use analytic formula in Appendix A.2 to calculate sample's $\hat{r}_{\rm major}, \hat{r}_{\rm minor}, \hat{\theta}_{\rm pos}, \hat{c}_x$ and $\hat{c}_y$ which we defined in Section 2.4.1, and compare the distribution of these parameters of samples with the same parameters of the data. Figure A.2 shows the posterior predictive check results for the triaxial model of Sculptor.

We can see that the peak of distribution of gradient along semi-major is between 1σ and 2σ boundary and a small part of the distribution of gradient along semi-minor is outside 1σ boundary. The model is still acceptable because the distribution is still within 3σ boundary. Considering the triaxial model should be very flexible and should have the ability to perfectly fit the data, we also calculate a maximum a posteriori (MAP) model shown by the red line in the Figure A.2 that also agrees well with data.

For the oblate model, Figure A.3 shows the result of posterior predictive check for Sculptor. The whole distribution of gradient along semi-major axis is outside 1σ boundary, and a small part of the distribution of gradient along semi-minor is outside 1σ boundary. We are not surprised about the distribution of gradient along semi-major axis are tightly constrained because an oblate should have zero gradient along semi-major as discussed in Section 2.4.1, and we can see that for oblate model, the MAP estimation cannot perfectly fit the data. This result is consistent with the distribution of triaxiality in the triaxial model fitting result, which shows zero triaxiality is possible but the triaxial model does not have a strong preference for oblate model.

Overall the result shows both the triaxial and the oblate models agree with the data of Sculptor. Based on posterior predictive check, we can accept the fitting results of both models.

We did the same analysis for Sextans and the posterior predictive check result is consistent with the data within 1σ, we will not show the detail here.

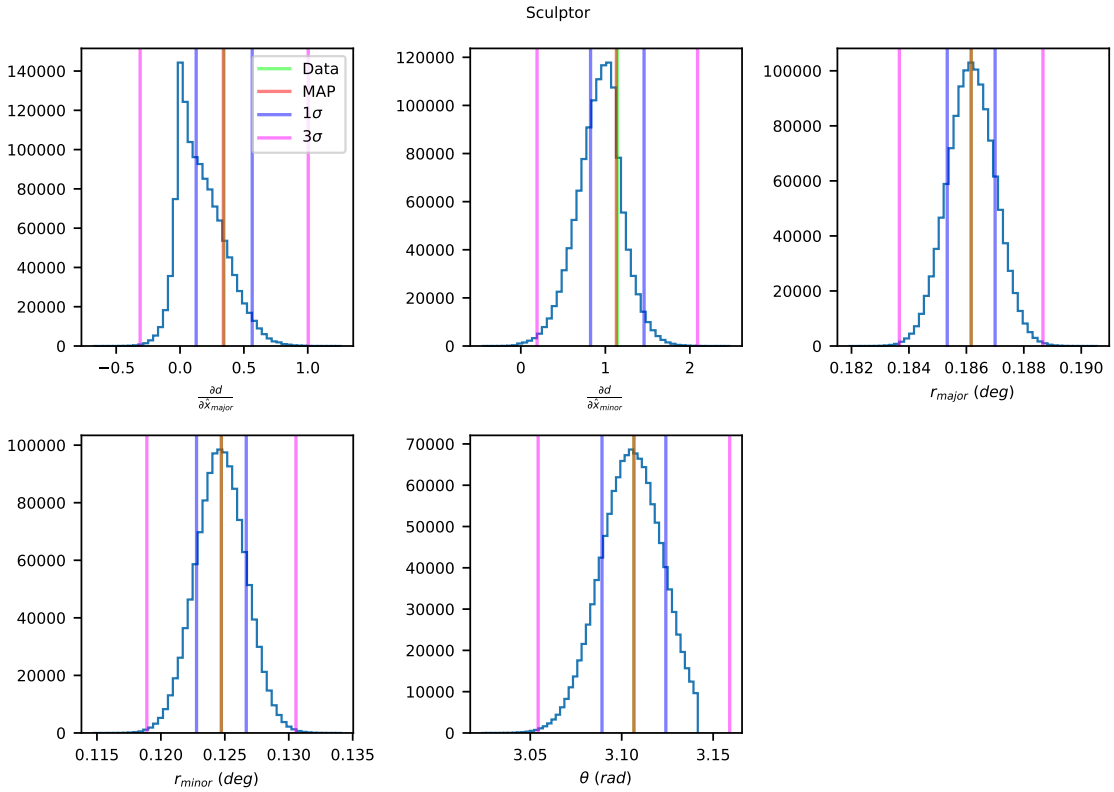

FIGURE A.2: The plots are marginal histograms of parameters inferred from the posterior of Sculptor triaxial ellipsoid model, where d is the distance in pc, $\hat{x}_{major}$ and $\hat{x}_{minor}$ is coordinate in semi-major/semi-minor coordinate system in pc, r_{major} is half-light radius along semi-major axis, r_{minor} is half-light radius along semi-minor axis for 2D Plummer and θ is position angle of major axis for 2D Plummer. The green lines show the values calculated from Sextans observed data, blue lines show their $1\,\sigma$ range and purple lines are $3\,\sigma$ range. The red line shows the parameters from the MAP for the triaxial ellipsoid model and is sitting on top of the green line.

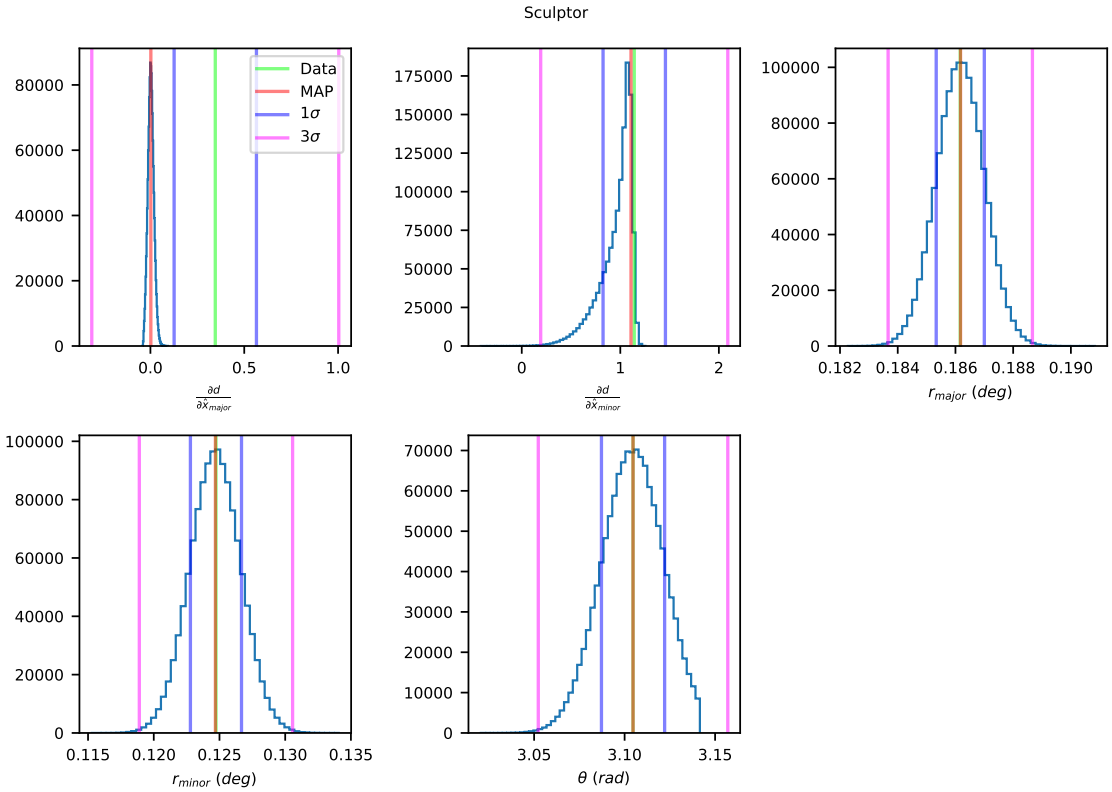

FIGURE A.3: The plots are marginal histograms of parameters inferred from the posterior of Sculptor oblate ellipsoid model, where d is the distance in pc, $\hat{x}_{major}$ and $\hat{x}_{minor}$ is coordinate in semi-major/semi-minor coordinate system in pc, r_{major} is half-light radius along semi-major axis, r_{minor} is half-light radius along semi-minor axis for 2D Plummer and θ is position angle of major axis for 2D Plummer. The green line is the value calculated from Sextans observed data, blue lines are 1σ boundary and purple lines are 3σ boundary. The red line is the result of MAP estimation for the oblate ellipsoid model.

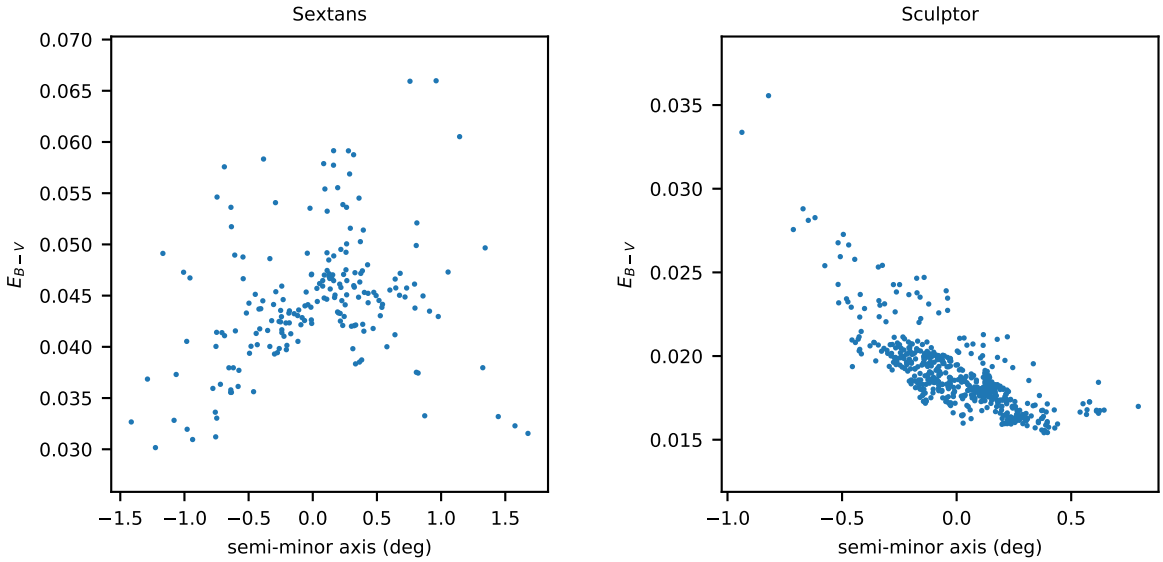

FIGURE A.4: The plots shows the relationship between BHB stars' E_{B-V} and their position along semi-minor axis in Sextans (left panel) and Sculptor (right panel), and the dots are BHBs we used in distance gradient fitting.

A.4 Extinction and Gradient

We notice that there is also E_{B-V} gradient in the Sextans and Sculptor. Figure A.4 shows the relationship between E_{B-V} and position along semi-minor axis for BHB stars in Sextans (left panel) and Sculptor (right panel). It's clear to see the gradient. To study how the changes E_{B-V} affect the distance gradient measurement, we scale E_{B-V} by different factors. Figure A.5 shows the result for Sextans, where to eliminate the observed gradient the extinction need to be scaled by almost 3.0. Figure A.6 shows the result for Sculptor, it shows that we need to scale E_{B-V} to zero to almost eliminate the distance gradient. These results show that it is extremely unlikely that the observed effects are caused by incorrect treatment of extinction. Even if there is a small change in extinction, that won't change the significance of our distance gradient measurement.

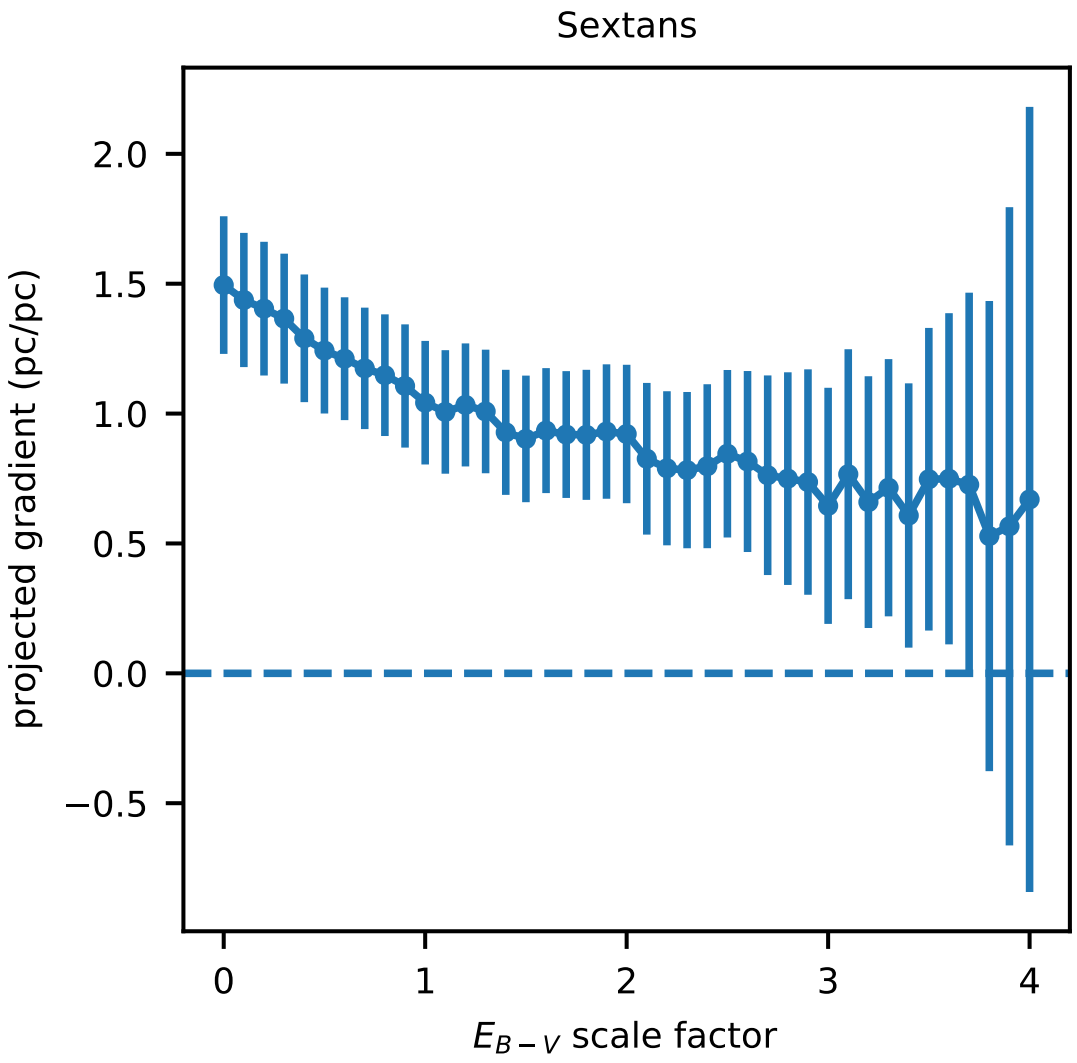

FIGURE A.5: The plot shows the Sextans's projected distance gradient (pc/pc) along the direction from zero gradient to average gradient that we obtain with different E_{B-V} scale factor. The errorbar is the standard deviation calculated after projection.

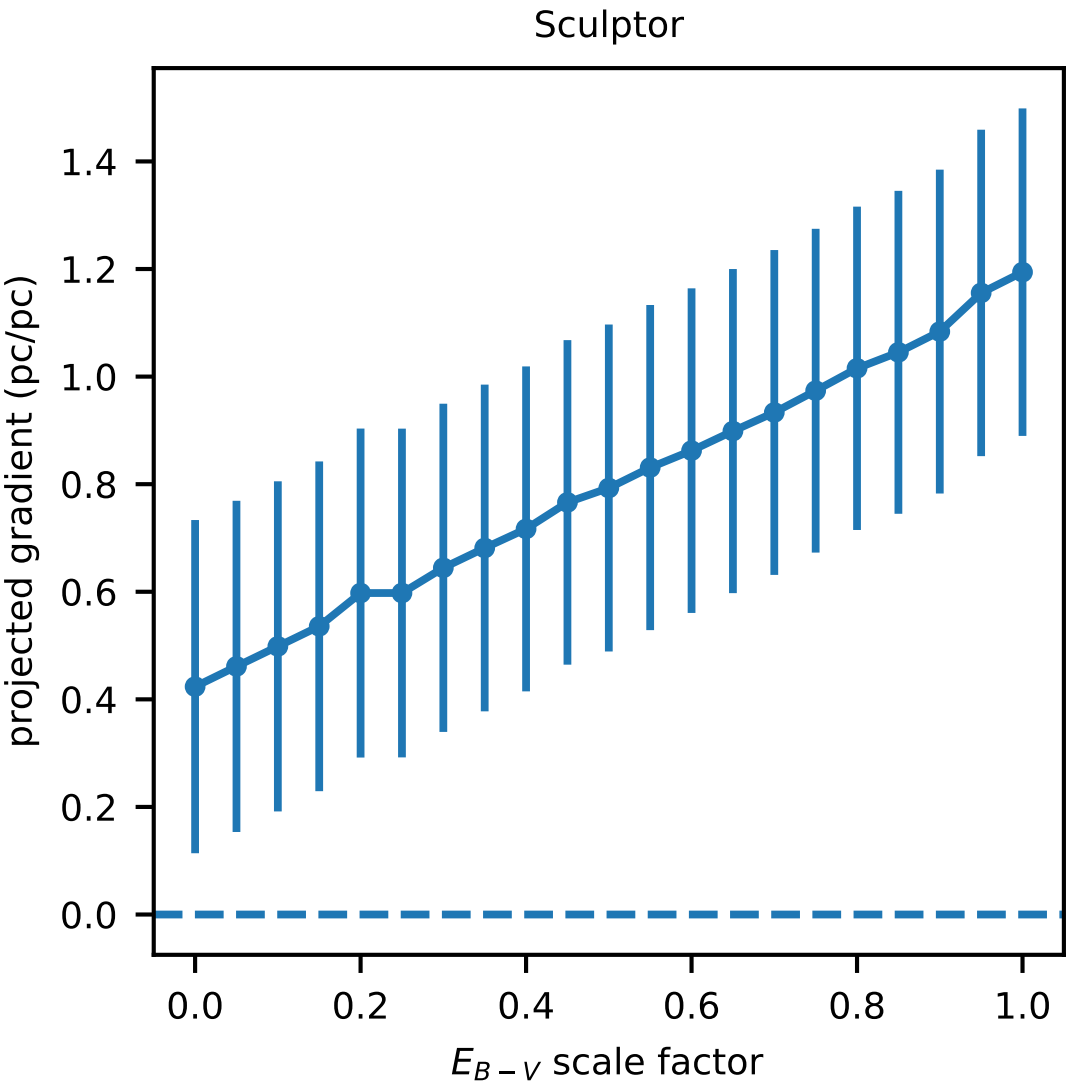

FIGURE A.6: The plot shows the Sculptor's projected distance gradient (pc/pc) along the direction from zero gradient to average gradient that we obtain with different E_{B-V} scale factor. The errorbar is the standard deviation calculated after projection.

Bibliography

Aaronson, M. (Mar. 1983). "Accurate radial velocities for carbon stars in Draco and Ursa Minor :the first hint of a dwarf spheroidal mass-to-light ratio." In: *The Astrophysical Journal* 266. ADS Bibcode: 1983ApJ...266L..11A, pp. L11–L15. ISSN: 0004-637X. DOI: 10.1086/183969. URL: https://ui.adsabs.harvard.edu/abs/1983ApJ...266L..11A (visited on 03/03/2024).

Abbott, T. M. C. et al. (2018). "The Dark Energy Survey Data Release 1". In: *The Astrophysical Journal Supplement Series* 239.2, p. 18. DOI: 10.3847/1538-4365/aae9f0. arXiv: 1801.03181. URL: http://arxiv.org/abs/1801.03181http://dx.doi.org/10.3847/1538-4365/aae9f0.

Abdurro'uf et al. (Apr. 2022). "The Seventeenth Data Release of the Sloan Digital Sky Surveys: Complete Release of MaNGA, MaStar, and APOGEE-2 Data". In: ApJS 259.2, 35, p. 35. DOI: 10.3847/1538-4365/ac4414. arXiv: 2112.02026 [astro-ph.GA].

Alfaro-Cuello, M. et al. (Nov. 2019). "A Deep View into the Nucleus of the Sagittarius Dwarf Spheroidal Galaxy with MUSE. I. Data and Stellar Population Characterization". In: ApJ 886.1, 57, p. 57. DOI: 10.3847/1538-4357/ab1b2c. arXiv: 1909.10529 [astro-ph.GA].

Alfaro-Cuello, M. et al. (Mar. 2020). "A Deep View into the Nucleus of the Sagittarius Dwarf Spheroidal Galaxy with MUSE. II. Kinematic Characterization of the Stellar Populations". In: ApJ 892.1, 20, p. 20. DOI: 10.3847/1538-4357/ab77bb. arXiv: 2002.07814 [astro-ph.GA].

An, Zhaozhou and Sergey E. Koposov (Apr. 2022). "Constraining the shape of Milky Way satellites with distance gradients". In: MNRAS 511.3, pp. 4316–4332. DOI: 10.1093/mnras/stac308. arXiv: 2203.02623 [astro-ph.GA].

Angus, G. W., B. Famaey, and H. S. Zhao (Sept. 2006). "Can MOND take a bullet? Analytical comparisons of three versions of MOND beyond spherical symmetry". In: MNRAS 371.1, pp. 138–146. DOI: 10.1111/j.1365-2966.2006.10668.x. arXiv: astro-ph/0606216 [astro-ph].

Antonini, Fabio, Enrico Barausse, and Joseph Silk (Oct. 2015). "The Coevolution of Nuclear Star Clusters, Massive Black Holes, and Their Host Galaxies". In: ApJ 812.1, 72, p. 72. DOI: 10.1088/0004-637X/812/1/72. arXiv: 1506.02050 [astro-ph.GA].

Arca-Sedda, M. and R. Capuzzo-Dolcetta (Nov. 2014). "The globular cluster migratory origin of nuclear star clusters". In: MNRAS 444.4, pp. 3738–3755. DOI: 10.1093/mnras/stu1683. arXiv: 1405.7593 [astro-ph.GA].

Bailin, Jeremy and Matthias Steinmetz (July 2005). "Internal and External Alignment of the Shapes and Angular Momenta of ΛCDM Halos". In: ApJ 627.2, pp. 647–665. DOI: 10.1086/430397. arXiv: astro-ph/0408163 [astro-ph].

Baldassare, Vivienne F. et al. (Aug. 2014). "AMUSE-Field. II. Nucleation of Early-type Galaxies in the Field versus Cluster Environment". In: ApJ 791.2, 133, p. 133. DOI: 10.1088/0004-637X/791/2/133. arXiv: 1406.6697 [astro-ph.GA].

Baldry, I. K. et al. (Mar. 2012). "Galaxy And Mass Assembly (GAMA): the galaxy stellar mass function at z < 0.06". In: MNRAS 421.1, pp. 621–634. DOI: 10.1111/j.1365-2966.2012.20340.x. arXiv: 1111.5707 [astro-ph.CO].

Banik, Uddipan and Frank C. van den Bosch (Feb. 2022). "Dynamical Friction, Buoyancy, and Core-stalling. I. A Nonperturbative Orbit-based Analysis". In: ApJ 926.2, 215, p. 215. DOI: 10.3847/1538-4357/ac4242. arXiv: 2112.06944 [astro-ph.GA].

Barber, Christopher et al. (Feb. 2015). "Galactic tides and the shape and orientation of dwarf galaxy satellites". In: MNRAS 447.2, pp. 1112–1125. DOI: 10.1093/mnras/stu2494. arXiv: 1410.6161 [astro-ph.GA].

Battaglia, G. et al. (July 2008). "The Kinematic Status and Mass Content of the Sculptor Dwarf Spheroidal Galaxy". In: ApJ 681.1, p. L13. DOI: 10.1086/590179. arXiv: 0802.4220 [astro-ph].

Battaglia, G. et al. (Feb. 2011). "Study of the Sextans dwarf spheroidal galaxy from the DART Ca II triplet survey". In: MNRAS 411.2, pp. 1013–1034. DOI: 10.1111/j.1365-2966.2010.17745.x. arXiv: 1009.4857 [astro-ph.CO].

Baumgardt, H. and M. Hilker (Aug. 2018). "A catalogue of masses, structural parameters, and velocity dispersion profiles of 112 Milky Way globular clusters". In: MNRAS 478.2, pp. 1520–1557. DOI: 10.1093/mnras/sty1057. arXiv: 1804.08359 [astro-ph.GA].

Baumgardt, H. and E. Vasiliev (Aug. 2021). "Accurate distances to Galactic globular clusters through a combination of Gaia EDR3, HST, and literature data". In: MNRAS 505.4, pp. 5957–5977. DOI: 10.1093/mnras/stab1474. arXiv: 2105.09526 [astro-ph.GA].

Bekki, K. (July 2007). "The Formation of Stellar Galactic Nuclei through Dissipative Gas Dynamics". In: PASA 24.2, pp. 77–94. DOI: 10.1071/AS07008.

Bekki, Kenji, Warrick J. Couch, and Yasuhiro Shioya (May 2006). "Dissipative Transformation of Nonnucleated Dwarf Galaxies into Nucleated Systems". In: ApJ 642.2, pp. L133–L136. DOI: 10.1086/504588. arXiv: astro-ph/0604340 [astro-ph].

Bellazzini, M., F. R. Ferraro, and E. Pancino (Oct. 2001). "Multiple stellar populations in the Sextans dwarf spheroidal galaxy?" In: MNRAS 327.1, pp. L15–L20. DOI: 10.1046/j.1365-8711.2001.04889.x. arXiv: astro-ph/0108504 [astro-ph].

Bellazzini, M. et al. (Sept. 2008). "The Nucleus of the Sagittarius Dsph Galaxy and M54: a Window on the Process of Galaxy Nucleation". In: *The Astronomical Journal* 136. ADS Bibcode: 2008AJ....136.1147B, pp. 1147–1170. ISSN: 0004-6256. DOI: 10.1088/0004-6256/136/3/1147. URL: https://ui.adsabs.harvard.edu/abs/2008AJ....136.1147B (visited on 04/16/2023).

Belokurov, V. et al. (May 2006). "The Field of Streams: Sagittarius and Its Siblings". In: ApJ 642.2, pp. L137–L140. DOI: 10.1086/504797. arXiv: astro-ph/0605025 [astro-ph].

Belokurov, V. et al. (Oct. 2008). "Leo V: A Companion of a Companion of the Milky Way Galaxy?" In: ApJ 686.2, p. L83. DOI: 10.1086/592962. arXiv: 0807.2831 [astro-ph].

Bender, Ralf et al. (Sept. 2005). "HST STIS Spectroscopy of the Triple Nucleus of M31: Two Nested Disks in Keplerian Rotation around a Supermassive Black Hole". en. In: *The Astrophysical Journal* 631.1. Publisher: IOP Publishing, p. 280. ISSN: 0004-637X. DOI: 10.1086/432434. URL: https://iopscience.iop.org/article/10.1086/432434/meta (visited on 04/23/2023).

Benítez-Llambay, Alejandro et al. (Sept. 2019). "Baryon-induced dark matter cores in the EAGLE simulations". In: MNRAS 488.2, pp. 2387–2404. DOI: 10.1093/mnras/stz1890. arXiv: 1810.04186 [astro-ph.GA].

Bernardi, M. et al. (Nov. 2013). "The massive end of the luminosity and stellar mass functions: dependence on the fit to the light profile". In: MNRAS 436.1, pp. 697–704. DOI: 10.1093/mnras/stt1607. arXiv: 1304.7778 [astro-ph.CO].

Bertin, E. (July 2011). "Automated Morphometry with SExtractor and PSFEx". In: *Astronomical Data Analysis Software and Systems XX*. Ed. by I. N. Evans et al. Vol. 442. Astronomical Society of the Pacific Conference Series, p. 435.

Bertin, E. and S. Arnouts (June 1996). "SExtractor: Software for source extraction." In: A&AS 117, pp. 393–404. DOI: 10.1051/aas:1996164.

Binggeli, B., F. Barazza, and H. Jerjen (July 2000). "Off-center nuclei in dwarf elliptical galaxies". In: *Astronomy and Astrophysics* 359. ADS Bibcode: 2000A&A...359..447B, pp. 447–456. ISSN: 0004-6361. URL: https://ui.adsabs.harvard.edu/abs/2000A&A...359..447B (visited on 05/04/2023).

Binney, J. (Oct. 1976). "Is the flattening of elliptical galaxies necessarily due to rotation?" In: MNRAS 177, pp. 19–29. DOI: 10.1093/mnras/177.1.19.

— (May 1978). "On the rotation of elliptical galaxies." In: MNRAS 183, pp. 501–514. DOI: 10.1093/mnras/183.3.501.

Binney, James (Nov. 2005). "Rotation and anisotropy of galaxies revisited". In: MNRAS 363.3, pp. 937–942. DOI: 10.1111/j.1365-2966.2005.09495.x. arXiv: astro-ph/0504387 [astro-ph].

Blok, W. J. G. de et al. (Nov. 2008). "HIGH-RESOLUTION ROTATION CURVES AND GALAXY MASS MODELS FROM THINGS". en. In: *The Astronomical Journal* 136.6. Publisher: The American Astronomical Society, p. 2648. ISSN: 1538-3881. DOI: 10.1088/0004-6256/136/6/2648. URL: https://dx.doi.org/10.1088/0004-6256/136/6/2648 (visited on 03/03/2024).

Bode, Paul, Jeremiah P. Ostriker, and Neil Turok (July 2001). "Halo Formation in Warm Dark Matter Models". In: ApJ 556.1, pp. 93–107. DOI: 10.1086/321541. arXiv: astro-ph/0010389 [astro-ph].

Bond, J. R. and A. S. Szalay (Nov. 1983). "The collisionless damping of density fluctuations in an expanding universe". In: ApJ 274, pp. 443–468. DOI: 10.1086/161460.

Bose, Sownak et al. (July 2019). "No cores in dark matter-dominated dwarf galaxies with bursty star formation histories". In: *Monthly Notices of the Royal Astronomical Society* 486. ADS Bibcode: 2019MNRAS.486.4790B, pp. 4790–4804. ISSN: 0035-8711. DOI: 10.1093/mnras/stz1168. URL: https://ui.adsabs.harvard.edu/abs/2019MNRAS.486.4790B (visited on 03/07/2024).

Bovy, Jo (Feb. 2015). "galpy: A python Library for Galactic Dynamics". In: ApJS 216.2, 29, p. 29. DOI: 10.1088/0067-0049/216/2/29. arXiv: 1412.3451 [astro-ph.GA].

Boyarsky, A. et al. (Jan. 2019). "Sterile neutrino Dark Matter". In: *Progress in Particle and Nuclear Physics* 104. ADS Bibcode: 2019PrPNP.104....1B, pp. 1–45. ISSN: 0146-6410. DOI: 10.1016/j.ppnp.2018.07.004. URL: https://ui.adsabs.harvard.edu/abs/2019PrPNP.104....1B (visited on 03/11/2024).

Boylan-Kolchin, Michael, James S. Bullock, and Manoj Kaplinghat (July 2011). "Too big to fail? The puzzling darkness of massive Milky Way subhaloes". In: *Monthly Notices of the Royal Astronomical Society* 415. ADS Bibcode: 2011MNRAS.415L..40B, pp. L40–L44. ISSN: 0035-8711. DOI: 10.1111/j.1745-3933.2011.01074.x. URL: https://ui.adsabs.harvard.edu/abs/2011MNRAS.415L..40B (visited on 03/03/2024).

Boylan-Kolchin, Michael, James S. Bullock, and Manoj Kaplinghat (July 2011). "Too big to fail? The puzzling darkness of massive Milky Way subhaloes". In: MNRAS 415.1, pp. L40–L44. DOI: 10.1111/j.1745-3933.2011.01074.x. arXiv: 1103.0007 [astro-ph.CO].

— (May 2012). "The Milky Way's bright satellites as an apparent failure of ΛCDM". In: MNRAS 422.2, pp. 1203–1218. DOI: 10.1111/j.1365-2966.2012.20695.x. arXiv: 1111.2048 [astro-ph.CO].

Brok, Mark den et al. (Dec. 2014). "The HST/ACS Coma Cluster Survey – X. Nuclear star clusters in low-mass early-type galaxies: scaling relations". In: *Monthly Notices of the Royal Astronomical Society* 445.3, pp. 2385–2403. ISSN: 0035-8711. DOI: 10.1093/mnras/stu1906. URL: https://doi.org/10.1093/mnras/stu1906 (visited on 04/24/2023).

Brook, Chris B. (Dec. 2015). "The variation of rotation curve shapes as a signature of the effects of baryons on dark matter density profiles". In: *Monthly Notices of the Royal Astronomical Society* 454. ADS Bibcode: 2015MNRAS.454.1719B, pp. 1719–1724. ISSN:

0035-8711. DOI: 10.1093/mnras/stv2101. URL: https://ui.adsabs.harvard.edu/abs/2015MNRAS.454.1719B (visited on 03/09/2024).

Buckley, Matthew R. and Annika H. G. Peter (Oct. 2018). "Gravitational probes of dark matter physics". In: Phys. Rep. 761, pp. 1–60. DOI: 10.1016/j.physrep.2018.07.003. arXiv: 1712.06615 [astro-ph.CO].

Bullock, James S. and Michael Boylan-Kolchin (Aug. 2017). "Small-Scale Challenges to the ΛCDM Paradigm". In: ARA&A 55.1, pp. 343–387. DOI: 10.1146/annurev-astro-091916-055313. arXiv: 1707.04256 [astro-ph.CO].

Bullock, James S. and Michael Boylan-Kolchin (2017). "Small-Scale Challenges to the ΛCDM Paradigm". In: *Annual Review of Astronomy and Astrophysics* 55.1, pp. 343–387. DOI: 10.1146/annurev-astro-091916-055313. arXiv: 1707.04256. URL: http://arxiv.org/abs/1707.04256http://dx.doi.org/10.1146/annurev-astro-091916-055313.

Burles, Scott, Kenneth M. Nollett, and Michael S. Turner (Apr. 2001). "Big Bang Nucleosynthesis Predictions for Precision Cosmology". en. In: *The Astrophysical Journal* 552.1. Publisher: IOP Publishing, p. L1. ISSN: 0004-637X. DOI: 10.1086/320251. URL: https://iopscience.iop.org/article/10.1086/320251/meta (visited on 02/22/2024).

Callingham, Thomas M. et al. (Apr. 2019). "The mass of the Milky Way from satellite dynamics". In: *Monthly Notices of the Royal Astronomical Society* 484. ADS Bibcode: 2019MNRAS.484.5453C, pp. 5453–5467. ISSN: 0035-8711. DOI: 10.1093/mnras/stz365. URL: https://ui.adsabs.harvard.edu/abs/2019MNRAS.484.5453C (visited on 03/09/2024).

Callingham, Thomas M. et al. (Apr. 2019). "The mass of the Milky Way from satellite dynamics". In: MNRAS 484.4, pp. 5453–5467. DOI: 10.1093/mnras/stz365. arXiv: 1808.10456 [astro-ph.GA].

Campbell, David J. R. et al. (Aug. 2017). "Knowing the unknowns: uncertainties in simple estimators of galactic dynamical masses". In: *Monthly Notices of the Royal Astronomical Society* 469. ADS Bibcode: 2017MNRAS.469.2335C, pp. 2335–2360. ISSN: 0035-8711. DOI: 10.1093/mnras/stx975. URL: https://ui.adsabs.harvard.edu/abs/2017MNRAS.469.2335C (visited on 03/09/2024).

Cappellari, Michele et al. (Mar. 2006). "The SAURON project - IV. The mass-to-light ratio, the virial mass estimator and the Fundamental Plane of elliptical and lenticular galaxies". In: MNRAS 366.4, pp. 1126–1150. DOI: 10.1111/j.1365-2966.2005.09981.x. arXiv: astro-ph/0505042 [astro-ph].

Capuzzo-Dolcetta, R. and A. Mastrobuono-Battisti (Nov. 2009). "Globular cluster system erosion in elliptical galaxies". In: *Astronomy and Astrophysics* 507. ADS Bibcode: 2009A&A...507..183C, pp. 183–193. ISSN: 0004-6361. DOI: 10.1051/0004-6361/200912255. URL: https://ui.adsabs.harvard.edu/abs/2009A&A...507..183C (visited on 04/24/2023).

Capuzzo-Dolcetta, Roberto (Oct. 1993). "The Evolution of the Globular Cluster System in a Triaxial Galaxy: Can a Galactic Nucleus Form by Globular Cluster Capture?" In: ApJ 415, p. 616. DOI: 10.1086/173189. arXiv: astro-ph/9301006 [astro-ph].

Carlson, Eric D., Marie E. Machacek, and Lawrence J. Hall (Oct. 1992). "Self-interacting Dark Matter". In: ApJ 398, p. 43. DOI: 10.1086/171833.

Carlsten, Scott G. et al. (Oct. 2020). "Radial Distributions of Dwarf Satellite Systems in the Local Volume". In: ApJ 902.2, 124, p. 124. DOI: 10.3847/1538-4357/abb60b. arXiv: 2006.02444 [astro-ph.GA].

Carretta, E. et al. (Sept. 2010). "Detailed abundances of a large sample of giant stars in M 54 and in the Sagittarius nucleus". In: A&A 520, A95, A95. DOI: 10.1051/0004-6361/201014924. arXiv: 1006.5866 [astro-ph.GA].

Chan, T. K. et al. (Dec. 2015). "The impact of baryonic physics on the structure of dark matter haloes: the view from the FIRE cosmological simulations". In: MNRAS 454.3, pp. 2981–3001. DOI: 10.1093/mnras/stv2165. arXiv: 1507.02282 [astro-ph.GA].

Cicuéndez, L. and G. Battaglia (Oct. 2018). "Appearances can be deceiving: clear signs of accretion in the seemingly ordinary Sextans dSph". In: MNRAS 480.1, pp. 251–260. DOI: 10.1093/mnras/sty1748. arXiv: 1804.02336 [astro-ph.GA].

Cicuéndez, L. et al. (Jan. 2018). "Tracing the stellar component of low surface brightness Milky Way dwarf galaxies to their outskirts. I. Sextans". In: A&A 609, A53, A53. DOI: 10.1051/0004-6361/201731450. arXiv: 1709.04519 [astro-ph.GA].

Clewley, L. et al. (Nov. 2002). "Distant field blue horizontal branch stars and the mass of the Galaxy - I. Classification of halo A-type stars". In: MNRAS 337.1, pp. 87–97. DOI: 10.1046/j.1365-8711.2002.05864.x. arXiv: astro-ph/0207499 [astro-ph].

Clowe, Douglas et al. (Sept. 2006). "A Direct Empirical Proof of the Existence of Dark Matter". In: ApJ 648.2, pp. L109–L113. DOI: 10.1086/508162. arXiv: astro-ph/0608407 [astro-ph].

Cole, David R. et al. (Oct. 2012). "The mass distribution of the Fornax dSph: constraints from its globular cluster distribution". In: MNRAS 426.1, pp. 601–613. DOI: 10.1111/j.1365-2966.2012.21885.x. arXiv: 1205.6327 [astro-ph.CO].

Coleman, M. G., G. S. Da Costa, and Joss Bland-Hawthorn (Sept. 2005). "The Absence of Extratidal Structure in the Sculptor Dwarf Spheroidal Galaxy". In: AJ 130.3, pp. 1065–1082. DOI: 10.1086/432662. arXiv: astro-ph/0506069 [astro-ph].

Cooper, A. P. et al. (Aug. 2010). "Galactic stellar haloes in the CDM model". In: MNRAS 406.2, pp. 744–766. DOI: 10.1111/j.1365-2966.2010.16740.x. arXiv: 0910.3211 [astro-ph.GA].

Crnojević, D. et al. (June 2016). "Deep Imaging of Eridanus II and Its Lone Star Cluster". In: ApJ 824.1, L14, p. L14. DOI: 10.3847/2041-8205/824/1/L14. arXiv: 1604.08590 [astro-ph.GA].

Côté, Patrick et al. (July 2006). "The ACS Virgo Cluster Survey. VIII. The Nuclei of Early-Type Galaxies*". en. In: *The Astrophysical Journal Supplement Series* 165.1. Publisher: IOP Publishing, p. 57. ISSN: 0067-0049. DOI: 10.1086/504042. URL: https://iopscience.iop.org/article/10.1086/504042/meta (visited on 04/23/2023).

Davis, M. et al. (May 1985). "The evolution of large-scale structure in a universe dominated by cold dark matter". In: ApJ 292, pp. 371–394. DOI: 10.1086/163168.

de Boer, T. J. L. et al. (Apr. 2011). "Deep wide-field imaging down to the oldest main sequence turn-offs in the Sculptor dwarf spheroidal galaxy". In: A&A 528, A119, A119. DOI: 10.1051/0004-6361/201016398. arXiv: 1103.0015 [astro-ph.CO].

De Rijcke, Sven and Victor P. Debattista (Mar. 2004). "The Counterstreaming Instability in Dwarf Elliptical Galaxies with Off-Center Nuclei". In: ApJ 603.1, pp. L25–L28. DOI: 10.1086/383088. arXiv: astro-ph/0404041 [astro-ph].

Deason, A. J., V. Belokurov, and N. W. Evans (2011). "The Milky Way stellar halo out to 40kpc: Squashed, broken but smooth". In: *Monthly Notices of the Royal Astronomical Society* 416.4, pp. 2903–2915. ISSN: 00358711. DOI: 10.1111/j.1365-2966.2011.19237.x. arXiv: 1104.3220. URL: https://academic.oup.com/mnras/article/416/4/2903/976085.

Deason, A. J. et al. (Aug. 2011). "Mismatch and misalignment: dark haloes and satellites of disc galaxies". In: MNRAS 415.3, pp. 2607–2625. DOI: 10.1111/j.1365-2966.2011.18884.x. arXiv: 1101.0816 [astro-ph.CO].

Dekel, A. and J. Silk (Apr. 1986). "The Origin of Dwarf Galaxies, Cold Dark Matter, and Biased Galaxy Formation". In: ApJ 303, p. 39. DOI: 10.1086/164050.

del Pino, Andrés et al. (Feb. 2021). "Revealing the Structure and Internal Rotation of the Sagittarius Dwarf Spheroidal Galaxy with Gaia and Machine Learning". In: ApJ 908.2, 244, p. 244. DOI: 10.3847/1538-4357/abd5bf. arXiv: 2011.02627 [astro-ph.GA].

Dellenbusch, Kate E. et al. (Jan. 2008). "Deep Optical Imaging of Starbursting "Transition" Dwarf Galaxies". In: AJ 135.1, pp. 326–332. DOI: 10.1088/0004-6256/135/1/326. arXiv: 0710.4094 [astro-ph].

Dey, Arjun et al. (May 2019). "Overview of the DESI Legacy Imaging Surveys". In: AJ 157.5, 168, p. 168. DOI: 10.3847/1538-3881/ab089d. arXiv: 1804.08657 [astro-ph.IM].

Do, Tuan et al. (Aug. 2015). "Discovery of Low-metallicity Stars in the Central Parsec of the Milky Way". In: ApJ 809.2, 143, p. 143. DOI: 10.1088/0004-637X/809/2/143. arXiv: 1506.07891 [astro-ph.GA].

Dotter, Aaron et al. (Sept. 2008). "The Dartmouth Stellar Evolution Database". In: ApJS 178.1, pp. 89–101. DOI: 10.1086/589654. arXiv: 0804.4473 [astro-ph].

Drlica-Wagner, A. et al. (Apr. 2018). "Dark Energy Survey Year 1 Results: The Photometric Data Set for Cosmology". In: ApJS 235.2, 33, p. 33. DOI: 10.3847/1538-4365/aab4f5. arXiv: 1708.01531 [astro-ph.CO].

Efstathiou, G., J. R. Bond, and S. D. M. White (Sept. 1992). "COBE background radiation anisotropies and large-scale structure in the universe". In: MNRAS 258.1, 1P–6P. DOI: 10.1093/mnras/258.1.1P.

Einasto, J. (Jan. 1965). "On the Construction of a Composite Model for the Galaxy and on the Determination of the System of Galactic Parameters". In: *Trudy Astrofizicheskogo Instituta Alma-Ata* 5, pp. 87–100.

Einasto, Jaan, Ants Kaasik, and Enn Saar (July 1974). "Dynamic evidence on massive coronas of galaxies". en. In: *Nature* 250.5464. Number: 5464 Publisher: Nature Publishing Group, pp. 309–310. ISSN: 1476-4687. DOI: 10.1038/250309a0. URL: https://www.nature.com/articles/250309a0 (visited on 02/19/2024).

El-Badry, Kareem et al. (Feb. 2017). "When the Jeans Do Not Fit: How Stellar Feedback Drives Stellar Kinematics and Complicates Dynamical Modeling in Low-mass Galaxies". In: ApJ 835.2, 193, p. 193. DOI: 10.3847/1538-4357/835/2/193. arXiv: 1610.04232 [astro-ph.GA].

El-Zant, Amr, Isaac Shlosman, and Yehuda Hoffman (Oct. 2001). "Dark Halos: The Flattening of the Density Cusp by Dynamical Friction". In: ApJ 560.2, pp. 636–643. DOI: 10.1086/322516. arXiv: astro-ph/0103386 [astro-ph].

Emsellem, Eric et al. (Aug. 2007). "The SAURON project - IX. A kinematic classification for early-type galaxies". In: MNRAS 379.2, pp. 401–417. DOI: 10.1111/j.1365-2966.2007.11752.x. arXiv: astro-ph/0703531 [astro-ph].

Emsellem, Eric et al. (2011). "The ATLAS3D project - III. A census of the stellar angular momentum within the effective radius of early-type galaxies: Unveiling the distribution of fast and slow rotators". In: *Monthly Notices of the Royal Astronomical Society* 414.2, pp. 888–912. ISSN: 00358711. DOI: 10.1111/j.1365-2966.2011.18496.x. arXiv: 1102.4444. URL: https://academic.oup.com/mnras/article/414/2/888/976034.

Erkal, D. et al. (Aug. 2019). "The total mass of the Large Magellanic Cloud from its perturbation on the Orphan stream". In: MNRAS 487.2, pp. 2685–2700. DOI: 10.1093/mnras/stz1371. arXiv: 1812.08192 [astro-ph.GA].

Errani, Raphaël, Jorge Peñarrubia, and Matthew G. Walker (Dec. 2018). "Systematics in virial mass estimators for pressure-supported systems". In: MNRAS 481.4, pp. 5073–5090. DOI: 10.1093/mnras/sty2505. arXiv: 1805.00484 [astro-ph.GA].

Errani, Raphaël, Jorge Peñarrubia, and Matthew G. Walker (Dec. 2018). "Systematics in virial mass estimators for pressure-supported systems". In: *Monthly Notices of the Royal Astronomical Society* 481. ADS Bibcode: 2018MNRAS.481.5073E, pp. 5073–5090.

ISSN: 0035-8711. DOI: 10.1093/mnras/sty2505. URL: https://ui.adsabs.harvard.edu/abs/2018MNRAS.481.5073E (visited on 03/09/2024).

The HIPPARCOS and TYCHO catalogues. Astrometric and photometric star catalogues derived from the ESA HIPPARCOS Space Astrometry Mission (Jan. 1997). Vol. 1200. ESA Special Publication.

Evans, D. W. et al. (2018). "Gaia Data Release 2: Photometric content and validation". In: *Astronomy and Astrophysics* 616, A4. ISSN: 14320746. DOI: 10.1051/0004-6361/201832756. arXiv: 1804.09368. URL: https://doi.org/10.1051/0004-6361/201832756.

Faber, S. M. and D. N. C. Lin (Mar. 1983). "Is there nonluminous matter in dwarf spheroidal galaxies ?" In: *The Astrophysical Journal* 266. ADS Bibcode: 1983ApJ...266L..17F, pp. L17–L20. ISSN: 0004-637X. DOI: 10.1086/183970. URL: https://ui.adsabs.harvard.edu/abs/1983ApJ...266L..17F (visited on 03/03/2024).

Faulkner, J. and Jr. Iben Icko (June 1966). "The Evolution of Population II Stars". In: ApJ 144, p. 995. DOI: 10.1086/148697.

Fermani, Francesco and Ralph Schönrich (Apr. 2013). "A new calibration for the Blue Horizontal Branch". In: MNRAS 430.2, pp. 1294–1301. DOI: 10.1093/mnras/sts703. arXiv: 1301.1974 [astro-ph.GA].

Feroz, F., M. P. Hobson, and M. Bridges (Oct. 2009). "MULTINEST: an efficient and robust Bayesian inference tool for cosmology and particle physics". In: MNRAS 398.4, pp. 1601–1614. DOI: 10.1111/j.1365-2966.2009.14548.x. arXiv: 0809.3437 [astro-ph].

Ferrara, Andrea and Eline Tolstoy (Apr. 2000). "The role of stellar feedback and dark matter in the evolution of dwarf galaxies". In: *Monthly Notices of the Royal Astronomical Society* 313. ADS Bibcode: 2000MNRAS.313..291F, pp. 291–309. ISSN: 0035-8711. DOI: 10.1046/j.1365-8711.2000.03209.x. URL: https://ui.adsabs.harvard.edu/abs/2000MNRAS.313..291F (visited on 03/10/2024).

Fitts, Alex et al. (Nov. 2017). "fire in the field: simulating the threshold of galaxy formation". In: MNRAS 471.3, pp. 3547–3562. DOI: 10.1093/mnras/stx1757. arXiv: 1611.02281 [astro-ph.GA].

Flaugher, B. et al. (Nov. 2015). "The Dark Energy Camera". In: AJ 150.5, 150, p. 150. DOI: 10.1088/0004-6256/150/5/150. arXiv: 1504.02900 [astro-ph.IM].

Flores, Ricardo A. and Joel R. Primack (May 1994). "Observational and Theoretical Constraints on Singular Dark Matter Halos". In: *The Astrophysical Journal* 427. ADS Bibcode: 1994ApJ...427L...1F, p. L1. ISSN: 0004-637X. DOI: 10.1086/187350. URL: https://ui.adsabs.harvard.edu/abs/1994ApJ...427L...1F (visited on 03/03/2024).

Flores, Ricardo A. and Joel R. Primack (May 1994). "Observational and Theoretical Constraints on Singular Dark Matter Halos". In: ApJ 427, p. L1. DOI: 10.1086/187350. arXiv: astro-ph/9402004 [astro-ph].

Foreman-Mackey, D. et al. (2013). "emcee: The MCMC Hammer". In: *PASP* 125, pp. 306–312. DOI: 10.1086/670067. eprint: 1202.3665.

Franx, Marijn, Garth Illingworth, and Tim de Zeeuw (Dec. 1991). "The Ordered Nature of Elliptical Galaxies: Implications for Their Intrinsic Angular Momenta and Shapes". In: ApJ 383, p. 112. DOI: 10.1086/170769.

Freeman, K. C. (June 1970). "On the Disks of Spiral and S0 Galaxies". In: *The Astrophysical Journal* 160. ADS Bibcode: 1970ApJ...160..811F, p. 811. ISSN: 0004-637X. DOI: 10.1086/150474. URL: https://ui.adsabs.harvard.edu/abs/1970ApJ...160..811F (visited on 02/18/2024).

Fukugita, M., C. J. Hogan, and P. J. E. Peebles (Aug. 1998). "The Cosmic Baryon Budget". en. In: *The Astrophysical Journal* 503.2. Publisher: IOP Publishing, p. 518. ISSN: 0004-637X. DOI: 10.1086/306025. URL: https://iopscience.iop.org/article/10.1086/306025/meta (visited on 02/22/2024).

Gaia Collaboration et al. (Nov. 2016a). "The Gaia mission". In: A&A 595, A1, A1. DOI: 10.1051/0004-6361/201629272. arXiv: 1609.04153 [astro-ph.IM].

— (Nov. 2016b). "The Gaia mission". In: A&A 595, A1, A1. DOI: 10.1051/0004-6361/201629272. arXiv: 1609.04153 [astro-ph.IM].

Gaia Collaboration et al. (Aug. 2018a). "Gaia Data Release 2. Kinematics of globular clusters and dwarf galaxies around the Milky Way". In: A&A 616, A12, A12. DOI: 10.1051/0004-6361/201832698. arXiv: 1804.09381 [astro-ph.GA].

Gaia Collaboration et al. (2018b). "Gaia Data Release 2: Observational Hertzsprung-Russell diagrams". In: *Astronomy and Astrophysics* 616, A10. ISSN: 0004-6361. DOI: 10.1051/0004-6361/201832843. arXiv: 1804.09378. URL: http://arxiv.org/abs/1804.09378http://dx.doi.org/10.1051/0004-6361/201832843.

Gaia Collaboration et al. (Aug. 2018c). "Gaia Data Release 2. Observational Hertzsprung-Russell diagrams". In: A&A 616, A10, A10. DOI: 10.1051/0004-6361/201832843. arXiv: 1804.09378 [astro-ph.SR].

Gaia Collaboration et al. (Aug. 2018d). "Gaia Data Release 2. Summary of the contents and survey properties". In: A&A 616, A1, A1. DOI: 10.1051/0004-6361/201833051. arXiv: 1804.09365 [astro-ph.GA].

Gaia Collaboration et al. (May 2021). "Gaia Early Data Release 3. Summary of the contents and survey properties". In: A&A 649, A1, A1. DOI: 10.1051/0004-6361/202039657. arXiv: 2012.01533 [astro-ph.GA].

Gaia Collaboration et al. (June 2023a). "Gaia Data Release 3. Summary of the content and survey properties". In: A&A 674, A1, A1. DOI: 10.1051/0004-6361/202243940. arXiv: 2208.00211 [astro-ph.GA].

Gaia Collaboration et al. (Dec. 2023b). "Gaia Focused Product Release: Sources from Service Interface Function image analysis. Half a million new sources in omega Centauri". In: A&A 680, A35, A35. DOI: 10.1051/0004-6361/202347203. arXiv: 2310.06551 [astro-ph.SR].

Gallart, Carme et al. (Oct. 2015). "The ACS LCID Project: On the Origin of Dwarf Galaxy Types—A Manifestation of the Halo Assembly Bias?" In: ApJ 811.2, L18, p. L18. DOI: 10.1088/2041-8205/811/2/L18. arXiv: 1507.08350 [astro-ph.GA].

Garrison-Kimmel, Shea et al. (July 2019). "The Local Group on FIRE: dwarf galaxy populations across a suite of hydrodynamic simulations". In: *Monthly Notices of the Royal Astronomical Society* 487. ADS Bibcode: 2019MNRAS.487.1380G, pp. 1380–1399. ISSN: 0035-8711. DOI: 10.1093/mnras/stz1317. URL: https://ui.adsabs.harvard.edu/abs/2019MNRAS.487.1380G (visited on 03/03/2024).

Gelman, Andrew et al. (2013). *Bayesian data analysis*. CRC press.

Genina, Anna et al. (Feb. 2018). "The core-cusp problem: a matter of perspective". In: MNRAS 474.1, pp. 1398–1411. DOI: 10.1093/mnras/stx2855. arXiv: 1707.06303 [astro-ph.GA].

Gerola, H., P. Carnevali, and E. E. Salpeter (May 1983). "Dwarf elliptical galaxies." In: ApJ 268, pp. L75–L78. DOI: 10.1086/184032.

Gillessen, S. et al. (Feb. 2009). "Monitoring Stellar Orbits Around the Massive Black Hole in the Galactic Center". In: ApJ 692.2, pp. 1075–1109. DOI: 10.1088/0004-637X/692/2/1075. arXiv: 0810.4674 [astro-ph].

Gilman, Daniel et al. (Feb. 2020). "Warm dark matter chills out: constraints on the halo mass function and the free-streaming length of dark matter with eight quadruple-image strong gravitational lenses". In: MNRAS 491.4, pp. 6077–6101. DOI: 10.1093/mnras/stz3480. arXiv: 1908.06983 [astro-ph.CO].

Gilmore, Gerard et al. (July 2007). "The Observed Properties of Dark Matter on Small Spatial Scales". In: *The Astrophysical Journal* 663. ADS Bibcode: 2007ApJ...663..948G, pp. 948–959. ISSN: 0004-637X. DOI: 10.1086/518025. URL: https://ui.adsabs.harvard.edu/abs/2007ApJ...663..948G (visited on 03/09/2024).

Gilmore, Gerard et al. (July 2007). "The Observed Properties of Dark Matter on Small Spatial Scales". In: ApJ 663.2, pp. 948–959. DOI: 10.1086/518025. arXiv: astro-ph/0703308 [astro-ph].

Gnedin, Oleg Y., Jeremiah P. Ostriker, and Scott Tremaine (Apr. 2014). "Co-evolution of Galactic Nuclei and Globular Cluster Systems". In: ApJ 785.1, 71, p. 71. DOI: 10.1088/0004-637X/785/1/71. arXiv: 1308.0021 [astro-ph.CO].

Goerdt, Tobias et al. (May 2006). "Does the Fornax dwarf spheroidal have a central cusp or core?" In: MNRAS 368.3, pp. 1073–1077. DOI: 10.1111/j.1365-2966.2006.10182.x. arXiv: astro-ph/0601404 [astro-ph].

Goerdt, Tobias et al. (Dec. 2010). "Core Creation in Galaxies and Halos Via Sinking Massive Objects". In: ApJ 725.2, pp. 1707–1716. DOI: 10.1088/0004-637X/725/2/1707. arXiv: 0806.1951 [astro-ph].

Governato, F. et al. (Jan. 2010). "Bulgeless dwarf galaxies and dark matter cores from supernova-driven outflows". In: Nature 463.7278, pp. 203–206. DOI: 10.1038/nature08640. arXiv: 0911.2237 [astro-ph.CO].

Governato, F. et al. (May 2012). "Cuspy no more: how outflows affect the central dark matter and baryon distribution in Λ cold dark matter galaxies". In: MNRAS 422.2, pp. 1231–1240. DOI: 10.1111/j.1365-2966.2012.20696.x. arXiv: 1202.0554 [astro-ph.CO].

Graham, Alister W. and Rafael Guzmán (June 2003). "HST Photometry of Dwarf Elliptical Galaxies in Coma, and an Explanation for the Alleged Structural Dichotomy between Dwarf and Bright Elliptical Galaxies". In: *The Astronomical Journal* 125. ADS Bibcode: 2003AJ....125.2936G, pp. 2936–2950. ISSN: 0004-6256. DOI: 10.1086/374992. URL: https://ui.adsabs.harvard.edu/abs/2003AJ....125.2936G (visited on 03/03/2024).

Guo, Qi et al. (May 2011). "From dwarf spheroidals to cD galaxies: simulating the galaxy population in a ΛCDM cosmology". In: MNRAS 413.1, pp. 101–131. DOI: 10.1111/j.1365-2966.2010.18114.x. arXiv: 1006.0106 [astro-ph.CO].

Hargis, Jonathan R., Beth Willman, and Annika H. G. Peter (Nov. 2014). "Too Many, Too Few, or Just Right? The Predicted Number and Distribution of Milky Way Dwarf Galaxies". In: *The Astrophysical Journal* 795. ADS Bibcode: 2014ApJ...795L..13H, p. L13. ISSN: 0004-637X. DOI: 10.1088/2041-8205/795/1/L13. URL: https://ui.adsabs.harvard.edu/abs/2014ApJ...795L..13H (visited on 03/03/2024).

Hargreaves, J. C. et al. (Aug. 1994). "A dynamical study of the Sextans dwarf spheroidal galaxy." In: MNRAS 269, pp. 957–974. DOI: 10.1093/mnras/269.4.957.

Harris, William E. (Oct. 1996). "A Catalog of Parameters for Globular Clusters in the Milky Way". In: AJ 112, p. 1487. DOI: 10.1086/118116.

Hartmann, Markus et al. (Dec. 2011). "Constraining the role of star cluster mergers in nuclear cluster formation: simulations confront integral-field data". In: MNRAS 418.4, pp. 2697–2714. DOI: 10.1111/j.1365-2966.2011.19659.x. arXiv: 1103.5464 [astro-ph.CO].

Herlan, Robin, Alessandra Mastrobuono-Battisti, and Nadine Neumayer (Aug. 2023). "Nuclear star clusters as probes of dark matter haloes: the case of the Sagittarius

dwarf spheroidal galaxy". In: MNRAS 523.2, pp. 2721–2731. DOI: 10.1093/mnras/stad1584. arXiv: 2305.15517 [astro-ph.GA].

Hernandez, X. and Gerard Gilmore (June 1998). "Dynamical friction in dwarf galaxies". In: MNRAS 297.2, pp. 517–525. DOI: 10.1046/j.1365-8711.1998.01511.x. arXiv: astro-ph/9802261 [astro-ph].

Higson, Edward et al. (Sept. 2019). "Dynamic nested sampling: an improved algorithm for parameter estimation and evidence calculation". In: *Statistics and Computing* 29.5, pp. 891–913. DOI: 10.1007/s11222-018-9844-0. arXiv: 1704.03459 [stat.CO].

Hinshaw, G. et al. (Oct. 2013). "Nine-year Wilkinson Microwave Anisotropy Probe (WMAP) Observations: Cosmological Parameter Results". In: *The Astrophysical Journal Supplement Series* 208. ADS Bibcode: 2013ApJS..208...19H, p. 19. ISSN: 0067-0049. DOI: 10.1088/0067-0049/208/2/19. URL: https://ui.adsabs.harvard.edu/abs/2013ApJS..208...19H (visited on 02/22/2024).

Homma, Daisuke et al. (Nov. 2016). "A New Milky Way Satellite Discovered in the Subaru/Hyper Suprime-Cam Survey". In: ApJ 832.1, 21, p. 21. DOI: 10.3847/0004-637X/832/1/21. arXiv: 1609.04346 [astro-ph.GA].

Hu, Wayne, Rennan Barkana, and Andrei Gruzinov (Aug. 2000). "Fuzzy Cold Dark Matter: The Wave Properties of Ultralight Particles". In: Phys. Rev. Lett. 85.6, pp. 1158–1161. DOI: 10.1103/PhysRevLett.85.1158. arXiv: astro-ph/0003365 [astro-ph].

Huang, Kuan-Wei and Sergey E. Koposov (Jan. 2021). "Search for globular clusters associated with the Milky Way dwarf galaxies using Gaia DR2". In: MNRAS 500.1, pp. 986–997. DOI: 10.1093/mnras/staa3297. arXiv: 2005.14014 [astro-ph.GA].

Hui, Lam et al. (Feb. 2017). "Ultralight scalars as cosmological dark matter". In: Phys. Rev. D 95.4, 043541, p. 043541. DOI: 10.1103/PhysRevD.95.043541. arXiv: 1610.08297 [astro-ph.CO].

Ibata, R. et al. (July 2009). "Density and Kinematic Cusps in M54 at the Heart of the Sagittarius Dwarf Galaxy: Evidence for A 10^4 M_{sun} Black Hole?" In: ApJ 699.2, pp. L169–L173. DOI: 10.1088/0004-637X/699/2/L169. arXiv: 0906.4894 [astro-ph.GA].

Ibata, R. A., G. Gilmore, and M. J. Irwin (July 1994). "A dwarf satellite galaxy in Sagittarius". In: Nature 370.6486, pp. 194–196. DOI: 10.1038/370194a0.

Ibata, Rodrigo et al. (Feb. 2001). "Galactic Halo Substructure in the Sloan Digital Sky Survey: The Ancient Tidal Stream from the Sagittarius Dwarf Galaxy". In: ApJ 547.2, pp. L133–L136. DOI: 10.1086/318894. arXiv: astro-ph/0004255 [astro-ph].

Ibata, Rodrigo A. et al. (Feb. 1997). "The Kinematics, Orbit, and Survival of the Sagittarius Dwarf Spheroidal Galaxy". In: AJ 113, pp. 634–655. DOI: 10.1086/118283. arXiv: astro-ph/9612025 [astro-ph].

Ibata, Rodrigo A. et al. (Jan. 2013). "A vast, thin plane of corotating dwarf galaxies orbiting the Andromeda galaxy". In: Nature 493.7430, pp. 62–65. DOI: 10.1038/nature11717. arXiv: 1301.0446 [astro-ph.CO].

Iben Icko, Jr. and Robert T. Rood (Aug. 1970). "Metal-Poor Stars. III. on the Evolution of Horizontal-Branch Stars". In: ApJ 161, p. 587. DOI: 10.1086/150563.

Inoue, Shigeki (Aug. 2009). "The test for suppressed dynamical friction in a constant density core of dwarf galaxies". In: MNRAS 397.2, pp. 709–716. DOI: 10.1111/j.1365-2966.2009.15066.x. arXiv: 0901.4861 [astro-ph.CO].

Iršič, Vid et al. (July 2017). "New constraints on the free-streaming of warm dark matter from intermediate and small scale Lyman-α forest data". In: Phys. Rev. D 96.2, 023522, p. 023522. DOI: 10.1103/PhysRevD.96.023522. arXiv: 1702.01764 [astro-ph.CO].

Irwin, M. J. et al. (Feb. 2007). "Discovery of an Unusual Dwarf Galaxy in the Outskirts of the Milky Way". In: ApJ 656.1, pp. L13–L16. DOI: 10.1086/512183. arXiv: astro-ph/0701154 [astro-ph].

Jerjen, H., B. Binggeli, and K. C. Freeman (Feb. 2000). "Surface BR Photometry of Newly Discovered Dwarf Elliptical Galaxies in the Nearby Sculptor and Centaurus A Groups". In: AJ 119.2, pp. 593–608. DOI: 10.1086/301216.

Jungman, G., M. Kamionkowski, and K. Griest (Mar. 1996). "Supersymmetric dark matter". In: Phys. Rep. 267, pp. 195–373. DOI: 10.1016/0370-1573(95)00058-5. arXiv: hep-ph/9506380 [hep-ph].

Kaplinghat, Manoj, Mauro Valli, and Hai-Bo Yu (Nov. 2019). "Too big to fail in light of Gaia". In: MNRAS 490.1, pp. 231–242. DOI: 10.1093/mnras/stz2511. arXiv: 1904.04939 [astro-ph.GA].

Kaplinghat, Manoj et al. (July 2014). "Tying Dark Matter to Baryons with Self-Interactions". In: Phys. Rev. Lett. 113.2, 021302, p. 021302. DOI: 10.1103/PhysRevLett.113.021302. arXiv: 1311.6524 [astro-ph.CO].

Karachentseva, VE, ID Karachentsev, and F Börngen (1985). "Atlas of dwarf galaxies in the region of M 81 group". In: *Astronomy and Astrophysics Supplement Series* 60, pp. 213–227.

Kim, Hak-Sub et al. (Jan. 2019). "A Possible Relic Star Cluster in the Sextans Dwarf Galaxy". In: ApJ 870.1, L8, p. L8. DOI: 10.3847/2041-8213/aaf885. arXiv: 1901.02458 [astro-ph.GA].

Kimm, Taysun and Sukyoung K. Yi (2007). "Intrinsic Axis Ratio Distribution of Early-type Galaxies From Sloan Digital Sky Survey". In: *The Astrophysical Journal* 670.2, pp. 1048–1055. DOI: 10.1086/522573. arXiv: 0708.2631. URL: http://arxiv.org/abs/0708.2631http://dx.doi.org/10.1086/522573.

King, Ivan (Oct. 1962). "The structure of star clusters. I. an empirical density law". In: AJ 67, p. 471. DOI: 10.1086/108756.

Klypin, Anatoly et al. (Sept. 1999). "Where Are the Missing Galactic Satellites?" In: *The Astrophysical Journal* 522. ADS Bibcode: 1999ApJ...522...82K, pp. 82–92. ISSN: 0004-637X. DOI: 10.1086/307643. URL: https://ui.adsabs.harvard.edu/abs/1999ApJ...522...82K (visited on 03/03/2024).

Klypin, Anatoly et al. (Sept. 1999). "Where Are the Missing Galactic Satellites?" In: ApJ 522.1, pp. 82–92. DOI: 10.1086/307643. arXiv: astro-ph/9901240 [astro-ph].

Klypin, Anatoly A., Sebastian Trujillo-Gomez, and Joel Primack (Oct. 2011). "Dark Matter Halos in the Standard Cosmological Model: Results from the Bolshoi Simulation". In: ApJ 740.2, 102, p. 102. DOI: 10.1088/0004-637X/740/2/102. arXiv: 1002.3660 [astro-ph.CO].

Knapp, G. R., F. J. Kerr, and P. F. Bowers (Apr. 1978). "Upper limits to the H I content of the dwarf spheroidal galaxies." In: AJ 83, pp. 360–362. DOI: 10.1086/112211.

Knebe, Alexander et al. (June 2010). "The impact of baryonic physics on the shape and radial alignment of substructures in cosmological dark matter haloes". In: MNRAS 405.2, pp. 1119–1128. DOI: 10.1111/j.1365-2966.2010.16514.x. arXiv: 1002.2853 [astro-ph.CO].

Koposov, Sergey et al. (Oct. 2023). *joshspeagle/dynesty: v2.1.3*. Version v2.1.3. DOI: 10.5281/zenodo.8408702. URL: https://doi.org/10.5281/zenodo.8408702.

Koposov, Sergey E. et al. (June 2015). "Beasts of the Southern Wild: Discovery of Nine Ultra Faint Satellites in the Vicinity of the Magellanic Clouds." In: ApJ 805.2, 130, p. 130. DOI: 10.1088/0004-637X/805/2/130. arXiv: 1503.02079 [astro-ph.GA].

Koposov, Sergey E. et al. (2015). "Beasts of the southern wild: Discovery of nine ultra faint satellites in the vicinity of the magellanic Clouds". In: *Astrophysical Journal* 805.2, p. 130. ISSN: 15384357. DOI: 10.1088/0004-637X/805/2/130. arXiv: 1503.02079. URL: http://www.portal-nvo.noao.edu/.

Kormendy, J. (Aug. 1985). "Families of ellipsoidal stellar systems and the formation of dwarf elliptical galaxies." In: *The Astrophysical Journal* 295. ADS Bibcode: 1985ApJ...295...73K,

pp. 73–79. ISSN: 0004-637X. DOI: 10.1086/163350. URL: https://ui.adsabs.harvard.edu/abs/1985ApJ...295...73K (visited on 03/03/2024).

Kormendy, J. (Aug. 1985). "Families of ellipsoidal stellar systems and the formation of dwarf elliptical galaxies." In: ApJ 295, pp. 73–79. DOI: 10.1086/163350.

Kroupa, P., C. Theis, and C. M. Boily (Feb. 2005). "The great disk of Milky-Way satellites and cosmological sub-structures". In: A&A 431, pp. 517–521. DOI: 10.1051/0004-6361:20041122. arXiv: astro-ph/0410421 [astro-ph].

Kuhlen, Michael, Jürg Diemand, and Piero Madau (Dec. 2007). "The Shapes, Orientation, and Alignment of Galactic Dark Matter Subhalos". In: ApJ 671.2, pp. 1135–1146. DOI: 10.1086/522878. arXiv: 0705.2037 [astro-ph].

Kunkel, William E. and Serge Demers (Jan. 1976). "The Magellanic Plane". In: *The Galaxy and the Local Group*. Vol. 182, p. 241.

Lang, Dustin, David W. Hogg, and David Mykytyn (Apr. 2016). *The Tractor: Probabilistic astronomical source detection and measurement*. ascl: 1604.008.

Lasserre, T. et al. (Mar. 2000). "Not enough stellar mass Machos in the Galactic halo". In: A&A 355, pp. L39–L42. DOI: 10.48550/arXiv.astro-ph/0002253. arXiv: astro-ph/0002253 [astro-ph].

Li, T. S. et al. (2019). "The Southern Stellar Stream Spectroscopic Survey (${S}^5$): Overview, Target Selection, Data Reduction, Validation, and Early Science". In: *Monthly Notices of the Royal Astronomical Society* 490.3, pp. 3508–3531. DOI: 10.1093/mnras/stz2731. arXiv: 1907.09481. URL: http://arxiv.org/abs/1907.09481http://dx.doi.org/10.1093/mnras/stz2731.

Li, Zhao-Zhou et al. (Dec. 2017). "Determination of Dark Matter Halo Mass from Dynamics of Satellite Galaxies". In: ApJ 850.2, 116, p. 116. DOI: 10.3847/1538-4357/aa94c0. arXiv: 1710.08003 [astro-ph.GA].

Lin, D. N. C. and S. M. Faber (Mar. 1983). "Some implications of nonluminous matter in dwarf spheroidal galaxies." In: *The Astrophysical Journal* 266. ADS Bibcode: 1983ApJ...266L..21L, pp. L21–L25. ISSN: 0004-637X. DOI: 10.1086/183971. URL: https://ui.adsabs.harvard.edu/abs/1983ApJ...266L..21L (visited on 03/03/2024).

Lin, D. N. C. and S. M. Faber (Mar. 1983). "Some implications of nonluminous matter in dwarf spheroidal galaxies." In: ApJ 266, pp. L21–L25. DOI: 10.1086/183971.

Lindegren, L. et al. (Feb. 2012). "The astrometric core solution for the Gaia mission. Overview of models, algorithms, and software implementation". In: A&A 538, A78, A78. DOI: 10.1051/0004-6361/201117905. arXiv: 1112.4139 [astro-ph.IM].

Lindegren, L. et al. (May 2021). "Gaia Early Data Release 3. The astrometric solution". In: A&A 649, A2, A2. DOI: 10.1051/0004-6361/202039709. arXiv: 2012.03380 [astro-ph.IM].

Lotz, Jennifer M. et al. (May 2001). "Dynamical Friction in dE Globular Cluster Systems". en. In: *The Astrophysical Journal* 552.2. Publisher: IOP Publishing, p. 572. ISSN: 0004-637X. DOI: 10.1086/320545. URL: https://iopscience.iop.org/article/10.1086/320545/meta (visited on 04/23/2023).

Lynden-Bell, D. (Mar. 1976). "Dwarf galaxies and globular clusters in high velocity hydrogen streams." In: MNRAS 174, pp. 695–710. DOI: 10.1093/mnras/174.3.695.

Mackey, A. D. and G. F. Gilmore (Jan. 2003a). "Surface brightness profiles and structural parameters for 10 rich stellar clusters in the Small Magellanic Cloud". In: MNRAS 338.1, pp. 120–130. DOI: 10.1046/j.1365-8711.2003.06022.x. arXiv: astro-ph/0209046 [astro-ph].

— (Jan. 2003b). "Surface brightness profiles and structural parameters for 53 rich stellar clusters in the Large Magellanic Cloud". In: MNRAS 338.1, pp. 85–119. DOI: 10.1046/j.1365-8711.2003.06021.x. arXiv: astro-ph/0209031 [astro-ph].

Mackey, A. D. and G. F. Gilmore (Mar. 2003c). "Surface brightness profiles and structural parameters for globular clusters in the Fornax and Sagittarius dwarf spheroidal galaxies". In: MNRAS 340.1, pp. 175–190. DOI: 10.1046/j.1365-8711.2003.06275.x. arXiv: astro-ph/0211396 [astro-ph].

Majewski, S. R., APOGEE Team, and APOGEE-2 Team (Sept. 2016). "The Apache Point Observatory Galactic Evolution Experiment (APOGEE) and its successor, APOGEE-2". In: *Astronomische Nachrichten* 337.8-9, p. 863. DOI: 10.1002/asna.201612387.

Majewski, Steven R. et al. (Dec. 2003). "A Two Micron All Sky Survey View of the Sagittarius Dwarf Galaxy. I. Morphology of the Sagittarius Core and Tidal Arms". In: ApJ 599.2, pp. 1082–1115. DOI: 10.1086/379504. arXiv: astro-ph/0304198 [astro-ph].

Majewski, Steven R. et al. (Sept. 2017). "The Apache Point Observatory Galactic Evolution Experiment (APOGEE)". In: AJ 154.3, 94, p. 94. DOI: 10.3847/1538-3881/aa784d. arXiv: 1509.05420 [astro-ph.IM].

Mashchenko, Sergey, H. M. P. Couchman, and James Wadsley (Aug. 2006). "The removal of cusps from galaxy centres by stellar feedback in the early Universe". In: *Nature* 442. ADS Bibcode: 2006Natur.442..539M, pp. 539–542. ISSN: 0028-0836. DOI: 10.1038/nature04944. URL: https://ui.adsabs.harvard.edu/abs/2006Natur.442..539M (visited on 03/06/2024).

Mashchenko, Sergey, James Wadsley, and H. M. P. Couchman (Jan. 2008). "Stellar Feedback in Dwarf Galaxy Formation". In: *Science* 319. ADS Bibcode: 2008Sci...319..174M, p. 174. ISSN: 0036-8075. DOI: 10.1126/science.1148666. URL: https://ui.adsabs.harvard.edu/abs/2008Sci...319..174M (visited on 03/06/2024).

Mateo, Mario (Apr. 1996). "Dwarf Spheroidal Galaxies and the Formation of the Galactic Halo". In: *Formation of the Galactic Halo...Inside and Out*. Ed. by Heather L. Morrison and Ata Sarajedini. Vol. 92. Astronomical Society of the Pacific Conference Series, p. 434.

Mateo, Mario (1998). "Dwarf galaxies of the Local Group". In: *Annual Review of Astronomy and Astrophysics* 36.1, pp. 435–506. ISSN: 00664146. DOI: 10.1146/annurev.astro.36.1.435. arXiv: 9810070 [astro-ph]. URL: https://www.annualreviews.org/doi/abs/10.1146/annurev.astro.36.1.435.

Mateo, Mario et al. (Feb. 1996). "Discovery of a Tidal Extension of the Sagittarius Dwarf Spheroidal Galaxy". In: ApJ 458, p. L13. DOI: 10.1086/309919.

Mayer, L. et al. (Feb. 2007). "Early gas stripping as the origin of the darkest galaxies in the Universe". In: Nature 445.7129, pp. 738–740. DOI: 10.1038/nature05552. arXiv: astro-ph/0702495 [astro-ph].

Mayer, Lucio et al. (Oct. 2001a). "The Metamorphosis of Tidally Stirred Dwarf Galaxies". In: ApJ 559.2, pp. 754–784. DOI: 10.1086/322356. arXiv: astro-ph/0103430 [astro-ph].

— (Feb. 2001b). "Tidal Stirring and the Origin of Dwarf Spheroidals in the Local Group". In: ApJ 547.2, pp. L123–L127. DOI: 10.1086/318898. arXiv: astro-ph/0011041 [astro-ph].

Mayer, Lucio et al. (Oct. 2002). "Tidal debris of dwarf spheroidals as a probe of structure formation models". In: MNRAS 336.1, pp. 119–130. DOI: 10.1046/j.1365-8711.2002.05721.x. arXiv: astro-ph/0110386 [astro-ph].

McConnachie, Alan W. (2012). "The observed properties of dwarf galaxies in and around the Local Group". In: *Astronomical Journal* 144.1, pp. 4–36. ISSN: 00046256. DOI: 10.1088/0004-6256/144/1/4. arXiv: 1204.1562. URL: https://iopscience.iop.org/article/10.1088/0004-6256/144/1/4https://iopscience.iop.org/article/10.1088/0004-6256/144/1/4/meta.

McConnachie, Alan W. (July 2012). "The Observed Properties of Dwarf Galaxies in and around the Local Group". In: AJ 144.1, 4, p. 4. DOI: 10.1088/0004-6256/144/1/4. arXiv: 1204.1562 [astro-ph.CO].

McGaugh, Stacy S., Federico Lelli, and James M. Schombert (Nov. 2016). "Radial Acceleration Relation in Rotationally Supported Galaxies". In: Phys. Rev. Lett. 117.20, 201101, p. 201101. DOI: 10.1103/PhysRevLett.117.201101. arXiv: 1609.05917 [astro-ph.GA].

McGaugh, Stacy S., Vera C. Rubin, and W. J. G. de Blok (Nov. 2001). "High-Resolution Rotation Curves of Low Surface Brightness Galaxies. I. Data". In: *The Astronomical Journal* 122. ADS Bibcode: 2001AJ....122.2381M, pp. 2381–2395. ISSN: 0004-6256. DOI: 10.1086/323448. URL: https://ui.adsabs.harvard.edu/abs/2001AJ....122.2381M (visited on 03/03/2024).

Meadows, Noah et al. (Jan. 2020). "Cusp or core? Revisiting the globular cluster timing problem in Fornax". In: MNRAS 491.3, pp. 3336–3342. DOI: 10.1093/mnras/stz3280. arXiv: 1910.11887 [astro-ph.GA].

Merritt, D. and B. Tremblay (1996). "Evidence From Intrinsic Shapes for Two Families of Elliptical Galaxies". In: *The Astronomical Journal* 111, p. 2243. ISSN: 00046256. DOI: 10.1086/117959. URL: http://arxiv.org/abs/astro-ph/9601038http://dx.doi.org/10.1086/117959.

Merritt, David et al. (Dec. 2006). "Empirical Models for Dark Matter Halos. I. Nonparametric Construction of Density Profiles and Comparison with Parametric Models". In: AJ 132.6, pp. 2685–2700. DOI: 10.1086/508988. arXiv: astro-ph/0509417 [astro-ph].

Miles, Roger E (1965). "On random rotations in R^3". In: *Biometrika* 52.3/4, pp. 636–639.

Milgrom, M. (July 1983a). "A modification of the Newtonian dynamics - Implications for galaxies." In: ApJ 270, pp. 371–383. DOI: 10.1086/161131.

— (July 1983b). "A modification of the newtonian dynamics : implications for galaxy systems." In: ApJ 270, pp. 384–389. DOI: 10.1086/161132.

— (July 1983c). "A modification of the Newtonian dynamics as a possible alternative to the hidden mass hypothesis." In: ApJ 270, pp. 365–370. DOI: 10.1086/161130.

Minelli, Alice et al. (Jan. 2023). "The metallicity distribution in the core of the Sagittarius dwarf spheroidal: Minimising the metallicity biases". In: A&A 669, A54, A54. DOI: 10.1051/0004-6361/202244890. arXiv: 2211.06727 [astro-ph.GA].

Monaco, L. et al. (Feb. 2005). "The central density cusp of the Sagittarius dwarf spheroidal galaxy". In: *Monthly Notices of the Royal Astronomical Society* 356.4, pp. 1396–1402. ISSN: 0035-8711. DOI: 10.1111/j.1365-2966.2004.08579.x. URL: https://doi.org/10.1111/j.1365-2966.2004.08579.x (visited on 04/23/2023).

Moore, Ben (Aug. 1994). "Evidence against dissipation-less dark matter from observations of galaxy haloes". In: *Nature* 370. ADS Bibcode: 1994Natur.370..629M, pp. 629–631. ISSN: 0028-0836. DOI: 10.1038/370629a0. URL: https://ui.adsabs.harvard.edu/abs/1994Natur.370..629M (visited on 03/03/2024).

Moore, Ben (Aug. 1994). "Evidence against dissipation-less dark matter from observations of galaxy haloes". In: Nature 370.6491, pp. 629–631. DOI: 10.1038/370629a0.

Moore, Ben et al. (Oct. 1999). "Dark Matter Substructure within Galactic Halos". In: *The Astrophysical Journal* 524. ADS Bibcode: 1999ApJ...524L..19M, pp. L19–L22. ISSN: 0004-637X. DOI: 10.1086/312287. URL: https://ui.adsabs.harvard.edu/abs/1999ApJ...524L..19M (visited on 03/03/2024).

Moore, Ben et al. (Oct. 1999). "Dark Matter Substructure within Galactic Halos". In: ApJ 524.1, pp. L19–L22. DOI: 10.1086/312287. arXiv: astro-ph/9907411 [astro-ph].

Moskowitz, A. G. and M. G. Walker (Mar. 2020). "Stellar Density Profiles of Dwarf Spheroidal Galaxies". In: ApJ 892.1, 27, p. 27. DOI: 10.3847/1538-4357/ab7459. arXiv: 1910.10134 [astro-ph.GA].

Muñoz, Ricardo R. et al. (June 2018). "A MegaCam Survey of Outer Halo Satellites. III. Photometric and Structural Parameters". In: ApJ 860.1, 66, p. 66. DOI: 10.3847/1538-4357/aac16b. arXiv: 1806.06891 [astro-ph.GA].

Mucciarelli, A. et al. (Sept. 2017). "Chemical abundances in the nucleus of the Sagittarius dwarf spheroidal galaxy". In: A&A 605, A46, A46. DOI: 10.1051/0004-6361/201730707. arXiv: 1705.03251 [astro-ph.GA].

Muraveva, Tatiana et al. (Sept. 2020). "A fresh look at the RR Lyrae population in the Draco dwarf spheroidal galaxy with Gaia". In: MNRAS. DOI: 10.1093/mnras/staa2984. arXiv: 2009.12191 [astro-ph.GA].

Naray, Rachel Kuzio de, Stacy S. McGaugh, and W. J. G. de Blok (Apr. 2008). "Mass Models for Low Surface Brightness Galaxies with High-Resolution Optical Velocity Fields". en. In: *The Astrophysical Journal* 676.2. Publisher: IOP Publishing, p. 920. ISSN: 0004-637X. DOI: 10.1086/527543. URL: https://iopscience.iop.org/article/10.1086/527543/meta (visited on 03/03/2024).

Navarro, Julio F., Vincent R. Eke, and Carlos S. Frenk (Dec. 1996). "The cores of dwarf galaxy haloes". In: *Monthly Notices of the Royal Astronomical Society* 283. ADS Bibcode: 1996MNRAS.283L..72N, pp. L72–L78. ISSN: 0035-8711. DOI: 10.1093/mnras/283.3.L72. URL: https://ui.adsabs.harvard.edu/abs/1996MNRAS.283L..72N (visited on 03/05/2024).

Navarro, Julio F., Carlos S. Frenk, and Simon D. M. White (May 1996). "The Structure of Cold Dark Matter Halos". In: ApJ 462, p. 563. DOI: 10.1086/177173. arXiv: astro-ph/9508025 [astro-ph].

Navarro, Julio F., Carlos S. Frenk, and Simon D. M. White (Dec. 1997). "A Universal Density Profile from Hierarchical Clustering". In: *The Astrophysical Journal* 490. ADS Bibcode: 1997ApJ...490..493N, pp. 493–508. ISSN: 0004-637X. DOI: 10.1086/304888. URL: https://ui.adsabs.harvard.edu/abs/1997ApJ...490..493N (visited on 03/02/2024).

Navarro, Julio F., Carlos S. Frenk, and Simon D. M. White (Dec. 1997). "A Universal Density Profile from Hierarchical Clustering". In: ApJ 490.2, pp. 493–508. DOI: 10.1086/304888. arXiv: astro-ph/9611107 [astro-ph].

Neumayer, Nadine, Anil Seth, and Torsten Böker (July 2020). "Nuclear star clusters". In: A&A Rev. 28.1, 4, p. 4. DOI: 10.1007/s00159-020-00125-0. arXiv: 2001.03626 [astro-ph.GA].

Nguyen, Dieu D. et al. (Sept. 2014). "EXTENDED STRUCTURE AND FATE OF THE NUCLEUS IN HENIZE 2-10". en. In: *The Astrophysical Journal* 794.1. Publisher: The American Astronomical Society, p. 34. ISSN: 0004-637X. DOI: 10.1088/0004-637X/794/1/34. URL: https://dx.doi.org/10.1088/0004-637X/794/1/34 (visited on 04/23/2023).

Nilles, H. P. (Aug. 1984). "Supersymmetry, supergravity and particle physics". In: Phys. Rep. 110.1-2, pp. 1–162. DOI: 10.1016/0370-1573(84)90008-5.

Nojiri, S., S. D. Odintsov, and V. K. Oikonomou (June 2017). "Modified gravity theories on a nutshell: Inflation, bounce and late-time evolution". In: Phys. Rep. 692, pp. 1–104. DOI: 10.1016/j.physrep.2017.06.001. arXiv: 1705.11098 [gr-qc].

Okamoto, S. et al. (May 2017). "Population gradient in the Sextans dSph: comprehensive mapping of a dwarf galaxy by Suprime-Cam". In: MNRAS 467.1, pp. 208–217. DOI: 10.1093/mnras/stx086. arXiv: 1701.04422 [astro-ph.GA].

Oman, Kyle A. et al. (Oct. 2015). "The unexpected diversity of dwarf galaxy rotation curves". In: *Monthly Notices of the Royal Astronomical Society* 452. ADS Bibcode: 2015MNRAS.452.3650O, pp. 3650–3665. ISSN: 0035-8711. DOI: 10.1093/mnras/stv1504. URL: https://ui.adsabs.harvard.edu/abs/2015MNRAS.452.3650O (visited on 03/09/2024).

Oman, Kyle A. et al. (Aug. 2016). "Missing dark matter in dwarf galaxies?" In: *Monthly Notices of the Royal Astronomical Society* 460. ADS Bibcode: 2016MNRAS.460.3610O, pp. 3610–3623. ISSN: 0035-8711. DOI: 10.1093/mnras/stw1251. URL: https://ui.adsabs.harvard.edu/abs/2016MNRAS.460.3610O (visited on 03/09/2024).

Oort, J. H. (Aug. 1932). "The force exerted by the stellar system in the direction perpendicular to the galactic plane and some related problems". In: *Bulletin of the Astronomical Institutes of the Netherlands* 6. ADS Bibcode: 1932BAN.....6..249O, p. 249. ISSN: 0365-8910. URL: https://ui.adsabs.harvard.edu/abs/1932BAN.....6..249O (visited on 02/18/2024).

Orkney, Matthew D. A. et al. (July 2021). "EDGE: two routes to dark matter core formation in ultra-faint dwarfs". In: MNRAS 504.3, pp. 3509–3522. DOI: 10.1093/mnras/stab1066. arXiv: 2101.02688 [astro-ph.GA].

Ostriker, J. P., P. J. E. Peebles, and A. Yahil (Oct. 1974). "The Size and Mass of Galaxies, and the Mass of the Universe". In: *The Astrophysical Journal* 193. ADS Bibcode: 1974ApJ...193L...1O, p. L1. ISSN: 0004-637X. DOI: 10.1086/181617. URL: https://ui.adsabs.harvard.edu/abs/1974ApJ...193L...1O (visited on 02/19/2024).

Pace, Andrew B. et al. (Dec. 2021). "Spectroscopic Confirmation of the Sixth Globular Cluster in the Fornax Dwarf Spheroidal Galaxy". In: *The Astrophysical Journal* 923. ADS Bibcode: 2021ApJ...923...77P, p. 77. ISSN: 0004-637X. DOI: 10.3847/1538-4357/ac2cd2. URL: https://ui.adsabs.harvard.edu/abs/2021ApJ...923...77P (visited on 03/11/2024).

Padilla, Nelson D. and Michael A. Strauss (2008). "The shapes of galaxies in the Sloan Digital Sky Survey". In: *Monthly Notices of the Royal Astronomical Society* 388.3, pp. 1321–1334. ISSN: 00358711. DOI: 10.1111/j.1365-2966.2008.13480.x. URL: https://academic.oup.com/mnras/article-lookup/doi/10.1111/j.1365-2966.2008.13480.x.

Paumard, T. et al. (June 2006). "The Two Young Star Disks in the Central Parsec of the Galaxy: Properties, Dynamics, and Formation*". en. In: *The Astrophysical Journal* 643.2. Publisher: IOP Publishing, p. 1011. ISSN: 0004-637X. DOI: 10.1086/503273. URL: https://iopscience.iop.org/article/10.1086/503273/meta (visited on 04/23/2023).

Pawlowski, M. S., J. Pflamm-Altenburg, and P. Kroupa (June 2012). "The VPOS: a vast polar structure of satellite galaxies, globular clusters and streams around the Milky Way". In: MNRAS 423.2, pp. 1109–1126. DOI: 10.1111/j.1365-2966.2012.20937.x. arXiv: 1204.5176 [astro-ph.GA].

Pawlowski, Marcel S. and Pavel Kroupa (Nov. 2013). "The rotationally stabilized VPOS and predicted proper motions of the Milky Way satellite galaxies". In: MNRAS 435.3, pp. 2116–2131. DOI: 10.1093/mnras/stt1429. arXiv: 1309.1159 [astro-ph.CO].

Peñarrubia, Jorge, Matthew G. Walker, and Gerard Gilmore (Nov. 2009). "Tidal disruption of globular clusters in dwarf galaxies with triaxial dark matter haloes". In: MNRAS 399.3, pp. 1275–1292. DOI: 10.1111/j.1365-2966.2009.15027.x. arXiv: 0905.0924 [astro-ph.GA].

Peñarrubia, Jorge et al. (June 2009). "The Signature of Galactic Tides in Local Group Dwarf Spheroidals". In: ApJ 698.1, pp. 222–232. DOI: 10.1088/0004-637X/698/1/222. arXiv: 0811.1579 [astro-ph].

Peebles, P. J. E. (June 1984). "The Origin of Galaxies and Clusters of Galaxies". In: *Science* 224.4656, pp. 1385–1391. DOI: 10.1126/science.224.4656.1385.

Petts, J. A., J. I. Read, and A. Gualandris (Nov. 2016). "A semi-analytic dynamical friction model for cored galaxies". In: MNRAS 463.1, pp. 858–869. DOI: 10.1093/mnras/stw2011. arXiv: 1607.04284 [astro-ph.GA].

Pier, J. R. (Dec. 1983). "AB stars in the southern galactic halo. II. Spectroscopy and radial velocities." In: ApJS 53, pp. 791–813. DOI: 10.1086/190910.

Planck Collaboration et al. (Sept. 2016). "Planck 2015 results. XIII. Cosmological parameters". In: *Astronomy and Astrophysics* 594. ADS Bibcode: 2016A&A...594A..13P, A13. ISSN: 0004-6361. DOI: 10.1051/0004-6361/201525830. URL: https://ui.adsabs.harvard.edu/abs/2016A&A...594A..13P (visited on 02/22/2024).

Plummer, H. C. (Mar. 1911). "On the problem of distribution in globular star clusters". In: MNRAS 71, pp. 460–470. DOI: 10.1093/mnras/71.5.460.

Pontzen, Andrew and Fabio Governato (Apr. 2012). "How supernova feedback turns dark matter cusps into cores". In: *Monthly Notices of the Royal Astronomical Society* 421. ADS Bibcode: 2012MNRAS.421.3464P, pp. 3464–3471. ISSN: 0035-8711. DOI: 10.1111/j.1365-2966.2012.20571.x. URL: https://ui.adsabs.harvard.edu/abs/2012MNRAS.421.3464P (visited on 03/05/2024).

Pontzen, Andrew et al. (Aug. 2015). "Milking the spherical cow - on aspherical dynamics in spherical coordinates". In: MNRAS 451.2, pp. 1366–1379. DOI: 10.1093/mnras/stv1032. arXiv: 1502.07356 [astro-ph.GA].

Price-Whelan, Adrian et al. (Nov. 2022). *adrn/gala: v1.6.1*. Version v1.6.1. DOI: 10.5281/zenodo.7299506. URL: https://doi.org/10.5281/zenodo.7299506.

Qi, Yuewen et al. (Nov. 2021). "Stellar proper motions in the outskirts of classical dwarf spheroidal galaxies with Gaia EDR3". In: *arXiv e-prints*, arXiv:2111.08737, arXiv:2111.08737. arXiv: 2111.08737 [astro-ph.GA].

Read, J. I., O. Agertz, and M. L. M. Collins (July 2016). "Dark matter cores all the way down". In: MNRAS 459.3, pp. 2573–2590. DOI: 10.1093/mnras/stw713. arXiv: 1508.04143 [astro-ph.GA].

Read, J. I. and G. Gilmore (Jan. 2005). "Mass loss from dwarf spheroidal galaxies: the origins of shallow dark matter cores and exponential surface brightness profiles". In: *Monthly Notices of the Royal Astronomical Society* 356. ADS Bibcode: 2005MNRAS.356..107R, pp. 107–124. ISSN: 0035-8711. DOI: 10.1111/j.1365-2966.2004.08424.x. URL: https://ui.adsabs.harvard.edu/abs/2005MNRAS.356..107R (visited on 03/05/2024).

Read, J. I., M. G. Walker, and P. Steger (Nov. 2018). "The case for a cold dark matter cusp in Draco". In: MNRAS 481.1, pp. 860–877. DOI: 10.1093/mnras/sty2286. arXiv: 1805.06934 [astro-ph.GA].

— (Mar. 2019). "Dark matter heats up in dwarf galaxies". In: MNRAS 484.1, pp. 1401–1420. DOI: 10.1093/mnras/sty3404. arXiv: 1808.06634 [astro-ph.GA].

Read, J. I. et al. (Dec. 2006). "Dynamical friction in constant density cores: a failure of the Chandrasekhar formula". In: MNRAS 373.4, pp. 1451–1460. DOI: 10.1111/j.1365-2966.2006.11022.x. arXiv: astro-ph/0606636 [astro-ph].

Read, J. I. et al. (Nov. 2016). "Understanding the shape and diversity of dwarf galaxy rotation curves in ΛCDM". In: MNRAS 462.4, pp. 3628–3645. DOI: 10.1093/mnras/stw1876. arXiv: 1601.05821 [astro-ph.GA].

Reid, M. J. and A. Brunthaler (Dec. 2004). "The Proper Motion of Sagittarius A*. II. The Mass of Sagittarius A*". In: ApJ 616.2, pp. 872–884. DOI: 10.1086/424960. arXiv: astro-ph/0408107 [astro-ph].

Riello, M. et al. (May 2021). "Gaia Early Data Release 3. Photometric content and validation". In: A&A 649, A3, A3. DOI: 10.1051/0004-6361/202039587. arXiv: 2012.01916 [astro-ph.IM].

Roberts, M. S. and R. N. Whitehurst (Oct. 1975). "The rotation curve and geometry of M31 at large galactocentric distances." In: *The Astrophysical Journal* 201. ADS Bibcode: 1975ApJ...201..327R, pp. 327–346. ISSN: 0004-637X. DOI: 10.1086/153889. URL: https://ui.adsabs.harvard.edu/abs/1975ApJ...201..327R (visited on 02/18/2024).

Roderick, T. A. et al. (July 2016). "Structural analysis of the Sextans dwarf spheroidal galaxy". In: MNRAS 460.1, pp. 30–43. DOI: 10.1093/mnras/stw949. arXiv: 1604.06214 [astro-ph.GA].

Rogstad, D. H. and G. S. Shostak (Sept. 1972). "Gross Properties of Five Scd Galaxies as Determined from 21-CENTIMETER Observations". In: ApJ 176, p. 315. DOI: 10.1086/151636.

Rose, J. A. (Oct. 1985). "Constraints on stellar populations in elliptical galaxies." In: AJ 90, pp. 1927–1956. DOI: 10.1086/113898.

Rossa, Jörn et al. (Sept. 2006). "Hubble Space Telescope STIS Spectra of Nuclear Star Clusters in Spiral Galaxies: Dependence of Age and Mass on Hubble Type". In: AJ 132.3, pp. 1074–1099. DOI: 10.1086/505968. arXiv: astro-ph/0604140 [astro-ph].

Rubin, V. C., W. K. Ford Jr., and N. Thonnard (June 1980). "Rotational properties of 21 SC galaxies with a large range of luminosities and radii, from NGC 4605 (R=4kpc) to UGC 2885 (R=122kpc)." In: *The Astrophysical Journal* 238. ADS Bibcode: 1980ApJ...238..471R, pp. 471–487. ISSN: 0004-637X. DOI: 10.1086/158003. URL: https://ui.adsabs.harvard.edu/abs/1980ApJ...238..471R (visited on 02/18/2024).

Rubin, Vera C. and Jr. Ford W. Kent (Feb. 1970). "Rotation of the Andromeda Nebula from a Spectroscopic Survey of Emission Regions". In: ApJ 159, p. 379. DOI: 10.1086/150317.

Rybizki, Jan et al. (Feb. 2022). "A classifier for spurious astrometric solutions in Gaia eDR3". In: MNRAS 510.2, pp. 2597–2616. DOI: 10.1093/mnras/stab3588. arXiv: 2101.11641 [astro-ph.IM].

Sales, Laura V., Andrew Wetzel, and Azadeh Fattahi (Aug. 2022). "Baryonic solutions and challenges for cosmological models of dwarf galaxies". en. In: *Nature Astronomy* 6.8. Number: 8 Publisher: Nature Publishing Group, pp. 897–910. ISSN: 2397-3366. DOI: 10.1038/s41550-022-01689-w. URL: https://www.nature.com/articles/s41550-022-01689-w (visited on 03/03/2024).

Salomon, J. B. et al. (June 2015). "The intrinsic ellipticity of dwarf spheroidal galaxies: constraints from the Andromeda system". In: MNRAS 450.2, pp. 1409–1419. DOI: 10.1093/mnras/stv741. arXiv: 1504.02091 [astro-ph.GA].

Sameie, Omid et al. (Sept. 2018). "The impact of baryonic discs on the shapes and profiles of self-interacting dark matter haloes". In: MNRAS 479.1, pp. 359–367. DOI: 10.1093/mnras/sty1516. arXiv: 1801.09682 [astro-ph.GA].

Sánchez-Janssen, Rubén et al. (June 2019). "The Next Generation Virgo Cluster Survey. XXIII. Fundamentals of Nuclear Star Clusters over Seven Decades in Galaxy Mass". In: ApJ 878.1, 18, p. 18. DOI: 10.3847/1538-4357/aaf4fd. arXiv: 1812.01019 [astro-ph.GA].

Sandage, Allan, Kenneth C. Freeman, and N. R. Stokes (1970). "The Intrinsic Flattening of e, so, and Spiral Galaxies as Related to Galaxy Formation and Evolution". In: *The Astrophysical Journal* 160, p. 831. ISSN: 0004-637X. DOI: 10.1086/150475. URL: https://ui.adsabs.harvard.edu/abs/1970ApJ...160..831S/abstract.

Sanders, Jason L. and N. Wyn Evans (Dec. 2017). "The shapes and alignments of the satellites of the Milky Way and Andromeda". In: MNRAS 472.3, pp. 2670–2685. DOI: 10.1093/mnras/stx2116. arXiv: 1708.06526 [astro-ph.GA].

Santos-Santos, Isabel M. E. et al. (June 2020). "Baryonic clues to the puzzling diversity of dwarf galaxy rotation curves". In: MNRAS 495.1, pp. 58–77. DOI: 10.1093/mnras/staa1072. arXiv: 1911.09116 [astro-ph.GA].

Sarajedini, Alta and Andrew C. Layden (Mar. 1995). "A Photometric Study of the Globular Cluster M54 and the Sagittarius Dwarf Galaxy: Evidence for Three Distinct Populations". In: AJ 109, p. 1086. DOI: 10.1086/117343.

Sawala, Till et al. (Apr. 2016). "The APOSTLE simulations: solutions to the Local Group's cosmic puzzles". In: *Monthly Notices of the Royal Astronomical Society* 457.2, pp. 1931–1943. ISSN: 0035-8711. DOI: 10.1093/mnras/stw145. URL: https://doi.org/10.1093/mnras/stw145 (visited on 03/03/2024).

Schlafly, Edward F. and Douglas P. Finkbeiner (Aug. 2011). "Measuring Reddening with Sloan Digital Sky Survey Stellar Spectra and Recalibrating SFD". In: ApJ 737.2, 103, p. 103. DOI: 10.1088/0004-637X/737/2/103. arXiv: 1012.4804 [astro-ph.GA].

Schlafly, Edward F. et al. (Dec. 2010). "The Blue Tip of the Stellar Locus: Measuring Reddening with the Sloan Digital Sky Survey". In: ApJ 725.1, pp. 1175–1191. DOI: 10.1088/0004-637X/725/1/1175. arXiv: 1009.4933 [astro-ph.GA].

Schlegel, David J., Douglas P. Finkbeiner, and Marc Davis (June 1998). "Maps of Dust Infrared Emission for Use in Estimation of Reddening and Cosmic Microwave Background Radiation Foregrounds". In: ApJ 500.2, pp. 525–553. DOI: 10.1086/305772. arXiv: astro-ph/9710327 [astro-ph].

Schneider, Michael D., Carlos S. Frenk, and Shaun Cole (May 2012). "The shapes and alignments of dark matter halos". In: J. Cosmology Astropart. Phys. 2012.5, 030, p. 030. DOI: 10.1088/1475-7516/2012/05/030. arXiv: 1111.5616 [astro-ph.CO].

Schönrich, Ralph, James Binney, and Walter Dehnen (Apr. 2010). "Local kinematics and the local standard of rest". In: *Monthly Notices of the Royal Astronomical Society* 403.4, pp. 1829–1833. ISSN: 0035-8711. DOI: 10.1111/j.1365-2966.2010.16253.x. eprint: https://academic.oup.com/mnras/article-pdf/403/4/1829/18575828/mnras0403-1829.pdf. URL: https://doi.org/10.1111/j.1365-2966.2010.16253.x.

Seth, Anil C. et al. (Nov. 2006). "Clues to Nuclear Star Cluster Formation from Edge-on Spirals". en. In: *The Astronomical Journal* 132.6. Publisher: IOP Publishing, p. 2539. ISSN: 1538-3881. DOI: 10.1086/508994. URL: https://iopscience.iop.org/article/10.1086/508994/meta (visited on 04/23/2023).

Siegel, Michael H. et al. (Sept. 2007). "The ACS Survey of Galactic Globular Clusters: M54 and Young Populations in the Sagittarius Dwarf Spheroidal Galaxy". In: ApJ 667.1, pp. L57–L60. DOI: 10.1086/522003. arXiv: 0708.0027 [astro-ph].

Siegel, Michael H. et al. (Dec. 2011). "The ACS Survey of Galactic Globular Clusters. XI. The Three-dimensional Orientation of the Sagittarius Dwarf Spheroidal Galaxy and Its Globular Clusters". In: ApJ 743.1, 20, p. 20. DOI: 10.1088/0004-637X/743/1/20. arXiv: 1108.6276 [astro-ph.GA].

Simon, Joshua D. (Aug. 2019). "The Faintest Dwarf Galaxies". In: ARA&A 57, pp. 375–415. DOI: 10.1146/annurev-astro-091918-104453. arXiv: 1901.05465 [astro-ph.GA].

Simon, Joshua D. et al. (Mar. 2005). "High-Resolution Measurements of the Halos of Four Dark Matter-Dominated Galaxies: Deviations from a Universal Density Profile*". en. In: *The Astrophysical Journal* 621.2. Publisher: IOP Publishing, p. 757. ISSN: 0004-637X. DOI: 10.1086/427684. URL: https://iopscience.iop.org/article/10.1086/427684/meta (visited on 03/03/2024).

Sirko, Edwin et al. (Feb. 2004). "Blue Horizontal-Branch Stars in the Sloan Digital Sky Survey. I. Sample Selection and Structure in the Galactic Halo". In: AJ 127.2, pp. 899–913. DOI: 10.1086/381483. arXiv: astro-ph/0311324 [astro-ph].

Skilling, John (Nov. 2004). "Nested Sampling". In: *Bayesian Inference and Maximum Entropy Methods in Science and Engineering: 24th International Workshop on Bayesian Inference and Maximum Entropy Methods in Science and Engineering*. Ed. by Rainer Fischer, Roland Preuss, and Udo Von Toussaint. Vol. 735. American Institute of Physics Conference Series, pp. 395–405. DOI: 10.1063/1.1835238.

Smith, Sinclair (Jan. 1936). "The Mass of the Virgo Cluster". In: *The Astrophysical Journal* 83. ADS Bibcode: 1936ApJ....83...23S, p. 23. ISSN: 0004-637X. DOI: 10.1086/143697. URL: https://ui.adsabs.harvard.edu/abs/1936ApJ....83...23S (visited on 02/18/2024).

Sommer-Larsen, Jesper, Per Rex Christensen, and Dave Carter (May 1989). "Blue horizontal branch field stars in the galactic halo -II." In: MNRAS 238, pp. 225–233. DOI: 10.1093/mnras/238.1.225.

Speagle, Joshua S. (Apr. 2020). "DYNESTY: a dynamic nested sampling package for estimating Bayesian posteriors and evidences". In: MNRAS 493.3, pp. 3132–3158. DOI: 10.1093/mnras/staa278. arXiv: 1904.02180 [astro-ph.IM].

Spergel, David N. and Paul J. Steinhardt (Apr. 2000). "Observational Evidence for Self-Interacting Cold Dark Matter". In: Phys. Rev. Lett. 84.17, pp. 3760–3763. DOI: 10.1103/PhysRevLett.84.3760. arXiv: astro-ph/9909386 [astro-ph].

Springel, Volker et al. (June 2005). "Simulations of the formation, evolution and clustering of galaxies and quasars". In: Nature 435.7042, pp. 629–636. DOI: 10.1038/nature03597. arXiv: astro-ph/0504097 [astro-ph].

Steigman, Gary and Michael S. Turner (Jan. 1985). "Cosmological constraints on the properties of weakly interacting massive particles". In: *Nuclear Physics B* 253, pp. 375–386. DOI: 10.1016/0550-3213(85)90537-1.

Stoehr, Felix et al. (Oct. 2002). "The satellite population of the Milky Way in a ΛCDM universe". In: MNRAS 335.4, pp. L84–L88. DOI: 10.1046/j.1365-8711.2002.05891.x. arXiv: astro-ph/0203342 [astro-ph].

Stoehr, Felix et al. (Nov. 2003). "Dark matter annihilation in the halo of the Milky Way". In: MNRAS 345.4, pp. 1313–1322. DOI: 10.1046/j.1365-2966.2003.07052.x. arXiv: astro-ph/0307026 [astro-ph].

Strigari, Louis E., Carlos S. Frenk, and Simon D. M. White (Nov. 2010). "Kinematics of Milky Way satellites in a Lambda cold dark matter universe". In: *Monthly Notices of the Royal Astronomical Society* 408.4, pp. 2364–2372. ISSN: 0035-8711. DOI: 10.1111/j.1365-2966.2010.17287.x. URL: https://doi.org/10.1111/j.1365-2966.2010.17287.x (visited on 03/09/2024).

Strigari, Louis E., Carlos S. Frenk, and Simon D. M. White (Nov. 2010). "Kinematics of Milky Way satellites in a Lambda cold dark matter universe". In: MNRAS 408.4, pp. 2364–2372. DOI: 10.1111/j.1365-2966.2010.17287.x. arXiv: 1003.4268 [astro-ph.CO].

Strom, S. E. et al. (Oct. 1970). "On the Evolutionary Status of Stars above the Horizontal Branch in Globular Clusters". In: A&A 8, p. 243.

Swart, J. G. de, G. Bertone, and J. van Dongen (Mar. 2017). "How dark matter came to matter". en. In: *Nature Astronomy* 1.3. Number: 3 Publisher: Nature Publishing Group, pp. 1–9. ISSN: 2397-3366. DOI: 10.1038/s41550-017-0059. URL: https://www.nature.com/articles/s41550-017-0059 (visited on 02/18/2024).

Taga, Masatoshi and Masanori Iye (Aug. 1998). "Orbital motion of a massive object in a dense stellar system". In: MNRAS 299.1, pp. 111–117. DOI: 10.1046/j.1365-8711.1998.01753.x.

The Dark Energy Survey Collaboration (Oct. 2005). "The Dark Energy Survey". In: *arXiv e-prints*, astro-ph/0510346, astro–ph/0510346. DOI: 10.48550/arXiv.astro-ph/0510346. arXiv: astro-ph/0510346 [astro-ph].

Thob, Adrien C. R. et al. (May 2019). "The relationship between the morphology and kinematics of galaxies and its dependence on dark matter halo structure in EAGLE". In: MNRAS 485.1, pp. 972–987. DOI: 10.1093/mnras/stz448. arXiv: 1811.01954 [astro-ph.GA].

Tisserand, P. et al. (July 2007). "Limits on the Macho content of the Galactic Halo from the EROS-2 Survey of the Magellanic Clouds". In: *Astronomy and Astrophysics* 469. ADS Bibcode: 2007A&A...469..387T, pp. 387–404. ISSN: 0004-6361. DOI: 10.1051/0004-6361:20066017. URL: https://ui.adsabs.harvard.edu/abs/2007A&A...469..387T (visited on 02/22/2024).

Tollerud, Erik J., Michael Boylan-Kolchin, and James S. Bullock (June 2014). "M31 satellite masses compared to ΛCDM subhaloes". In: MNRAS 440.4, pp. 3511–3519. DOI: 10.1093/mnras/stu474. arXiv: 1403.6469 [astro-ph.GA].

Tolstoy, Eline, Vanessa Hill, and Monica Tosi (2009). "Star-Formation Histories, Abundances, and kinematics of dwarf galaxies in the local group". In: *Annual Review of Astronomy and Astrophysics* 47, pp. 371–425. ISSN: 00664146. DOI: 10.1146/annurev-

astro-082708-101650. arXiv: 0904.4505. URL: https://www.annualreviews.org/doi/abs/10.1146/annurev-astro-082708-101650.

Tomozeiu, Mihai, Lucio Mayer, and Thomas Quinn (Feb. 2016). "The Evolution of Dwarf Galaxy Satellites with Different Dark Matter Density Profiles in the ErisMod Simulations. I. The Early Infalls". In: ApJ 818.2, 193, p. 193. DOI: 10.3847/0004-637X/818/2/193. arXiv: 1506.02140 [astro-ph.GA].

Torrealba, G. et al. (Nov. 2016). "At the survey limits: discovery of the Aquarius 2 dwarf galaxy in the VST ATLAS and the SDSS data". In: MNRAS 463.1, pp. 712–722. DOI: 10.1093/mnras/stw2051. arXiv: 1605.05338 [astro-ph.GA].

Tremaine, S. D. (Jan. 1976). "The formation of the nuclei of galaxies. II. The local group." In: ApJ 203, pp. 345–351. DOI: 10.1086/154085.

Tremaine, S. D., J. P. Ostriker, and Jr. Spitzer L. (Mar. 1975). "The formation of the nuclei of galaxies. I. M31." In: ApJ 196, pp. 407–411. DOI: 10.1086/153422.

Troxel, M. A. and Mustapha Ishak (Feb. 2015). "The intrinsic alignment of galaxies and its impact on weak gravitational lensing in an era of precision cosmology". In: Phys. Rep. 558, pp. 1–59. DOI: 10.1016/j.physrep.2014.11.001. arXiv: 1407.6990 [astro-ph.CO].

Tulin, Sean and Hai-Bo Yu (Feb. 2018). "Dark matter self-interactions and small scale structure". In: Phys. Rep. 730, pp. 1–57. DOI: 10.1016/j.physrep.2017.11.004. arXiv: 1705.02358 [hep-ph].

Turner, Monica L. et al. (Oct. 2012). "THE ACS FORNAX CLUSTER SURVEY. VI. THE NUCLEI OF EARLY-TYPE GALAXIES IN THE FORNAX CLUSTER*". en. In: *The Astrophysical Journal Supplement Series* 203.1. Publisher: The American Astronomical Society, p. 5. ISSN: 0067-0049. DOI: 10.1088/0067-0049/203/1/5. URL: https://dx.doi.org/10.1088/0067-0049/203/1/5 (visited on 05/06/2023).

Vasiliev, Eugene and Holger Baumgardt (Aug. 2021). "Gaia EDR3 view on galactic globular clusters". In: MNRAS 505.4, pp. 5978–6002. DOI: 10.1093/mnras/stab1475. arXiv: 2102.09568 [astro-ph.GA].

Vasiliev, Eugene and Vasily Belokurov (Oct. 2020). "The last breath of the Sagittarius dSph". In: MNRAS 497.4, pp. 4162–4182. DOI: 10.1093/mnras/staa2114. arXiv: 2006.02929 [astro-ph.GA].

Vasiliev, Eugene, Vasily Belokurov, and Denis Erkal (Feb. 2021). "Tango for three: Sagittarius, LMC, and the Milky Way". In: MNRAS 501.2, pp. 2279–2304. DOI: 10.1093/mnras/staa3673. arXiv: 2009.10726 [astro-ph.GA].

Velliscig, Marco et al. (Oct. 2015). "The alignment and shape of dark matter, stellar, and hot gas distributions in the EAGLE and cosmo-OWLS simulations". In: MNRAS 453.1, pp. 721–738. DOI: 10.1093/mnras/stv1690. arXiv: 1504.04025 [astro-ph.GA].

Vera-Ciro, Carlos and Amina Helmi (Aug. 2013). "Constraints on the Shape of the Milky Way Dark Matter Halo from the Sagittarius Stream". In: ApJ 773.1, L4, p. L4. DOI: 10.1088/2041-8205/773/1/L4. arXiv: 1304.4646 [astro-ph.GA].

Vera-Ciro, Carlos A. et al. (Apr. 2014). "The shape of dark matter subhaloes in the Aquarius simulations". In: MNRAS 439.3, pp. 2863–2872. DOI: 10.1093/mnras/stu153. arXiv: 1402.0903 [astro-ph.CO].

Vitali, Sara et al. (Oct. 2022). "The Pristine Inner Galaxy Survey (PIGS) IV: A photometric metallicity analysis of the Sagittarius dwarf spheroidal galaxy". In: MNRAS. DOI: 10.1093/mnras/stac2869. arXiv: 2204.12140 [astro-ph.GA].

Vivas, A. Katherina et al. (Jan. 2019). "The Population of Pulsating Variable Stars in the Sextans Dwarf Spheroidal Galaxy". In: AJ 157.1, 35, p. 35. DOI: 10.3847/1538-3881/aaf4f3. arXiv: 1811.12207 [astro-ph.SR].

Vogelsberger, Mark et al. (Jan. 2020). "Cosmological simulations of galaxy formation". In: *Nature Reviews Physics* 2.1, pp. 42–66. DOI: 10.1038/s42254-019-0127-2. arXiv: 1909.07976 [astro-ph.GA].

Walcher, C. J. et al. (Oct. 2006). "Stellar Populations in the Nuclei of Late-Type Spiral Galaxies*". en. In: *The Astrophysical Journal* 649.2. Publisher: IOP Publishing, p. 692. ISSN: 0004-637X. DOI: 10.1086/505166. URL: https://iopscience.iop.org/article/10.1086/505166/meta (visited on 04/23/2023).

Walker, Matthew G., Mario Mateo, and Edward W. Olszewski (Dec. 2008). "Systemic Proper Motions of Milky Way Satellites from Stellar Redshifts: The Carina, Fornax, Sculptor, and Sextans Dwarf Spheroidals". In: ApJ 688.2, p. L75. DOI: 10.1086/595586. arXiv: 0810.1511 [astro-ph].

Walker, Matthew G. and Jorge Peñarrubia (Nov. 2011). "A Method for Measuring (Slopes of) the Mass Profiles of Dwarf Spheroidal Galaxies". In: ApJ 742.1, 20, p. 20. DOI: 10.1088/0004-637X/742/1/20. arXiv: 1108.2404 [astro-ph.CO].

Walker, Matthew G. et al. (Oct. 2009a). "A Universal Mass Profile for Dwarf Spheroidal Galaxies?" In: ApJ 704.2, pp. 1274–1287. DOI: 10.1088/0004-637X/704/2/1274. arXiv: 0906.0341 [astro-ph.CO].

Walker, Matthew G. et al. (Feb. 2009b). "Clean Kinematic Samples in Dwarf Spheroidals: An Algorithm for Evaluating Membership and Estimating Distribution Parameters When Contamination is Present". In: AJ 137.2, pp. 3109–3138. DOI: 10.1088/0004-6256/137/2/3109. arXiv: 0811.1990 [astro-ph].

Westfall, Kyle B. et al. (Jan. 2006). "Exploring Halo Substructure with Giant Stars. VIII. The Extended Structure of the Sculptor Dwarf Spheroidal Galaxy". In: AJ 131.1, pp. 375–406. DOI: 10.1086/496975. arXiv: astro-ph/0508091 [astro-ph].

Wetzel, Andrew R. et al. (Aug. 2016). "Reconciling Dwarf Galaxies with ΛCDM Cosmology: Simulating a Realistic Population of Satellites around a Milky Way-mass Galaxy". In: ApJ 827.2, L23, p. L23. DOI: 10.3847/2041-8205/827/2/L23. arXiv: 1602.05957 [astro-ph.GA].

White, S. D. M., C. S. Frenk, and M. Davis (Nov. 1983). "Clustering in a neutrino-dominated universe". In: *The Astrophysical Journal* 274. ADS Bibcode: 1983ApJ...274L...1W, pp. L1–L5. ISSN: 0004-637X. DOI: 10.1086/184139. URL: https://ui.adsabs.harvard.edu/abs/1983ApJ...274L...1W (visited on 02/22/2024).

White, Simon D. M. and Carlos S. Frenk (Sept. 1991). "Galaxy Formation through Hierarchical Clustering". In: ApJ 379, p. 52. DOI: 10.1086/170483.

Willman, B. and J. Strader (Aug. 2012). ""GALAXY," DEFINED". en. In: *The Astronomical Journal* 144.3. Publisher: The American Astronomical Society, p. 76. ISSN: 1538-3881. DOI: 10.1088/0004-6256/144/3/76. URL: https://dx.doi.org/10.1088/0004-6256/144/3/76 (visited on 03/03/2024).

Wilson, J. C. et al. (May 2019). "The Apache Point Observatory Galactic Evolution Experiment (APOGEE) Spectrographs". In: PASP 131.999, p. 055001. DOI: 10.1088/1538-3873/ab0075. arXiv: 1902.00928 [astro-ph.IM].

Wolf, Joe et al. (Aug. 2010). "Accurate masses for dispersion-supported galaxies". In: MNRAS 406.2, pp. 1220–1237. DOI: 10.1111/j.1365-2966.2010.16753.x. arXiv: 0908.2995 [astro-ph.CO].

Wright, A. H. et al. (Sept. 2017). "Galaxy And Mass Assembly (GAMA): the galaxy stellar mass function to z = 0.1 from the r-band selected equatorial regions". In: MNRAS 470.1, pp. 283–302. DOI: 10.1093/mnras/stx1149. arXiv: 1705.04074 [astro-ph.GA].

Wyse, R. F. G. (Jan. 2001). "The Merging History of the Milky Way Disk". In: *Galaxy Disks and Disk Galaxies*. Ed. by José G. Funes and Enrico Maria Corsini. Vol. 230. Astronomical Society of the Pacific Conference Series, pp. 71–80. DOI: 10.48550/arXiv.astro-ph/0012270. arXiv: astro-ph/0012270 [astro-ph].

Xu, Weishuang Linda and Lisa Randall (Sept. 2020). "Testing ΛCDM with Dwarf Galaxy Morphology". In: ApJ 900.1, 69, p. 69. DOI: 10.3847/1538-4357/aba51f. arXiv: 1904.08949 [astro-ph.GA].

Zavala, Jesús et al. (Aug. 2016). "The link between the assembly of the inner dark matter halo and the angular momentum evolution of galaxies in the EAGLE simulation". In: MNRAS 460.4, pp. 4466–4482. DOI: 10.1093/mnras/stw1286. arXiv: 1512.02636 [astro-ph.GA].

Zwicky, F. (Jan. 1933). "Die Rotverschiebung von extragalaktischen Nebeln". In: *Helvetica Physica Acta* 6. ADS Bibcode: 1933AcHPh...6..110Z, pp. 110–127. ISSN: 0018-0238. URL: https://ui.adsabs.harvard.edu/abs/1933AcHPh...6..110Z (visited on 02/18/2024).